LUND UNIVERSITY

On the Growth of Bone through Stress Driven Diffusion and Bone Generation Processes

Lindberg, Gustav

2018

Document Version:
Publisher's PDF, also known as Version of record

Link to publication

Citation for published version (APA):
Lindberg, G. (2018). *On the Growth of Bone through Stress Driven Diffusion and Bone Generation Processes*. [Doctoral Thesis (compilation), Faculty of Engineering, LTH]. Solid Mechanics, Faculty of Engineering, Lund University.

Total number of authors:
1

General rights
Unless other specific re-use rights are stated the following general rights apply:
Copyright and moral rights for the publications made accessible in the public portal are retained by the authors and/or other copyright owners and it is a condition of accessing publications that users recognise and abide by the legal requirements associated with these rights.
• Users may download and print one copy of any publication from the public portal for the purpose of private study or research.
• You may not further distribute the material or use it for any profit-making activity or commercial gain
• You may freely distribute the URL identifying the publication in the public portal

Read more about Creative commons licenses: https://creativecommons.org/licenses/

Take down policy
If you believe that this document breaches copyright please contact us providing details, and we will remove access to the work immediately and investigate your claim.

LUND UNIVERSITY

PO Box 117
221 00 Lund
+46 46-222 00 00

Department of Construction Sciences
Solid Mechanics

ISRN LUTFD2/TFHF-18/1059-SE(1–138)
ISBN (PRINTED VERSION) 978-91-7753-881-3
ISBN (ELECTRONIC VERSION) 978-91-7753-882-0

On the Growth of Bone through Stress Driven Diffusion and Bone Generation Processes

Doctoral Dissertation by

GUSTAV LINDBERG

Copyright © 2018 by Gustav Lindberg
Division of Solid Mechanics, Lund University, Box 118, SE-221 00 Lund, Sweden
Homepage: http://www.solid.lth.se
Printed by Media-Tryck AB, Lund, Sweden

Till Elin, Gabriel och Alba

Preface

This thesis is the result of my PhD studies conducted at the Division of Solid Mechanics at Lund University.

My sincere thanks go to my supervisor Prof. Per Ståhle who has guided me through this work and shown me an incredible patience. His expertise in solid mechanics and mathematics has made this work possible. Likewise I am very grateful to my assistant supervisor Ass. Prof. Ingrid Svensson whose knowledge in biomechanics has introduced me to an otherwise unknown field of research. I would also like to thank Prof. Mathias Wallin, Prof. Matti Ristinmaa and Prof. Niels Saabye Ottosen who, through pedagogic and inspiring teaching, introduced me to the field of solid mechanics and finite element modelling.

Finally, thank you my beloved Elin for pushing me forward and giving me the support and energy needed to spend nights and weekends finishing this work. This could not have been done without you.

Stockholm, October 2018

Gustav Lindberg

Abstract

In order to prevent or modify bone degeneration due to rest or due to diseases such as osteopenia and osteoporosis, the modeling and remodeling of bone tissue must be better understood. In this thesis it is assumed that the primary condition leading to bone growth is a change of the chemical environment caused by transport of matter resulting from stress driven diffusion. The change in the chemical environment may consist of changes in the concentration of different substances stimulating, for example, bone building osteoblast recruitment or suppression of bone resorbing osteoclast activity. Inspired by a study found in the literature where an experiment is performed on avian bones, two numerical models are developed which can be solved using a regular structural finite element solver. The first model acknowledges that diffusion of matter is affected by the gradient of external potential energies such as heat, electrical or mechanical, of which the mechanical is assumed to be important. The derivation of the statistical mechanics of the molecular diffusing matter leads, according to Einstein (1905), to a partial differential equation similar to Fick's law but with an added diffusio-mechanical coupling term. The diffusio-mechanical term is a function of the hydrostatic pressure due to bending of the bone. Since bone growth takes place at the outer bone surface, the hypothesis is that substances promoting bone growth are transported from the medullary cavity to the outer surface, the periosteum, of the long skeletal bone. From comparison with experiments, it is found that bone growth to a higher extent takes place where high concentration of matter arises rather than where the mechanical stress is high. It is also seen that bone growth depends on load frequency. The second model also starts from the basic assumptions made in the first model regarding the preservation of energy. To derive the governing coupled diffusio-mechanical partial differential equations, the matter required for the generation of bone is assumed to be transported easily through the bone or surrounding fluids. Therefore, to simplify the analysis, the governing equations may be put on a non-conservative form. The Ginzburg-Landau theory is used to formulate the expression for the phase transformation like process for the generation of bone. The available energies are elastic strain energy due to bending, the concentration gradient energy and a chemical potential. The model uses a phase field variable to describe the state of the bone, and the model shows that high loading initiate bone growth whereas low loading makes the bone contract. The models use normalized input data, but in order to make full use of the results the actual diffusion coefficient of interest must be known, and hence an approach to determine diffusion coefficient in bone tissue is developed. By means of conductivity measurements together with an analytical solution, which is fitted to the experimental data using a Kalman filter, diffusion coefficients can be extracted. With known diffusion coefficients it is possible to evaluate the normalized results from the numerical models. Finally a model to evaluate the physiological status of the bone by looking only at a small portion of the cross-section of a bone is presented. The approach uses the size and shape of the pores of a representative area of the bone cross-section to determine a value of an effective diffusion coefficient of matter and an effective Young's modulus of the bone. A database with parameters used in the method must be established once with finite element analysis. The model can then be used by anyone, and no knowledge of finite element analysis is required. The calculated values can be used to evaluate how much the porosity is affecting the bone status.

Populärvetenskaplig sammanfattning

För att bättre kunna förebygga att skelettet bryts ner vid långvarig vila eller vid sjukdomar som osteopenia och osteoporos, behövs bättre förståelse för de processer som styr detta. I den här avhandlingen antas att den primära orsaken till bentillväxt är en förändring i den kemiska miljön i benet. Förändringen antas orsakas av att tillväxtstimulerande ämnen transporteras genom benet till den plats där bentillväxt sedan sker. Transporten sker genom spänningsdriven diffusion (spänning som i tryck och drag). De tillväxtstimulerande ämnena tros påverka de celler som är involverade i uppbyggnad respektive nedbrytning av ben, så som till exempel osteoblaster eller osteoklaster. Två numeriska modeller utvecklas vilka är inspirerade av ett experiment, funnet i litteraturen, där bentillväxt på grund av mekanisk last på vingben från fåglar undersöktes. Båda modellerna kan lösas med en vanlig kommersiell finita element-lösare. Den första modellen utgår ifrån det faktum att diffusion påverkas av extern potentiell energi så som från värme, elektricitet eller mekanisk last. I denna avhandling antas den mekaniska lasten vara viktig. Utifrån den statistiska mekaniken för diffusion fås, enligt Einstein (1905), en differentialekvation som är snarlik Ficks första lag men med en kopplad diffusionsmekanisk term. Denna är en funktion av den hydrostatiska spänningen som uppstår vid böjning av benet. Eftersom bentillväxt sker vid utsidan på benet är hypotesen att de växtstimulerande ämnena transporteras från det inre hålrummet i benet ut till utsidan av benet (periosteum). Efter jämförelse med experiment ses att bentillväxt i större utsträckning sker där koncentrationen av växtstimulerande ämnen är hög, än där spänningen är hög. Det ses också att bentillväxten påverkas av lastfrekvensen. Den andra modellen tar avstamp i de grundläggande antagandena angående bevarande av energi i den första modellen. För att bestämma den styrande differentialekvationen antas att de ämnen som krävs för bentillväxt kan transporteras genom benet eller från omkringliggande vätskor. För att förenkla analysen blir den styrande ekvationen icke-konservativ. Ginzburgs och Landaus teori används för att ta fram ett uttryck för den fasförändring i modellen som ger bentillväxt. De tillgängliga energierna är elastisk energi på grund av böjning, koncentrationsgradients-energin samt en kemisk potential. Modellen använder sig av en fasfältsvariabel för att beskriva benet. Modellen visar att hög belastning ger bentillväxt, medan låg last gör att benets tvärsnittsarea minskar. De numeriska modellerna använder sig av normaliserade indata, men för att fullt ut kunna nyttja modellerna behövs specifika värden på indata, bland annat värdet på diffusionskoefficienten. Därför utvecklas en metod för att genom experiment kunna bestämma en diffusionskoefficients värde. Genom ett konduktivitetsexperiment och en analytisk lösning, vilken anpassas till det experimentella datat med hjälp av ett Kalman-filter, kan en diffusionskoefficient bestämmas. Som det fjärde arbetet i den här avhandlingen presenteras en metod för att kunna bestämma vilket hälsostatus ett ben har genom att bara studera en liten del av ett tvärsnitt av benet. Metoden använder sig av den storlek och form som porerna har i den studerade delen, som bedöms vara representativ för hela tvärsnittet. En effektiv diffusionskoefficient räknas fram tillsammans med en effektiv elasticitetsmodul för benet. Värdena på dessa kan användas för att bedöma hur mycket benet är påverkat av porositeten. En databas med parametrar som behövs i metoden bestäms på förhand med finita element metoden, sedan kan metoden användas av vem som helst, inga krav på kunskaper i finita element eller andra numeriska metoder behövs.

List of appended papers

This PhD thesis is based on the following papers:

Paper A
G. Lindberg, L. Banks-Sills, P. Ståhle and I. Svensson (2013)
A Two-Dimensional Model for Stress Driven Diffusion in Bone Tissue.
Computer Methods in Biomechanics and Biomedical Engineering, 2015 18(5):457-67
DOI: http://dx.doi.org/10.1080/10255842.2013.807507

Paper B
G. Lindberg and P. Ståhle (2018)
Growth of a Long Bone Cross Section - A 2D Phase-Field Model.
Submitted May 15, 2018
Revised manuscript submitted Oct 17, 2018

Paper C
G. Lindberg, A. Shokry, W. Reheman and I. Svensson (2014)
Determination of diffusion coefficients in bovine bone by means of conductivity measurement.
Int. Journal of Experimental and Computational Biomechanics, 2014 2(4):324-342
DOI: https://doi.org/10.1504/IJECB.2014.066086

Paper D A. Shokry, G. Lindberg, G. Kharmanda and P. Ståhle (2017)
A Superposition Procedure for Calculation of Effective Diffusion and Elastic Parameters of Sparsely Porous Materials.
Transport in Porous Media, 2017 118(3):472-94
DOI: https://doi.org/10.1007/S11242-017-0866-4

Own contributions The author of this thesis has taken the main responsibility for the preparation and writing of Papers A to C. In Paper D the preparation and writing was done in collaboration with the co-authors. In Paper C, the author has taken the main responsibility for preparation and writing of the main part of the paper except for section 4.1, Kalman filtering, which has been prepared by Abdallah Shokry. The development of the theories has in all papers been conducted in collaboration with the co-authors. The numerical implementation of the models has been done entirely by the author in Paper A and in Paper B, and in collaboration with the co-authors in Paper C and Paper D.

Contents

1 Background

1.1 Introduction

Each year millions of people around the world get affected by various bone diseases, making the skeletal bones in the body less dense, leading to fractures, immobility and pain. Osteology is a large research field and a lot of research is carried out to better understand the processes of bone degeneration and what can be done in order to prevent it. Already in 1892, Julius Wolff (Wolff, 1892) published his findings about bone adaptation. The most important of his observations was that bone will adapt to the load that it is being subjected to. This is known as Wolff's law and is an example on how mechanobiology is used to understand bone development.

Growth and remodelling of bone tissue (osteogenesis) is dominated by the activity of bone cells such as osteoblasts, osteoclast, osteocytes and bone lining cells (Cowin, 2001; Currey, 2002; Bilezikian, Raisz and Martin, 2008). The cause of activation of these cells is widely discussed, and several hypotheses exist involving both direct and indirect activation due to mechanical load. See for instance Banks-Sills et al. (2011) for indirect dependence on strain levels or Isaksson et al. (2007) for bone growth dependent on shear strains and fluid flow.

The mechanisms of how solutes transport in bone, and how the removing of the waste products that are stored in skeletal tissue is accomplished, have been studied by many authors, e.g. in the papers by Piekarski and Munro (1977), Maroudas et al. (1992), Knothe Tate et al. (1998), and Fernandez-Seara et al. (2002). It was understood that one of the important mechanisms is diffusion, which plays an essential role in accomplishing these transports and also in the removal of waste products. Piekarski and Munro (1977), Kufahl and Saha (1990) and Knothe Tate and Niederer (1998) showed that stress-induced fluid flow may be important in bone remodelling, and that lack of such flow may be one cause for developing osteoporosis during immobilisation.

Frost (2004) proposed that bone growth is controlled by a tissue-level negative feedback system. E.g. low activity, such as bed rest or being under low-gravity conditions, results in bone resorption, but with increased activity bone growth is stimulated. The observation was that long bones are strengthened by adding bone at the outer (periosteal) surface. This will increase the second moment of area and the resistance to bending or torsional loading. Moreover, it has been observed that static loading does not cause bone remodeling (Lanyon and Rubin, 1984). The observations by Frost (2004) and Lanyon and Rubin (1984) are seemingly in conflict if it is assumed that load itself controls the remodeling process.

This thesis treats the causes of the shape adoption of the mid-shaft of long bones (e.g. femur, tibia and ulna) due to mechanical loading using two numerical models. An analytical expression is also developed to determine the diffusion coefficient and the Young's modulus over a large cross-section of a bone by looking at only a small part of it, making the progress of determining the healthiness of the bone faster. An experimental method for finding values for the diffusion coefficients of matter in bone tissue is also developed. The findings from these experiments are used in the numerical models.

1.2 About bone tissue

Bone tissue consists of an organic matrix called the osteoid, which is embedded in a crystalline complex of hydroxyapatite (calcium and phosphate). In adult developed bone tissue, the osteoid makes up about (by weight) 30% of the tissue (of which 2-5% bone cells), the hydroxyapatite 60% and the remaining 10% is water (Marcus et al., 2008). The osteoid itself is to 95% made up of type I collagen, and the remaining of noncollagenous proteins and cells. The collagen gives the bone tissue its resistance to tension, while the hydroxyapatite gives the bone its resistance to compression (Bilezikian, Raisz and Martin, 2008). As new bone is formed (ossification), the organic matrix is first created and is then mineralised with the hydroxyapatite. On a larger scale it is possible to identify two types of bone structure; cortical and cancellous. Cortical bone, also called compact bone, is dens with a porosity below 15%, while cancellous bone has a higher porosity, above 50%, and consists of a lattice of plates and rods called the trabecula (Currey, 2002). Cancellous bone is less stiff and with viscous properties and is also referred to as spongy bone. In general, cortical bone constitutes the shafts of long skeletal bones covered by the very outer surface of the bone, the periosteum. Cancellous bone is found close to joints, e.g. in the ends of long bones. It is also found close to cavities, e.g. the medullary cavity in long bones and to a high extent in the vertebrae. In adult humans the skeleton mass consists of approximately 80% cortical bone, while the remaining 20% is trabecular (Marcus et al., 2008). The distribution varies though from bone to bone. For the ulna about 90% of the bone is of cortical type, while for a vertebrae the distribution is rather 60% cortical and 40% cancellous (Cowin, 2001). The distribution over each bone also varies. For the mid-shaft of the long bone, called the diaphysis, there is almost no cancellous bone but, again, at the ends of the long bones, the epiphysis, there is mainly cancellous bone covered by only a thin layer of cortical bone. In both cancellous and cortical bone the material appears in two different shapes: woven and lamellar. Growing and developing bone material (immature bone) is of the type woven but is gradually replaced by lamellar bone (mature bone). In woven bone the collagen fiber directions are less organized, in comparison to lamellar bone, where the collagen fibers run in the same direction, at least locally (Currey, 2002).

This thesis focuses on the mid-shaft, diaphysis, of long skeletal bones and hence the focus is cortical bone. In Papers A and B the used geometry is the cross-section from avian ulna. In Paper C the bone samples used in the diffusion experiment are taken from the mid-shaft of a bovine femur. The studied bone in Paper D is from bovine as well.

In cortical bone the lamella forms cylindrical units which can be seen as a circular pattern over a bone cross-section. These units are called osteons and are oriented with their longitudinal axis mainly parallel to the longitudinal direction of the long bone (Hert, Fiala and Petrtýl, 1994). In Figure 1a the cross-section of cortical bone from a bovine femur can be seen, and in 1b a close-up on an osteon from the same sample is shown. The dimensions of the osteons are approximately 200 μm in diameter. In Figure 1a and b the circumferential lamellae of the osteon in cortical bone can be seen together with the remaining of old osteons (interstitial lamellae). In the middle of an osteon runs a canal called the Haversian canal which contains nerves and blood vessels. The Haversian canal in one osteon is in contact with the Haversian canal in the neighboring osteon via a transverse canal called Volkmann's canal. A principle sketch of a section of cortical bone

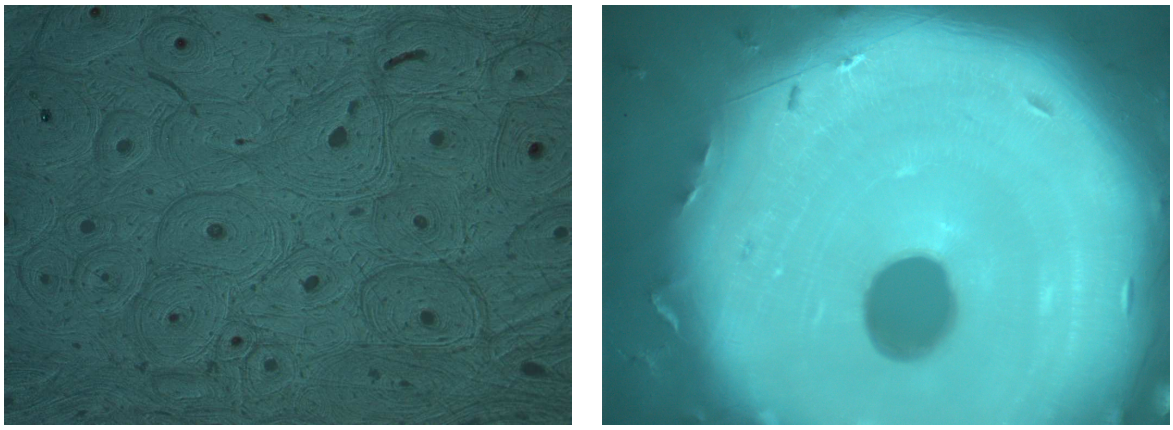

(a) Osteons and the interstitial lamellae

(b) Close up on a osteon

Figure 1: Cross section of the diaphysis of a femur from bovine. Pictures taken by the author.

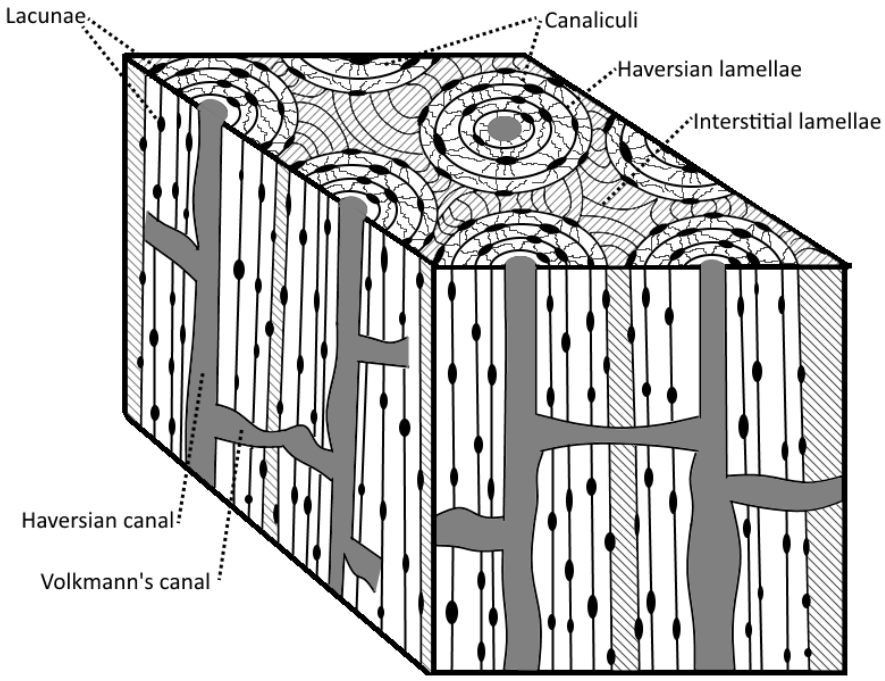

Figure 2: Sketch of cortical bone.

is shown in Figure 2.

From the Haversian canal a small network of canals branch out over the osteon cross-section. This network is called the canaliculi. During ossification, the bone building osteoblasts are trapped in small spaces within the bone matrix. These spaces are called lacunas, and can be seen in Figure 1b. The lacunas are connected to the Haversian canal via the canalicular network. The trapped osteoblasts here differentiate into another type of bone cell which are called osteocytes (Cowin, 2001).

1.3 About diffusion

Diffusion is a transport process where atoms migrate within a gas, liquid or inside a solid material. For instance if salt is poured into a tank of water, the salt molecules will by time be distributed all over the tank. Another example is when hydrogen penetrates and moves through steel thus creating hydrogen embrittlement. Diffusion occurs for all temperatures above absolute zero and becomes faster for higher temperatures since diffusion is dependent on the vibrations of atoms.

In 1827 Robert Brown observed the chaotic motion of small particles in a fluid, and the phenomena is called Brownian motion. Later both Einstein (1905) and Smoluchowski (1906) observed this phenomena and that led them to their respectively theoretical descriptions of diffusion.

This thesis utilizes the diffusion of nutrients and signal substances through compact bone in order to predict bone growth. The pathways through the bone are not treated, since the models are intended to be used for any molecule size. Smaller molecules may move through compact bone as through any solid, i.e. by means of interstitial diffusion or vacancy assisted diffusion. In interstitial diffusion the substitutional atom moves in between the sites of the host atoms, for instance the small hydrogen atom diffusing in steel. In vacancy assisted diffusion, the substitutional atom moves through the structure by jumping to a neighbouring free site, a vacancy. When the diffusing atoms become too large for interstitial diffusion, the vacancy assisted diffusion is the most common type of diffusion in pure solids. In compact bone, larger molecules may diffuse through the vessels of the vascular system, through the lacunae-canalicular system or through the matrix porosity of the cortical bone. It has been suggested that diffusion of nutrients through compact bone tissue is too slow to sufficiently supply the cells in compact bone with nutrients, and that other pathways are needed, for instance as in Piekarski and Munro (1977) and Knothe Tate and Niederer (1998) where the supply to osteocytes is studied.

Diffusion can be looked at either from a macroscopic or from a microscopic view. On the macroscopic scale diffusion is modelled by classical continuum field equations, for instance Fick's law which is described in the following chapters of this thesis. With the continuum field equations it appears as if the diffusing atoms are drawn to areas of lower concentration. As if they could sense variations of concentration. The process may be better understood if diffusion is studied on the microscopic scale. The diffusion is then treated as a stochastic process and the phenomena may be modelled with random walks. The atom can jump in any direction within the structure being just as likely to move towards high concentration as in any other direction.

The microscopic and macroscopic view may thus seem to be in conflict. However, if the boundary between of an area of high concentration and very low concentration is studied, it is seen that once the process has started, just as many atoms lying next to the boundary would have jumped into the area of low concentration as would have jumped in the other direction. Hence a net flow of mass would have occurred towards the area of low concentration.

Albert Einstein's research (Einstein, 1905) on the motion of atoms opened up a new field for understanding of diffusion on the microscopic scale. Einstein defined the diffusion coefficient D by the average time t it takes an atom to move a distance λ in d dimensions

as

$$D = \frac{1}{2d}\frac{\lambda^2}{t}\,, \tag{1}$$

i.e. making it possible to determine D by studying the microscopic scale.

In Fick's law, the transport process is governed by the concentration gradient and the corresponding diffusion coefficient D at a specific temperature. But, diffusion can be affected by several parameters though such as heat, mechanical loading, electrical fields and gravity. In some cases the diffusing atoms may interact with each other, i.e. attracting or repelling each other, which may lead to inclusions of concentration dependent diffusion coefficients. It is also possible to model changing chemical composition which will affect the flow of matter. This can be done by including a chemical potential in the governing equation. In this thesis both mechanical loading and a chemical potential is included to describe the diffusion process in cortical bone.

1.4 About constitutive properties of bone tissue

The mechanical properties for cortical bone have been investigated in numerous of studies during the past half century. Based on the findings by Reilly and Burstein (1975), Kutz (2003), Nyman et al. (2009) and Mirzaali et al. (2016) the average values of Young's modulus, the yield stress and the ultimate strength of cortical bone can be determined, which are summarized in Table 1. The values are for cortical bone in the human femur. As seen in Table 1 the axial and transverse directions have different properties. By

Table 1: Values of Young's modulus E, yield stress in tension σ_{YT}, yield stress in compression σ_{YC}, ultimate tensile strength σ_{UTS} and ultimate compressive strength σ_{UCS} for human cortical bone.

Direction	E	σ_{YT}	σ_{YC}	σ_{UTS}	σ_{UCS}
-	[GPa]	[MPa]	[MPa]	[MPa]	[MPa]
Axial	20	60	110	130	170
Transverse	10	40	90	50	130

"axial", the axial direction of a long bone is here implied, and by "transverse" the plane described by the radial and circumferential directions is intended. Bone can be modelled as orthotropic, or even transversely isotropic (Kutz, 2003), where the transverse plane has isotropic properties. In this thesis the coordinate system is aligned with these material orientations. The x_1- and x_2-axis are placed in the transverse (isotropic) plane, and the x_3-axis is placed along the axial direction of the long bones. Further, cortical bone may be modelled as linear elastic for small strains. The relation between stresses and strains is in this thesis modelled with Hooke's law $\sigma_{ij}{=}\mathcal{D}_{ijkl}\epsilon_{kl}$, where σ_{ij} is the second order stress tensor, $\mathcal{D}_{ijkl}$ the fourth order stiffness tensor and ϵ_{kl} the second order strain tensor and the indices i,j,k,l=1..3. The relation between flow of matter and the concentration gradient is modelled with Fick's first law

$$J_i(\boldsymbol{x}, t) = -D_{ij}\frac{\partial}{\partial x_j}c(\boldsymbol{x}, t)\,, \tag{2}$$

where $\boldsymbol{x}$=(x_1, x_2, x_3), i=1,2,3 and j=1,2,3 in the standard Cartesian coordinate system.

If the diffusivity properties of cortical bone is treated as transversely isotropic the diffusion tensor D_{ij} becomes

$$\boldsymbol{D} = \begin{bmatrix} D_{11} & 0 & 0 \\ 0 & D_{22} & 0 \\ 0 & 0 & D_{33} \end{bmatrix} \tag{3}$$

where D_{11}=D_{22}=D_t and D_{33}=D_a. In this thesis the diffusion in the transverse plane is studied, and the concentration of matter is modelled not to be depended on a flow in the axial x_3-direction. Hence the problem is limited to the x_1-x_2 plane and the diffusion tensor becomes

$$\boldsymbol{D} = \begin{bmatrix} D_t & 0 \\ 0 & D_t \end{bmatrix} = D \, , \tag{4}$$

and Fick's first law simplifies to

$$J_i(\boldsymbol{x}, t) = -D \frac{\partial}{\partial x_i} c(\boldsymbol{x}, t) \, , \tag{5}$$

where i=1,2 and j=1,2. It must be emphasised that published values for bone properties have a rather big span, depending on test methods but also depending on age of the donors. In the study by Malo et al. (2013) on the mid-shaft of human femur, it was seen that the porosity at this location went up from approximately 9% for the age of 17 to 17% at the age of 82. In a study by McCalden et al. (1993) on cortical bone from the human femur (from donors in the age of 20 to 102 years old) it was seen that the ultimate stress, the ultimate strain and energy absorption decreased by 5, 9, and 12% per decade, respectively.

2 Load cases for numerical models

The geometry used in the two numerical models (Paper A and Paper B) in this thesis is taken from the experiment by Lanyon and Rubin (1984), who studied the development of the cross-section in avian ulnas after *in vivo* applying oscillating compressions over the ulnas 100 times per day á 1 Hz for eight weeks. The load cases in the numerical models are inspired by the same experiment, and it is here believed that the compression forces also gave, due to the curvature of the long bone, a bending moment. In Lanyon and Rubin (1984) the neutral axis was determined in the cross-section at the middle of one of the ulnas using strain gauges. In the numerical models the cross-section from the experiment is placed in the x_1-x_2-plane. In the first numerical model the neutral axis from the experiment is chosen as the x_1-axis, see Figure 3a. The reason why the Lanyon and Rubin (1984) neutral axis does not coincide with one of the two geometrical principal axes of the cross-section is that the load case of compression and moment moves the neutral axis to the measured location. Applying a moment around the neutral axis produces bending only about this axis, and gives the same distribution of the out of plane stress σ_{33} over the cross-section as in the experiment. Any shear strains are neglected since the equipment used in the Lanyon and Rubin (1984) experiment is assumed in this thesis to have hindered torsion, and the bone is also treated as slender in comparison to

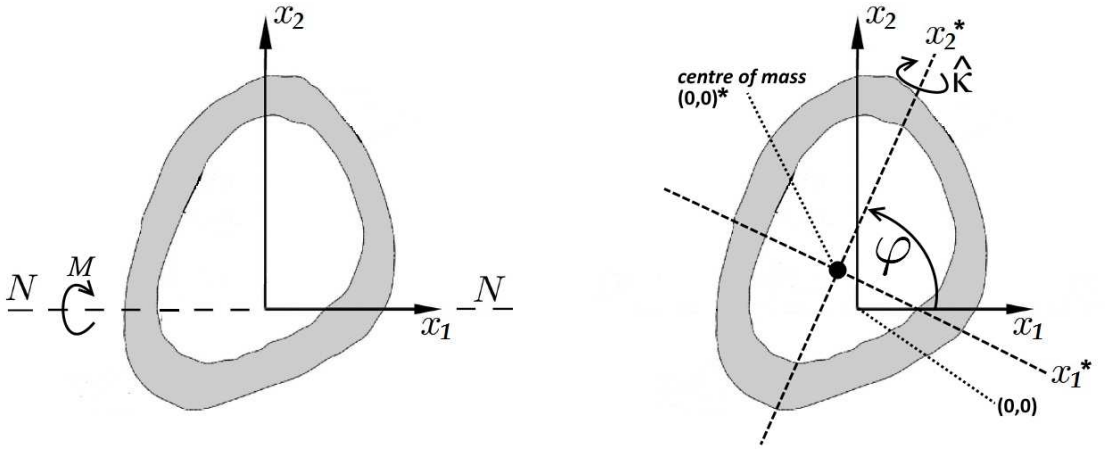

(a) Load case in the first numerical model - a bending moment M

(b) Main load case in the second numerical model - a bending $\hat{\kappa}$

Figure 3: The cross-section of the right intact turkey ulna from Lanyon and Rubin (1984).

its diameter. Treating the bone as slender allows the use of the Euler-Bernoulli theory for pure bending where transverse forces are neglected.

In the first numerical model the load case is an oscillating moment M applied around the x_1-axis treated as a neutral axis, as seen in Figure 3a. In the second numerical model the main load case is a static bending $\hat{\kappa}$ applied around the second geometrical principal axis, also called the minor centroidal axis, of the cross-section (Figure 3b) which then becomes a neutral axis. In the second numerical model a second load case is also evaluated where the static bending is applied around the x_1-axis just as in the first numerical model.

3 Distribution of growth promoting substances over the cross-section

With the background on the importance of exercise for bone growth, and with the knowledge of the importance of diffusion processes for bone growth and transport of substances, a 2-dimensional numerical model for stress driven transport of matter is developed. The geometry is a cross-section of the mid-diaphysis of a mammal's long bone. The approach is inspired by the 1-dimensional findings by Banks-Sills et al. (2011), and by the experimental findings of Lanyon and Rubin (1984). In addition to the gradient of a concentration field $c(\boldsymbol{x}, t)$, the gradient of the hydrostatic stress $\sigma_h(\boldsymbol{x}, t)$ caused by the bending is modelled to provide a driving force resulting in transport of matter in the plane of the cross-section. The latter controls the diffusion process. The geometry is shown in Figure 3a.

The flux $J_i(\boldsymbol{x}, t)$ of a selected substance in the bone environment becomes (Li, 1978)

$$J_i(\boldsymbol{x}, t) = -D\frac{\partial}{\partial x_i}c(\boldsymbol{x}, t) + BV_A c_o \frac{\partial}{\partial x_i}\sigma_h(\boldsymbol{x}, t)\,. \tag{6}$$

In eq. (6), D is the diffusion coefficient of the substance-bone system, B is the mechanical

mobility, V_A is the atomic volume of the bone nutrients and c_o is the ambient concentration.

Matter is modelled to be conserved and the divergence of the flux $J_i(\boldsymbol{x}, t)$ is by that related to the concentration by

$$\frac{\partial}{\partial x_i} J_i(\boldsymbol{x}, t) = -\frac{\partial}{\partial t} c(\boldsymbol{x}, t) \, . \tag{7}$$

The flux $J_i(\boldsymbol{x}, t)$ can be eliminated by combining eqs. (6) and (7), and the governing equation becomes

$$\frac{\partial}{\partial t} c(\boldsymbol{x}, t) = \frac{\partial}{\partial x_i}[D \frac{\partial}{\partial x_i} c(\boldsymbol{x}, t)] - V_A c_o \frac{\partial}{\partial x_i}[B \frac{\partial}{\partial x_i} \sigma_h(\boldsymbol{x}, t)] \, . \tag{8}$$

The material is modelled as linear elastic with a Young's modulus E. Since the load case is pure bending around the x_1-axis, the only stress component becomes the out-of-plane stress (x_3). The hydrostatic stress in eq. (8) is then obtained as

$$\sigma_h = \frac{1}{3}\sigma_{ii} = \frac{1}{3}\sigma_{33} = \frac{M(t) x_2}{3I} \, . \tag{9}$$

The moment $M(t)$ is oscillating in time with an angular velocity, ω, according to

$$M(t) = M_o \sin(\omega t) \, . \tag{10}$$

With this, along with the assumption that the diffusion coefficient D and the mechanical mobility B are constants, insertion of eqs. (9) and (10) into eq. (8) results in the governing differential equation for the concentration as

$$\frac{\partial}{\partial t} c(\boldsymbol{x}, t) = D \frac{\partial^2}{\partial x_i \partial x_i} c(\boldsymbol{x}, t) \, . \tag{11}$$

To simplify the analysis, dimensionless variables are introduced for the flux vector and the concentration as

$$\hat{\boldsymbol{J}} = \frac{3I}{B V_A c_o M_o} \boldsymbol{J} \qquad \hat{c} = \frac{3ID}{B V_A M_o a} \frac{c - c_o}{c_o} \tag{12}$$

where a is a measure of the width of the bone obtained as the average at four locations (two along the x_1-axis and two along the x_2-axis as in Figure 3)a. In addition, the time, space coordinates and the load frequency are normalized as

$$\hat{t} = \frac{D}{a^2} t \qquad \hat{x_i} = \frac{x_i}{a} \qquad \hat{\omega} = \frac{a^2}{D} \omega \, . \tag{13}$$

Equation (11) is now written as

$$\frac{\partial}{\partial t} \hat{c}(\hat{\boldsymbol{x}}, \hat{t}) = \frac{\partial^2}{\partial \hat{x}_i \partial \hat{x}_i} \hat{c}(\hat{\boldsymbol{x}}, \hat{t}) \, . \tag{14}$$

Since in the present study, the bone is assumed to be subject to cyclic loading for an extended period (i.e. $\hat{t} \gg 1$), the steady state solution is sought.

Due to the sinusoidal load, the solution will have a sinusoidal boundary condition, and so the solution to the partial differential equation in eq. (14) will approach a pure oscillatory state after a long time. It may be written in the form

$$\hat{c}(\hat{\boldsymbol{x}},\hat{t}) = {}^{a}\hat{c}(\hat{\boldsymbol{x}})\sin(\hat{\omega}\hat{t}) + {}^{b}\hat{c}(\hat{\boldsymbol{x}})\cos(\hat{\omega}\hat{t}) \tag{15}$$

so that there is a separation of the solution in time and space. At the same time two new concentration functions appear as ${}^{a}\hat{c}(\hat{\boldsymbol{x}})$ and ${}^{b}\hat{c}(\hat{\boldsymbol{x}})$. Substitution of eq. (15) into eq. (14) leads to

$${}^{a}\hat{c}(\hat{\boldsymbol{x}})\hat{\omega} = \frac{\partial^2}{\partial x_i \partial x_i}\,{}^{b}\hat{c}(\hat{\boldsymbol{x}})\,, \tag{16}$$

and

$${}^{b}\hat{c}(\hat{\boldsymbol{x}})\hat{\omega} = -\frac{\partial^2}{\partial x_i \partial x_i}\,{}^{a}\hat{c}(\hat{\boldsymbol{x}}) \tag{17}$$

where the sine and cosine terms are independent. Equations (16) and (17) may be decoupled as

$$[{}^{a}\hat{c}(\hat{\boldsymbol{x}})]_{,iijj} + {}^{a}\hat{c}(\hat{\boldsymbol{x}})\hat{\omega}^2 = 0 \qquad\qquad [{}^{b}\hat{c}(\hat{\boldsymbol{x}})]_{,iijj} + {}^{b}\hat{c}(\hat{\boldsymbol{x}})\hat{\omega}^2 = 0 \tag{18}$$

where i=1,2 and j=1,2 and the notation $(.)_{,iijj}$ implies the fourth order spatial derivative. In addition, the solution, eq. (15) may be rewritten as

$$\hat{c}(\hat{\boldsymbol{x}},\hat{t}) = \tilde{c}(\hat{\boldsymbol{x}})\sin(\hat{\omega}\hat{t} + \varphi) \tag{19}$$

where the amplitude $\tilde{c}$ can be written as

$$\tilde{c}(\hat{\boldsymbol{x}}) = \sqrt{{}^{a}\hat{c}^2(\hat{\boldsymbol{x}}) + {}^{b}\hat{c}^2(\hat{\boldsymbol{x}})} \tag{20}$$

and

$$\varphi(\hat{\boldsymbol{x}}) = \tan^{-1}\left[\frac{{}^{b}\hat{c}(\hat{\boldsymbol{x}})}{{}^{a}\hat{c}(\hat{\boldsymbol{x}})}\right]\,. \tag{21}$$

In order to solve eq. (18), four boundary conditions for each function are required, and these are demonstrated in Paper A.

In summary, as a result of the complicated geometry of the bone cross-section, a numerical solution is required. The assumption of a time harmonic solution leads to a differential equation in space, namely eq. (18). This avoids solution of the time dependent differential equation in eq. (14), but still makes it possible to see the effect of many load cycles.

The governing equations in eq. (18) together with the boundary conditions are solved using a finite element formulation. The system is analogous to the differential equation for a plate supported by an elastic foundation with corresponding boundary conditions. Hence, the numerical analyses may be conveniently performed using a commercial finite element code for structural analysis. Results from the numerical model are shown in Figure 4. Here the normalized amplitude $\tilde{c}$ of the concentration of matter, shown in eq. (20), is presented for five different normalized load frequencies $\hat{\omega}$. It can be seen that the concentration is highest at the outer boundary, the nearly impermeable periosteum. Recall that bone growth takes place at the bone surfaces. The results for moderate frequencies

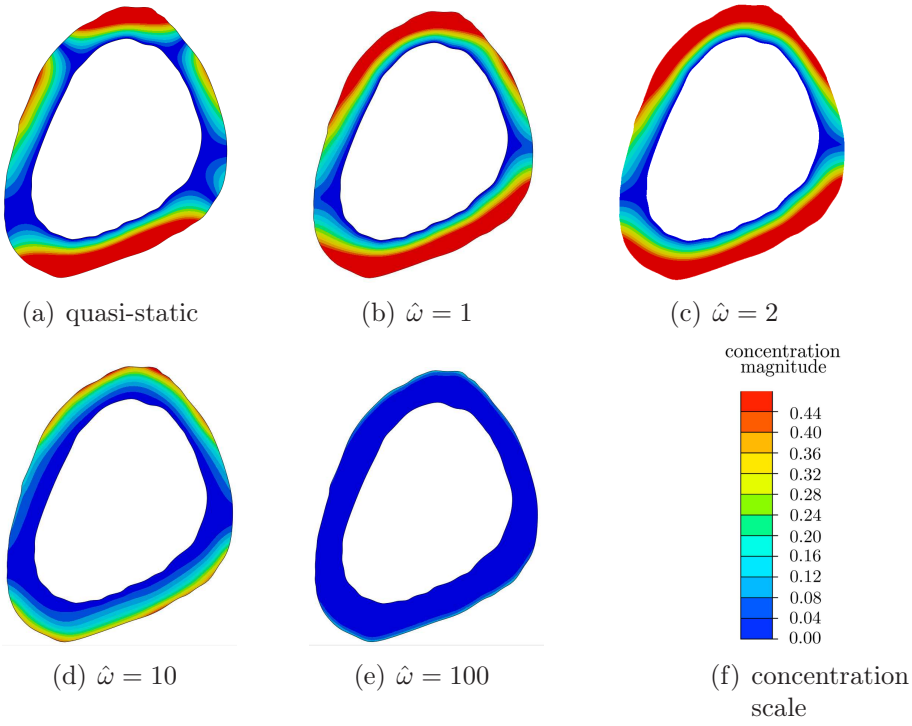

(a) quasi-static (b) $\hat{\omega} = 1$ (c) $\hat{\omega} = 2$

(d) $\hat{\omega} = 10$ (e) $\hat{\omega} = 100$ (f) concentration scale

Figure 4: Normalized concentration amplitude $\tilde{c}$ in eq. (20) distributed over the bone cross-section for different non-dimensional load frequencies $\hat{\omega} = \omega a^2/D$, cf. Paper A.

with $\hat{\omega}$ being 1 or 2, displayed in Figures 4b and 4c, show that the concentration also becomes large over extended regions of the bone cross-section. Close to the medullary cavity, as well as in two locations (dark blue color) near the lower part of the cross-section, the concentration vanishes.

It seems to exist an optimal load frequency for maximizing the concentration of matter at the periosteum. The optimum for this particular geometry seems to be between $\hat{\omega} = 1$ and $\hat{\omega} = 10$, possibly close to $\hat{\omega} = 2$, as can be seen in Figure 4. For $\hat{\omega} = 10$ and thereafter the amplitude is considerably lower. In Paper A the equations and results are presented and discussed more in detail. Comparison with the experiment results from Lanyon and Rubin (1984) are also made.

The model shows where bone growth should occur for loading around the x_1-axis (if treated as the neutral axis), and how the growth depends on load frequency. The concept can be developed by including the development of the bone cross-section and by investigating other load cases.

4 Development of the cross-section

To model the development of the cross-section, a Ginzburg-Landau partial differential equation system is utilised. The concept is based on a phase variable that keeps track of the material properties during the evolution of the bone. The relevant free energies are assumed to be elastic strain energy, gradient energy due to difference in concentration of matter and a double well chemical potential. It is believed that nutrients are transported from the existing cortical bone and out to the periosteum where bone building osteoblast are activated. The activation process is assumed to include release of free mechanical energy and dissipation of chemical energy. The chemical energy potential describe the motion on the microscopic level towards local states with minimum potential energy which in the present study are either the organized bone structure or a disintegrated non-solid state. This is considered to be in analogy with solid-viscous or solid-gaseous system where the phases are kept apart by a barrier of higher potential energy. Erwin Schrödinger's idea (Schrödinger, 1944) of living cells that seemingly decrease the entropy (as opposed to non living material) is used in this two-dimensional phase-field model. Schrödinger's idea is included by giving the strain energy a negative weight factor m, i.e., high strain energy would trigger the recruitment of material rather than dissolving it.

The phase field variable $\psi{=}\psi(\boldsymbol{x}, t)$ is used to keep track of the solid state, i.e., the bone. The phase field variable will from here on only be written as ψ since the dependence on space and time will be valid through all equations. To simplify the mathematical presentation, ψ is limited to the interval $|\psi| \leq 1$, where $\psi = -1$ defines the absence of bone and $\psi = 1$ defines fully developed bone. The fully developed phase is suggested to be a dense cortical bone. For this reason ψ is mostly close to 1 or -1, i.e. bone or not bone. There is a region where the material is a weak solid and not fully developed bone. For this region $|\psi| \leq 0.9$, and is called the transition zone. Focus of the growth process concerns the transition zone. It is believed in this study that the bone promoting substances are of no use as long as they appear in regions of fully developed cortical bone.

The total free energy density F is here composed of diffusion, phase and strain energies densities as follows

$$F = F_{ch} + F_{gr} + mF_{el}\,, \tag{22}$$

where the energy densities F_{ch}, F_{gr} and F_{el} here represent the chemical potential, the concentration gradient energy and the elastic strain energy respectively. Again, m is the dimensionless weight factor here supposed to be negative. The gradient energy is responsible for the diffusion of matter, and the chemical potential is the binding energy required to remove a single cell layer at the bone surface. The considered energies are functions of ψ and its gradients, $\frac{\partial}{\partial x_i}(\psi)$ from here on written $\psi_{,i}$ where the index i=1,2.

The study utilizes the Ginzburg-Landau theory to describe the development of bone tissue. The time dependent Ginzburg-Landau relation may be written

$$\frac{\partial}{\partial t}\psi = -L_\psi \frac{\delta}{\delta \psi} F\,, \tag{23}$$

where $\frac{\delta F}{\delta \psi}$ is the variation of F with respect to variation of the material state ψ (cf. Ginzburg and Landau (1950)). Here $F = F(\psi, \psi_{,i})$, from here on only written F. Gradients of higher order than $\psi_{,i}$ are assumed to be insignificant. The mobility coefficient

L_ψ is a positive constant. The Euler-Lagrange equation can be used to express the right hand side term in eq. (23), i.e. the variation of F, as

$$\frac{\delta}{\delta\psi}F = \frac{\partial}{\partial\psi}F - \frac{\partial}{\partial x_i}\frac{\partial}{\partial\psi_{,i}}F \,. \tag{24}$$

The chemical energy potential, also called the Landau potential (Ginzburg and Landau, 1950), should fulfil the condition $\partial F_{ch}/\partial\psi \to 0$ as $|\psi| \to 1$ to prevent $|\psi|$ from exceeding 1. On its simplest polynomial form it is written for two phases,

$$F_{ch} = p(\frac{1}{4}\psi^4 - \frac{1}{2}\psi^2) \,, \tag{25}$$

where p is a material parameter. The expression has minima at $|\psi| = 1$ and the potential strives to bring the state, ψ, towards any of the two minima.

The gradient energy is, with index notation using Einstein's summation rule, written as

$$F_{gr} = \frac{g_b}{2}\psi_{,i}\psi_{,i} \,. \tag{26}$$

The constant g_b is a material parameter which affects the width of the transition zone. The gradient energy F_{gr} creates diffusion. The driving force is towards decreasing gradients until the gradients and the gradient energy vanish.

The strain energy for a linear elastic behaviour is in general formulated as

$$F_{el} = \frac{1}{2}\sigma_{ij}\epsilon_{ij} \,. \tag{27}$$

The stress state is also here uniaxial for pure bending and uniaxial tension, and the only stress component, σ_{33}, is the stress normal to the studied bone cross-section. Therefore the stresses depend only on Young's modulus in the x_3-direction, E, which is a function of the material state ψ. Should the bone vanish then Young's modulus is expected to vanish and, reversely, for fully developed bone it should assume the value E_b. The released strain energy provides a driving towards fully dense bone, which vanishes when the material is in a stable configuration. Therefore it is required that $\partial F_{el}/\partial\psi \to 0$ for $|\psi| = 1$. The simplest polynomial form is

$$E = \frac{1}{4}(2 + 3\psi - \psi^3)E_b \,. \tag{28}$$

Poisson's ratio is not required in the present study.

Two load cases are evaluated; Bending around the minor centroidal axis of the cross-section (Figure 3b), for which the weakest bending response is given, and bending around the x_1-axis, treated as a neutral axis. In both load cases the only occurring stress component hence will be the out-of-plane stress σ_{33}.

Further the bone is treated as transversely isotropic with a principal axis in the x_3 direction, i.e. $\sigma_{33} = E\epsilon_{33}$ where E is the principal stiffness in the x_3 direction. The elastic strain energy in eq. (27) becomes

$$F_{el} = \frac{1}{2}E(\psi)\epsilon_{33}^2 \,, \tag{29}$$

and $E(\psi)$ a function of ψ according to eq. (28).

By inserting eqs. (25), (26) and (29) into eq. (24), and then make use of eq. (23) the following is readily obtained as

$$\frac{\partial}{\partial t}\psi = -L_\psi\Big(p(\psi^2-1)\psi - g_b\psi_{,ii} - \frac{3}{8}m\epsilon_{33}^2 E_b(\psi^2-1)\Big)\,. \tag{30}$$

In the main load case, i.e. bending around the minor centroidal axis of the cross-section, for which the weakest bending response is given, the strain in an arbitrary point becomes $\epsilon_{33}=\frac{1}{R}[x_1^*\cos(\varphi)+x_2^*\sin(\varphi)]$. The quantity $x_1^*\cos(\varphi)+x_2^*\sin(\varphi)$ becomes the perpendicular distance from the point to the minor centroidal axis if φ is the angle to the major centroidal axis, i.e. if $\varphi=\varphi_1$. R is the bending radius of the bone and x_1^* and x_2^* are the coordinates in the current system $x_1^*-x_2^*$ having the *current* mass center of the cross-section as the origin of the space. The angle to the major centroidal axis, φ_1, of the cross-section is found by using the second moment of area tensor for the cross-section. The mass center and the second moment of area tensor are continuously updated as the bone develops. In the second case where the load is applied around the x_1-axis, the strain becomes $\epsilon_{33}=\kappa x_2$. Let $z=x_1^*\cos(\varphi)+x_2^*\sin(\varphi)$ for the main case and let $z=x_2$ for the second load case. Now the strain is alternatively

$$\begin{gathered}\epsilon_{33}=\kappa z\,,\quad \text{with}\\ z=\begin{cases} x_1^*\cos\varphi + x_2^*\sin\varphi & \text{main case}\\ x_2 & \text{second case.}\end{cases}\end{gathered} \tag{31}$$

For convenience dimensionless variables are introduced. A length unit a [L] is introduced. In the selected shape a is the average bone wall thickness. By also introducing a time unit τ [T], non-dimensional variables may be selected as follows,

$$\tau=\frac{a^2}{L_\psi g_b},\ \hat{t}=\frac{t}{\tau},\ \hat{x}_i=\frac{x_i}{a},\ \hat{z}=\frac{z}{a},\ \hat{R}=\frac{R}{a},\ \hat{\kappa}=\frac{1}{\hat{R}}\sqrt{\frac{3E_b}{8p}},\ \text{and}\ \lambda=\frac{pa^2}{g_b}\,. \tag{32}$$

Now eq. (30) is written

$$\frac{\partial}{\partial\hat{t}}\psi - \frac{\partial^2}{\partial\hat{x}_i\partial\hat{x}_i}\psi = \Big(\psi - m\hat{z}^2\hat{\kappa}^2\Big)(1-\psi^2)\lambda\,. \tag{33}$$

As observed the left hand side of eq. (33) is Fick's second law for the continuous quantity ψ with a diffusion coefficient which is independent of concentration and spatial coordinates. The right hand side represents driving force sources or sinks. The equation is also in analogy with Fourier's law with heat sources on the right hand side of eq. (33), which widens the range of numerical codes that can be used for the calculations.

With a selected negative value of m both right hand terms are contributing to $\partial\psi/\partial t$ for $\psi>0$ meaning that both terms then act together to form bone structure.

The development of the whole bone cross-section and the development at some specific locations are investigated. In Paper B the influence on the numerical solution of the initial thickness b_o of the transition zone -1<ψ<1 is also investigated. A suitable thickness is found to be $b_o=2b_{ref}=2\frac{a}{18}$, cf. Paper B. In Figure 5 the positions (A) and (B) are shown

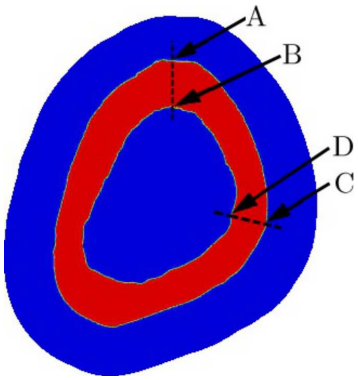

Figure 5: a) The position of cuts AB and CD across the bone wall, cf. Paper B.

which are evaluated in Figure 6. In Figure 6a the movement of periosteum at (A) during loading is shown for three different load amplitudes. Since high strain energy is modelled to contribute to bone formation the results are expected. Higher load (i.e. smaller bending radius $\hat{R}$) gives faster development of the bone. In Figure 6b the rate of the movement of the position where ψ=0, at a specific time, as a function of the load is shown for both (A) and (B). I.e. for both the periosteum and the endosteum at the cut A-B. The results are for the case with bending around the minor centroidal axis of the cross-section. The graphs reveal three different regions I) small loads ($9000<\hat{R}$) give resorption on both the periosteum and endosteum, II) intermediate loads ($4500<\hat{R}<9000$) give resorption at the inner surface and growth at the outer surface and III) large loads ($\hat{R}<4500$) give growth at both surfaces. At around $\hat{R}$=5000 the growth rate at the outer surface and the resorption at the inner surface are equal meaning that the wall thickness is maintained while the bone diameter is increasing.

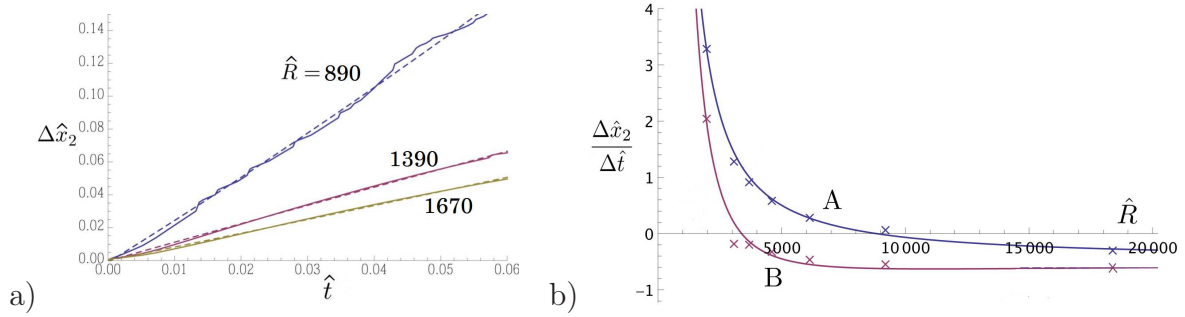

Figure 6: a) The vertical movement (i.e. along x_2) of ψ=0 at position (A) for b_o=$2b_{ref}$ for different loads. b) Growth rate versus load at positions (A) and (B) for b_o=$2b_{ref}$. Note that positive rate at the endosteum (B) means that the diameter of the medullar cavity is decreasing, i.e. (B) is then moving inwards towards the cavity, cf. Paper B.

In Figure 7 results are displayed for a transitions zone of $b_o = 2b_{ref}$ for the case with bending around the minor centroidal axis of the cross-section. In Figure 7a the undeformed geometry is displayed where the initial loading axis (the minor centroidal axis giving the weakest bending response) is shown together with the initial mass center of

the bone section. In Figure 7c the transition zone at point C (c.f. Figure 5a) is displayed at $\hat{t}$=0.005 for the deformation $\hat{R}$=890. The development of the full cross-section from three different bending deformation levels are then showed in Figure 7d, e) and f) at time $\hat{t}$=1, i.e. at times not discussed earlier. Here the bone growth appears to almost have stopped at about $\hat{t}$=0.4 as seen in Figure 8.

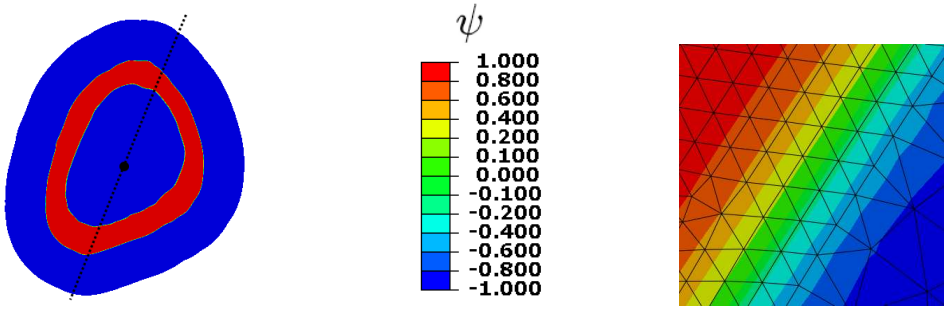

(a) Undeformed.

(b) Phase; 1 for bone and -1 for empty space.

(c) Transition zone at point C (cf. Figure 5) at $\hat{t}$=0.005 for $\hat{R}$=890.

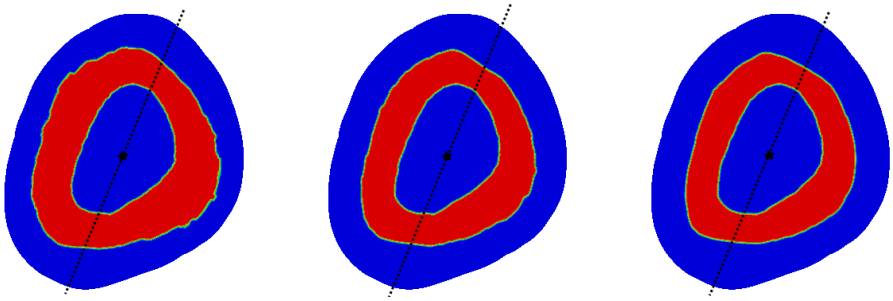

(d) $\hat{R}$=890 at $\hat{t}$=1.

(e) $\hat{R}$=1390 at $\hat{t}$=1.

(f) $\hat{R}$=1670 at $\hat{t}$=1.

Figure 7: Results for different $\hat{R}$ for $b_o = 2b_{ref}$ for bending around the minor centroidal axis giving the weakest bending response, cf. Paper B.

It is obvious that a more aggressive bending, i.e. higher loading, results in eventually more bone growth, as expected. It is also obvious that the bone growth appears to be highest where the strain energy is high, but the areas close to the minor centroidal axis differs in growth rate between the results. For the case with the largest bending, i.e. $\hat{R}$=890, there still is some bone growth taking place here even though the strain energy is zero here, but for the two other cases with lower loading the bone resorbs here.

In Paper B more results and numerical considerations are evaluated in detail.

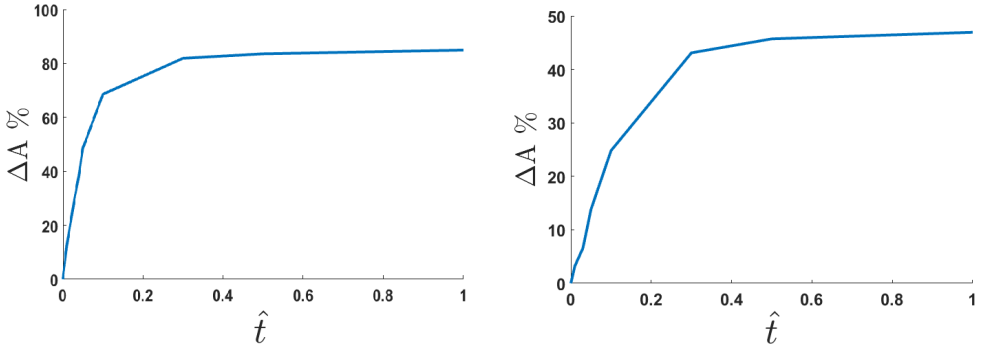

(a) $\hat{R}$=890. (b) $\hat{R}$=1670.

Figure 8: Area increase of the cross-section for two of the cases for $b_o = 2b_{ref}$, cf. Paper B.

5 Using the motion of ions to determine diffusion coefficients

To translate the numerical results to real loads and load frequencies, actual values of the material parameters must be known. Among them, the diffusion coefficient of diffusing matter in the transverse plane in the bone tissue. A method is developed to, in a fairly easy accessible way, determine a diffusion coefficient in the radial direction of cortical bone with high accuracy.

A part of the mid-shaft of a right femur bone of a 15 month old male bovine of type Charolais was four days after slaughter step by step cut in to small bone cubes approximately of size 1 cm^3 giving a total of 16 pieces. The pieces were taken from four different locations over the cross-section, see Figure 9a.

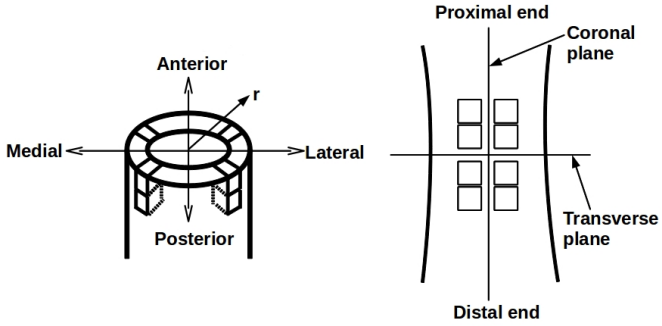

Figure 9: Location of samples, cf. Paper C.

At each location two pieces were taken above the midplane (being the transverse plane on the middle of the diaphysis), and two below, see Figure 9b. In each row the samples were numbered from 1 to 4, where 1 is the sample closest to the proximal end and 4 closest to the distal end. Eight pieces were taken from the lateral side (outside), where four of them were located slightly towards the anterior side (front side) and the other four were

located slightly towards the posterior side (back side). The other eight were taken from the medial side (inside), where four of them were located slightly towards the anterior side and the other four were located slightly towards the posterior side. KCl was chosen as diffusing matter since it has a high ability to conduct electricity, hence being suitable to use in conductivity measuring giving a strong read, along with the linear relationship between concentration and conductivity giving an easy mathematical approach.

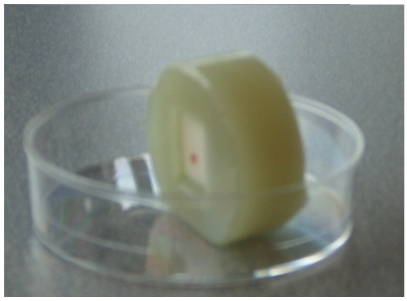

(a) Prepared bone sample

(b) The equipment; Seven Easy S30 from Mettler Toledo

Figure 10: Prepared bone sample and the equipment used for the experiment, cf. Paper C.

The bone pieces were put in beakers with saturated KCl solution for 24 hours exposing them to a very high concentration, after which they were quickly rinsed with distilled water, lightly wiped with paper and then molded in polyester in order to close the axial and tangential directions leaving only the radial direction ends opened, see Figure 10a. To measure the conductivity the instrument SevenEasy S30 from Mettler Toledo was used along with a cell that had two electrode plates, see Figure 10b. The samples were put in beakers with 100 ml distilled water in which the conductivity was frequently measured during 24 hours. The temperature in the water was held constant at 22^oC by placing the beakers on a temperature controlled plate. The conductivity of the water increased due to the ions of the KCl that diffused out from the sample and into the water.

In the experiment the diffusion in the radial direction of the bovine cross-section was examined. Hence the problem is one-dimensional. For the one-dimensional case, with the Cartesian spatial variable now being r, the following equation can be a solution to the one-dimensional Fick's second law with a constant diffusion coefficient,

$$c(r,t) = X(r)T(t)\,, \tag{34}$$

where the most general solution is given as (Crank, 1975),

$$c = \sum_{m=1}^{\infty} \Big(A_m \sin(\lambda_m r) + B_m \cos(\lambda_m r) \Big) e^{(-\lambda_m^2 Dt)}\,. \tag{35}$$

Each bone sample had a volume of approximately $1/100$ of the surrounding water. The concentration increase in the water was considered to be very low, in comparison to the

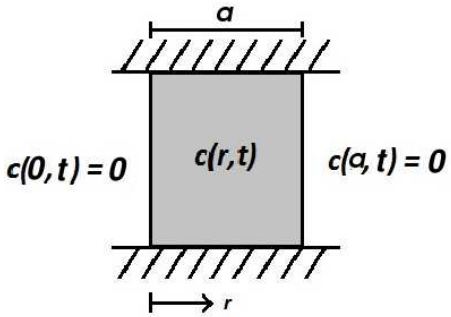

Figure 11: One-dimensional slab, cf. Paper C.

difference in concentration between the water and the bone sample, and hence ignored. The boundary conditions were hence modeled as constant. For a one-dimensional slab having the constant boundary conditions $c = 0$ at the boundaries $r = 0$ and $r = a$, and an initial concentration of c_o at $t = 0$ for $0 < r < a$, see Figure 11, the solution becomes

$$c(r,t) = c_o \sum_{n=1}^{\infty} A_n \sin\left[\lambda_n r\right] e^{-\lambda_n^2 Dt} \,, \tag{36}$$

where

$$\begin{aligned} A_n &= \tfrac{4}{\pi}\tfrac{1}{(2n-1)} \\ \lambda_n &= (2n-1)\tfrac{\pi}{a} \,. \end{aligned} \tag{37}$$

By taking the integral of eq. (36) over r and then divide it by the integration length a the mean value $\tilde{c}_b$ of the concentration in the bone sample is given. This is shown in the following expression,

$$\tilde{c}_b(t) = c_{bo} \frac{1}{a} \sum_{n=1}^{\infty} A_n \int_0^a \sin(\lambda_n r) \mathrm{d}r \; e^{-\lambda_n^2 Dt} \,, \tag{38}$$

where index b is for bone. Deriving the integral the following expression is readily given,

$$\tilde{c}_b(t) = c_{bo} \sum_{n=1}^{\infty} \frac{8}{\pi^2 (2n-1)^2} e^{-((2n-1)\frac{\pi}{a})^2 Dt} \,. \tag{39}$$

The conductivity ξ in the distilled water surrounding the bone sample was registered over time. The mean conductivity $\tilde{\xi}_w$ of the distilled water is modeled as

$$\tilde{\xi}_w(t) = A - B \sum_{n=1}^{\infty} \frac{8}{\pi^2 (2n-1)^2} e^{-((2n-1)\frac{\pi}{a})^2 Dt} \,. \tag{40}$$

Here A [S/l] is the final value of the conductivity, i.e. the conductivity after a long time, since the dimensionless summation converges towards zero. $A - B$ is the start value,

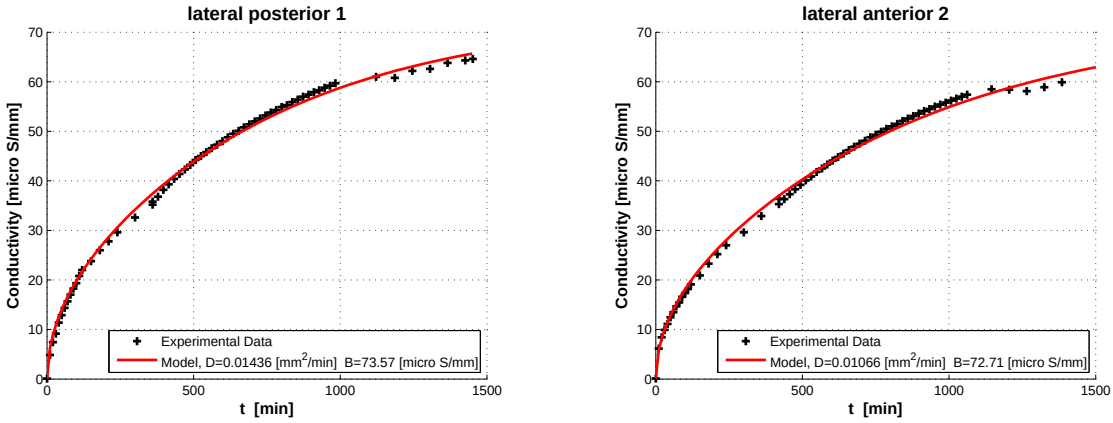

(a) Lateral posterior 1.

(b) Lateral anterior 2.

Figure 12: Experimental data and analytical function for samples from the lateral posterior (a) and anterior (b) side, cf. Paper C.

i.e. $\xi_{t=0}$, since the summation equals 1 for $t = 0$. $A - B$ is obtained from the very first measuring at t_0. The expression in eq. (40) is fitted to the experimental data by means of a Kalman filter.

The over all average value and the standard deviation of the extracted diffusion coefficient D for all bone samples become $D = 0.0110 \pm 0.0069$ mm^2/min, or $D = 1.83 \pm 1.15 \cdot 10^{-10}$ m^2/s. Differences between the samples were as expected observed. For the lateral posterior sample no. 1, LP_1, the diffusion coefficient was for instance found to be 0.014360 mm^2/min and for sample no. 2 from the lateral anterior side, LA_2, it was determined to 0.010660 mm^2/min. The fitted conductivity curves using the values of the diffusion coefficient from the Kalman filtering method are presented in Figure 12, and as can be seen the model has a good match with the experimental data.

In Paper C the theory, experiment set-up and more about the results are described. Comparison with other studies are also made.

6 Calculating effective material parameters of bone

So far the possibility to numerically calculate the required loading, along with how to determine input to the numerical models, have been presented. In a final step a method to look and evaluate the physiological status of a bone is developed. The porosity of a bone can be measured *in vivo* by computed tomography. Relatively high porosity means in general degenerated or unhealthy bone. However, looking only at the porosity of the bone may not be sufficient to determine the physiological performance of it. The shape of the pores and their orientation, and not only the size, influence the flux of nutrients and the stiffness of the bone as well. A method is developed where the diffusion coefficient and the Young's modulus of the bone can be determined by looking only at a small section of the full cross-section of a bone. The chosen section must be representative for the full section regarding number of pores per unit area along with the size, shape

and orientation of the pores. With image analysis tools a representative section of a bone cross-section can be analysed and typical pore shapes can be identified. Then by using the here suggested equation, the effective diffusion coefficient and effective Young's modulus can be calculated. The approach with an analytical solution can be far more efficient than the numerical approach using finite element method, since it would require extremely small elements to model the cross-section with the pores with good precision, and also requires the knowledge of finite element approach. Some shape parameters must be determined once using finite element method for typical pores, which then can be stored in a data base which will act as input to analytical approach.

Consider a body containing a single pore. The material surrounding the pore is called the matrix. In the pore, the diffusion coefficient is set to D_p and in the matrix the diffusion coefficient is set to D_m. A two-dimensional flow of matter that is driven by the concentration gradient is considered.

In the present study steady-state solutions, i.e., $\partial c/\partial t = 0$ are sought. The consequence is that the flux will be divergence free, i.e. Fick's second law becomes

$$\frac{\partial}{\partial x_i}[D\frac{\partial}{\partial x_i}c(\boldsymbol{x},t)] = 0\,. \tag{41}$$

In Paper D an expression for the effective diffusion coefficient D_e over a studied section with the width w and hight h is deducted to be

$$D_e = D_m\left(1 + \frac{s}{hw}\sum_{i=1}^{N}\frac{\tilde{\theta}^{(i)}A_p^{(i)}}{1 - s\kappa^{(i)}\sqrt{\frac{A_p^{(i)}}{hw}}}\right), \tag{42}$$

where

$$s = 1 - \frac{D_m}{D_p}\,. \tag{43}$$

and A_p is the area of the current pore i. The summation is performed for N pores where the contribution of each pore i is superpositioned which may only be allowed if the pores are sufficiently small. More precisely, the linear extent of the pore must not exceed 30% of the linear extent of the total studied section. I.e $\sqrt{\frac{A_p}{hw}}$ <0.3 for the model to be valid. The geometry factors $\tilde{\theta}^{(i)}$ and $\kappa^{(i)}$, which are functions of the shape, area and orientation of pore i, must be determined beforehand and stored in a data base. Finite element calculations for one and each of the relevant pores are performed, and by studying the influence of size, shape and orientation of the pore to the flux, $\tilde{\theta}^{(i)}$ and $\kappa^{(i)}$ can be established for the current pore i. In Figure 13 an example of the finite element model used to determine $\tilde{\theta}^{(i)}$ and $\kappa^{(i)}$ is shown. The shape of the pore is seen in the middle.

In the same way, an expression for the effective elasticity modulus is determined. To follow the conventional tensor notation, the stresses are written as σ_{ij}, the strains as ϵ_{ij} and the displacements as u_i. The stresses are given by Hooke's law as

$$\sigma_{ij} = \frac{E}{1+\nu}(\epsilon_{ij} + \frac{\nu}{(1-2\nu)}\delta_{ij}\epsilon_{kk}) \tag{44}$$

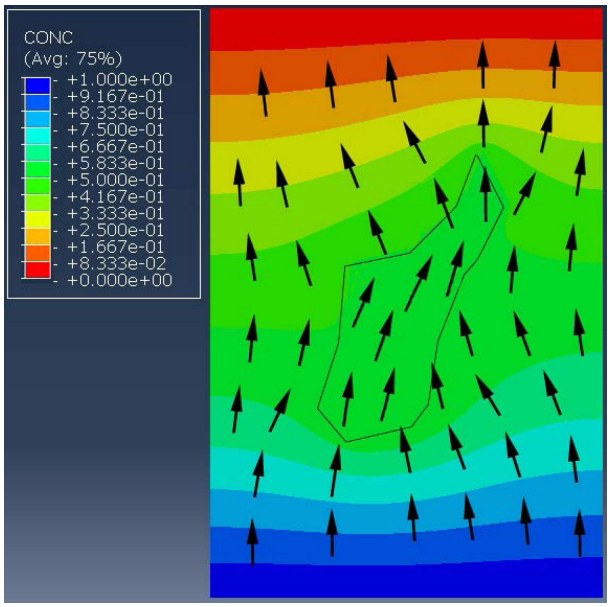

Figure 13: Distribution of the concentration. The nominal flux is vertical. The contour shows a pore named C', cf. Figure 14, with an around 20 000 times larger diffusion constant than the surrounding bone, cf. Paper D.

and the strains ϵ_{ij} are defined by

$$\epsilon_{ij} = \frac{1}{2}(u_{i,j} + u_{j,i})\,. \tag{45}$$

The equations of equilibrium, $\sigma_{ij,j} = 0$, after insertion of Eqs. (44) and (45) give the equation

$$u_{i,jj} + \frac{1}{1-2\nu} u_{j,ij} = 0. \tag{46}$$

Eq. (46) governs the linear elastic behaviour of the body. In order to introduce the reduction of stiffness due to a pore, the M-integral is used, which is defined as

$$M = \int_{\Omega} \left(W n_i - T_j \frac{\partial u_j}{\partial x_i} \right) x_i \mathrm{d}\Gamma\,, \tag{47}$$

where W is the elastic energy density, n_i is the unit normal to Ω which is directed to the right relative to the direction of the path Γ in the x_1-x_2 plane, T_i are the tractions acting on the material to the left of Ω relative to the direction of Γ and u_i are the displacements. Using the M-integral the effective modulus of elasticity E_e for a large body with multiple pores may be calculated using the same superposition principle as for the diffusion case, cf. eq. (42). The calculation is performed as

$$E_e = E_m \left(1 - \frac{1}{hw} \sum_{i=1}^{N} \tilde{\theta}_E^{(i)} \left(b^{(i)} \right)^2 \right), \tag{48}$$

where the summation is performed for N pores. The geometry factor $\tilde{\theta}_E^{(i)}$ are chosen for sufficiently small pores and for a corresponding shape.

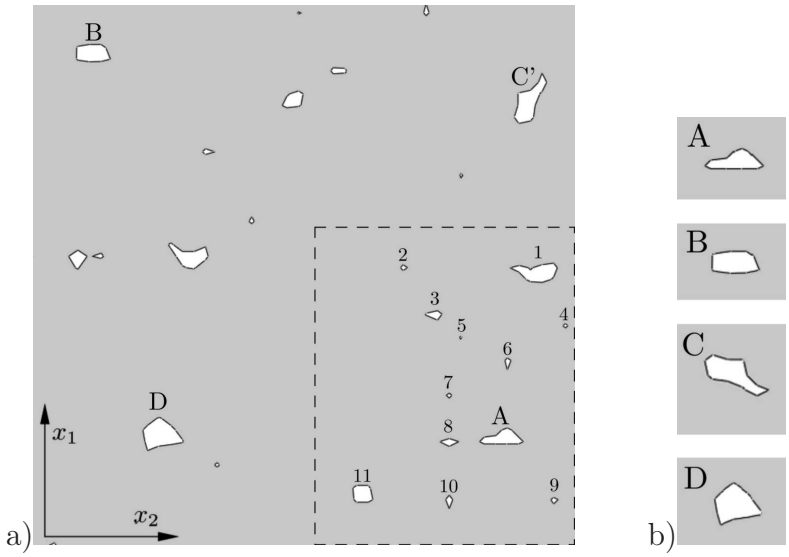

Figure 14: a) A $0.22 \times 0.20\,\mathrm{mm}^2$ part of a $10 \times 10\,\mathrm{mm}^2$ bovine ulna sample (Ståhle, Persson and Isaksson, 2013). Evaluation is performed on the region marked with dashed edges. b) detailed view of the selected pores. Cf. Paper D.

The method is tested for the area marked with the dashed line in Figure 14. It is assumed that for each and one of the pores in the region, one of the pores A-D or A'-D' (A-D rotated 90^o), can be used as a fair representation. The $\tilde{\theta}^{(i)}$, $\kappa^{(i)}$ and $\tilde{\theta}_E^{(i)}$ are determined by using finite element method for one pore at a time for A-D' as in Figure 13 for C'. Then the two main equations eq. (42) and eq. (48) are used and an effective diffusion coefficient D_e and Young's modulus E_e are determined for the region. A full scheme finite element calculation is performed for the region, including all pores as they are in the dashed region in Figure 14. The effective diffusion coefficient of matter and the effective Young's modulus are determined by studying the flux and the displacements respectively from the finite element results. Compared with the finite element results, a difference of 0.3% of the diffusion coefficient and of 0.7% of the modulus of elasticity is found. In both cases the superposition method gives smaller values of Young's moduli than the finite element method. The method is carefully presented in Paper D where all assumptions needed during the development of the equations are given.

7 Discussion

With the first numerical model an optimal loading frequency can be determined. Looking at eq. (12), there is also a relationship between applied moment and given concentration of matter. Higher applied moment gives higher concentration over the cross-section. Possibly there exists a threshold value for which the applied moment is too low giving too low increase of concentrations for promoting bone growth, regardless of load frequency. This assumption is strengthen by the results from the second numerical model, where low loads give a decrease of the cross-section area.

The mean value from the conductivity experiment, $D = 1.8 \cdot 10^{-10}$ m^2/s for KCl in bovine cortical bone, can be used in the first numerical model, where the relation for an optimal loading frequency for maximizing bone growth is $\omega \approx 2\frac{D}{a^2}$. The scaling factor a, being the average thickness of the bone wall thickness, must be chosen to calculate an actual loading frequency ω. For a human mid-diaphysis femur, a can be chosen as 0.007 m, which gives the time for a full sinusoidal load cycle, i.e. bending back *and* forth, to 10 days. For a bovine with a=0.015 m, several weeks. Even though regular training occurs as half load cycles, the here optimum frequency is unlikely to be reached, consequently it could be suggested that the longer the load cycles, the better if stronger bones are desired. The results suggest that very high load frequencies, e.g. running, is not the best way to optimize bone remodeling.

As seen in eq. (32) the time scaling in the second numerical model becomes $\hat{t}=\frac{tL_\psi g_b}{a^2}$. The quantity $L_\psi g_b$ is the diffusion coefficient D. It was seen that for the least aggressive evaluated load ($\frac{R}{a}$=1670, cf. Figure 8b), 10% growth was reached after $\frac{tL_\psi g_b}{a^2}$=0.05. With a chosen as 0.007 m, for a human femur and D again $1.8 \cdot 10^{-10}$ m^2/s, the actual time it would take to receive 10% growth then becomes about 4 hours. I.e. 4 days if work out takes place for one hour a day.

With a chosen as 0.015 mm, for a bovine femur, the actual time it would take to receive 10% growth then becomes about 17 hours. These exercise times are very short and suggest that important substances for bone growth have smaller diffusion coefficients. For instance, important substances for the remodelling process are the prostaglandins, e.g. prostaglandin E2 (PGE-2) (Jee et al., 1990) and the proteins BMP-2 (Wutzl et al., 2010). PGE-2 has a molecular weight of about 350 Da, and BMP-2 about 40 kDa. In the study by Patel et al. (2005) diffusion coefficients for tracers with different sizes were investigated. The 300 Da tracer in that study had a diffusion coefficient in the transverse direction of bovine cortical bone of D=$7 \cdot 10^{-14}$ m^2/s. With this value the exercise time for a human would be 405 days. If a person exercise one hour a day, it would take about 27 years to reach 10% growth. For the most aggressive load ($\frac{R}{a}$=890) the exercise time becomes 81 days, or about 5 years with one hour work out per day. For a bovine the same figure becomes 24 years.

The results indicates that mechanical loading should be applied with high load and low loading frequency.

8 Conclusions

In the first numerical model in this thesis an optimal loading frequency for an oscillating load can be determined to $\omega \approx 2\frac{D}{a^2}$ for times $\frac{D}{a^2}t \gg 1$, as seen in Figure 4c. The optimum loading frequency maximizes concentration of matter for an avian ulna cross-section. It is likely that this value would not differ substantially if the geometry is changed. As may be observed, the bone growth is rather diffuse and does not necessarily occur at the parts of the cross-section that are most distant from the neutral axis. Instead growth is spread out around the bone. The results for the limiting quasi-static case $\frac{a^2}{D}\omega \ll 1$ in Figure 4a is interesting since it infers that an almost purely static load still can promote bone growth.

The second numerical model reveals three different regions. Firstly, small loads give resorption on both the periosteum and endosteum. Secondly, intermediate loads give resorption at the inner surface and growth at the outer surface, and thirdly, large loads give growth at both surfaces. At a specific load the growth at the outer surface and the resorption at the inner surface are equal meaning that the wall thickness is maintained while the outer bone diameter is increasing.

In the conductivity experiment the diffusion coefficient of KCl in bovine bone was determined to $D = 1.8 \cdot 10^{-10}$ m^2/s. KCl has a weight of 74 Da (39 for potassium and 35 for chloride). It was assumed that the KCl diffused as separate ions through the micro porosity of the cortical bone. The method has good precision comparing analytical solution and experimental data. The value might be used to determine the diffusion coefficient of other substances in bone tissue with the same molecular weight.

The final method developed gives values for the diffusions coefficient D and Young's modulus E based on the amount of pores over a cross-section and their shape and size. The analytical solution gives values close to the full scheme finite element analyses. The calculated effective material parameters are believed to be a help in evaluating the physiological status of the bone. The method will be fast once the pre-work with establishing the parameters used in the equations have been calculated via finite element method. If the developed method is complemented by an image analysing algorithm, identifying shapes and orientations of pores, and then picking the correct parameters from the database, the approach can be fully automatized.

9 Summary of appended papers

Paper A The role of stress gradients in driving diffusion of nutrients and signal substances in skeletal bones is investigated. The hypothesis is that substances that promote bone growth are transported from the medullary cavity to the outer surface of the long skeletal bone by stress driven diffusion. The equation used is the well-known Fick's law generalized to include a stress gradient term. An expression being a solution to Fick's second law is deducted finding an analogy with the solution to a plate on elastic foundation. The stress gradient is constant and the variation of the concentration is assumed to be small, and the stress dependence appear as boundary conditions. The problem is numerically solved for the specific geometry. Due to the analogy with an elastic problem it is possible to introduce the complex boundary conditions and solve the problem using a finite element solver. The results are compared to the experimental findings by Lanyon and Rubin (1984).

Paper B A Ginzburg-Landau partial differential equation system is utilised to study the change of size and shape of a cross-section caused by mechanically enhanced bone growth. The concept is based on a phase variable that keeps track of the body shape during the evolution of the bone. The relevant, fully coupled, phenomena are the elastic strain energy, concentration gradient energy and a double well chemical potential. The partial differential equation is solved numerically for the same geometry as in Paper A using a finite element method. The approach allows the bone cross-section to update and develop during the analysis. The governing equation may be compared to Fick's second law with an included chemical potential and stress gradients. The equation is also in analogy with Fourier's law with heat sources which widens the range of numerical codes that can be used for the calculations. Bending in both moving and fixed directions is investigated regarding reshaping and growth rates.

Paper C A method of determining the diffusion coefficient of a substance in bovine bone tissue is developed. The aim of the study is to determine a diffusion coefficient of a substance in bovine bone with high accuracy. By means of an experiment using a regular conductivity meter following parameter identification using Kalman filtering it is possible to in an easily assessable way determine a diffusion coefficient. The obtained diffusion coefficient is compared to other experimental findings where more complex instruments were used.

Paper D A method to determine an effective diffusion coefficient of diffusing matter and an effective elasticity modulus of the bone is developed. The method uses an analytical approach which ends up in two main equations which can be used in combination with image analysis of e.g. images from CT-scans. A hypothesis is made that studying the two material parameters is a better instrument for analysing the physiological status of the bone rather than just studying the porosity from a CT-scan. The values of the effective diffusion coefficient and the effective elasticity modulus can be used as a reference of the healthiness of the bone.

References

Banks-Sills, L., Ståhle, P., Svensson, I., Eliaz, N. (2011) 'Strain driven transport for bone modeling at the periosteal surface', *Mathematical Bioscience*, 230(1):37-44.
DOI: 10.1016/j.mbs.2010.12.008

Bilezikian, J.P., Raisz, L.G., Martin, J.T. (2008) '*The Principles of Bone Biology (third edition)*', Online version, Elsevier Inc. Accessed on the 29th of March 2018
https://www.sciencedirect.com/science/book/9780123738844

Cowin, S.C. (2001) '*Bone mechanics handbook (second edition)*', CRC Press, Boca Raton, FL, USA.

Crank, J. (1975) '*The Mathematics of Diffusion*', Oxford University Press Inc, Oxford, UK.

Currey, J.D. (2002) '*Bones*', Princeton University Press, New Jersey, USA.

Einstein, A. (1905) 'On the motion of small particles suspended in liquids at rest required by the molecular-kinetic theory of heat. (Über die von der molekularkinetischen Theorie der Wärme geforderte Bewegung von in ruhenden Flüssigkeiten suspendierten Teilchen)', *Annalen der Physik*, 322(8):549-60.
DOI: 10.1002/andp.19053220806

Fernandez-Seara, M.A., Wehrli, S.L., Wehrli, F.W. (2002) 'Diffusion of Exchangeable Water in Cortical Bone Studied by Nuclear Magnetic Resonance', *Biophysical Journal*, 82(1): 522-9.
DOI: 10.1016/S0006-3495(02)75417-9

Frost, H.M. (2004) 'A 2003 update of bone physiology and Wolff's Law for clinicians', *The Angle Orthodontist*, 74(1):3-15.
DOI: 10.1043/0003-3219(2004)074<0003:AUOBPA>2.0.CO;2

Ginzburg, V.L., Landau, L.D. (1950) Zh. Eksp. Teor. Fiz. 20(1064). English translation in: 'L. D. Landau, Collected papers', Oxford: Pergamon Press, 1965.

Hert, J., Fiala, P., Petrtýl, M. (1994) 'Osteon orientation of the diaphysis of the long bones in man', *Bone*, 15(3):269-77.
DOI: 10.1016/8756-3282(94)90288-7

Isaksson, H., Comas, O., van Donkelaar, C.C., Mediavilla, J., Wilson, W., Huiskes, R., Ito, K. (2007) 'Bone regeneration during distraction osteogenesis: Mechano-regulation by shear strain and fluid velocity', *Journal of Biomechanics*, 40(9): 2002-11.
DOI: 10.1016/j.jbiomech.2006.09.028

Jee, W.S.S., Mori, S., Li, X.J., Chan, S., (1990) 'Prostaglandin E2 enhances cortical bone mass and activates intracortical bone remodelling in intact and ovariectomized female rats', *Bone*, 11(4): 253-366.
DOI: 10.1016/8756-3282(90)90078-D

Knothe Tate M.L., Niederer, P. (1998) 'A theoretical FE-based model developed to predict the relative contribution of convective and diffusive transport mechanisms for the maintenance of local equilibria within cortical bone', HTD - Vol. 362/BED - Vol. 40, *Advances in Heat and Mass Transfer in Biotechnology*, (Ed. S. Clegg) The American Society of Mechanical Engineers

Knothe Tate M.L., Niederer P., Knothe U. (1998) 'In vivo tracer transport through the lacunocanalicular system of rat bone in an environment devoid of mechanical loading', *Bone*, 22(2): 107-17.
DOI: 10.1016/S8756-3282(97)00234-2

Kufahl, R.H., Saha, S. (1990) 'A theoretical Model for Stress-generated Fluid Flow in the Canaliculi-lacunae Net Work in Bone Tissue', *Journal of Biomechanics*, 23(2):171-80.
DOI: 10.1016/0021-9290(90)90350-C

Kutz, M. (2003) '*Standard Handbook of Biomedical Engineering & Design*', The McGraw-Hill Companies, Inc, New York, USA.

Lanyon, L.E., Rubin, C.T. (1984) 'Static vs dynamic loads as an influence on bone remodelling', *Journal of Biomechanics*, 17(12):897-905.
DOI: 10.1016/0021-9290(84)90003-4

Li, JC-M. (1978) 'Physical chemistry of some microstructural phenomena', *Metallurgical Transactions A*, 9(10):1353-80.
DOI: 10.1007/BF02661808

Malo, M.K.H., Rohrbach, D., Isaksson, H., Töyräs, J., Jurvelin, J.S., Tamminen, I.S., Kröger, H., Raum, K. (2013) 'Longitudinal elastic properties and porosity of cortical bone tissue vary with age in human proximal femur', *Bone*, 53(2):451-8.
DOI: 10.1016/j.bone.2013.01.015

Marcus, R., Feldman, D., Nelson, D.A, and Clifford J. Rosen, J.D. (2008) '*Osteoporosis, (3rd Edition)*', Elsevier Academic press, online. Accessed on the 1st of May 2018
https://www.sciencedirect.com/science/book/9780123705440

Maroudas, A., Schneiderman, R., Popper, O. (1992) 'The Role of Water, Proteoglycan, and Collagen in Solute Transport in Cartilage', In: *Articular Cartilage and Osteoarthritis*, pp.355-72. Edited by Kuettner, K.E., Schleyerbach, R., Peyron, J.G.,and Hascall, V.C., Raven Press, New York, USA

McCalden, R.W., McGeough, J.A., Barker, M.D., Court-Brown, C.M. (1993) 'Age-related changes in the tensile properties of cortical bone. The relative importance of changes in porosity, mineralization, and microstructure', *The Journal of Bone and Joint Surgery*, 75(8):1193-205.
DOI: 10.2106/00004623-199308000-00009

Mirzaali, J.M., Schwiedrzik, J.J., Thaiwichai, S., Best, J.P., Michler, J., Zysset, P.K., Wolfram, U. (2016) 'Mechanical properties of cortical bone and their relationships with age, gender, composition and microindentation properties in the elderly', *Bone*, 93:196-211.
DOI: 10.1016/j.bone.2015.11.018

Nyman, J.S., Ling, H., Dong X., Wang, X. (2009) 'Differences in the mechanical behaviour of cortical bone between compression and tension when subjected to progressive loading', *Journal of the Mechanical Behaviour of Biomedical Materials*, 2(6):613-9.
DOI: 10.1016/j.jmbbm.2008.11.008

Patel, R.B., O'Leary, J.M., Bhatt, S.J., Vasanja, A., Knothe Tate, M.L. (2005) 'Determining the permeability of cortical bone at multiple length scales using fluorescence recovery after photobleaching techniques', *Proceedings of the 51st Annual Meeting of the Orthopaedic Research Society*, Washington D.C.

Piekarski, K., Munro, M. (1977) 'Transport mechanism operating between blood supply and osteocytes in long bones', *Nature*, 269(5624): 80-2.
DOI: 10.1038/269080a0

Reilly, D.T., Burstein, A.H. (1975) 'The elastic and ultimate properties of compact bone tissue', *Journal of Biomechanics*, 8(6):393-6.
DOI: 10.1016/0021-9290(75)90075-5

Schrödinger, E. (1944) '*What is life? - The Physical Aspect of the Living Cell.*', Cambridge University Press, Cambridge, UK, 1-194.

Smoluchowski, M. (1906) 'Zur kinetischen Theorie der Brownschen Molekularbewegung und der Suspensionen', *Annalen der Physik*, 21(14):756-80.
DOI: 10.1002/andp.19063261405

Ståhle, P., Persson, C., Isaksson, P. (2013) CT-images, Data set: ResearchGate
DOI: 10.13140/RG.2.1.3961.8082

Wolff, J. (1892) '*Das Gesetz der Transformation der Knochen*', Verlag von August Hirschwald, Berlin.

Wutzl, A., Rauner, M., Seemann, R., Millesi, W., Krepler, P., Pietschmann, P., Ewers, R. (2010) 'Bone morphogenetic proteins 2, 5, and 6 in combination stimulate osteoblasts but not osteoclasts in vitro', *Journal of Orthopeadic Research*, 28(11): 1431-9.
DOI: 10.1002/jor.21144

Paper A

A Two-Dimensional Model for Stress Driven Diffusion in Bone Tissue

Gustav Lindberg, Leslie Banks-Sills, Per Ståhle and Ingrid Svensson

Computer Methods in Biomechanics and Biomedical Engineering

2015 18(5):457-67

http://dx.doi.org/10.1080/10255842.2013.807507 (2013)

A Two-Dimensional Model for Stress Driven Diffusion in Bone Tissue

Gustav Lindberg[a], Leslie Banks-Sills[a,b], Per Ståhle[a] and Ingrid Svensson[a]

[a]Division of Solid Mechanics, Lund University
SE-221 00 Lund, Sweden
[b]School of Mechanical Engineering, Tel Aviv University
69978 Ramat Aviv, Israel

Abstract

The growth and resorption of bone are governed by interaction between several cells such as bone forming osteoblasts, osteocytes, lining cells and bone resorbing osteoclasts. The cells considered in this paper reside in the periosteum. Further, they are believed to be activated by certain substances to initiate bone growth. The present study focuses on the role that stress driven diffusion plays in the transport of these substances from the medullary cavity to the periosteum. Calculations of stress driven diffusion are performed under steady state conditions using a finite element method with the concentration of nutrients in the cambium layer of the periosteum obtained for different choices of load frequencies. The results are compared to experimental findings suggesting increased bone growth in the neighbourhood of relatively high nutrient concentration.

Keywords: *bone growth; diffusion; stress enhanced; finite element method; steady-state; periosteal membrane*

1 Introduction

The goal of this study is to investigate the role of stress gradients in driving diffusion processes in skeletal bones. The hypothesis is that substances that promote bone growth are transported from the medullar cavity to the outer surface of the long skeletal bone by stress driven diffusion. As a result of physiological activity, mechanical stresses occur in skeletal bones. Moreover, the literature contains many examples showing that mechanical oscillating loads stimulate bone remodeling that is prevalent in the cambium layer of the periosteum. However, the transport processes on the cell-level is not yet completely understood. Hence, the aim of this study is to analyze the interactions between mechanical loading and transport of nutrients and signal substances that affect remodeling of skeletal bones. The results have implications on such mechanisms as fracture healing, as well as on the medical treatment of disorders including osteoporosis.

It is well known that physical activity promotes bone formation and that bone architecture adapts to loading. Schwarz et al. (2006) gave an overview of observations of the effect of different physical activities on humans and animals. The strain distribution during locomotion is complex (Coleman et al., 2002). Different animal models where loading can be controlled have been used to study these effects as for example by the isolated avian-bone model, used for roosters and turkeys (Rubin and Lanyon , 1984; Lanyon and Rubin , 1984), as well as the rat model (Mosley and Lanyon , 1998). When developing numerical models of bone adaptation, the strain energy density (Huiskes et al., 2000) is often regarded as driving the process. The strain energy density is caused by e.g. muscle loading (Be'ery-Lipperman and Gefen , 2005). In these studies, a cellular communication network with osteocytes as mechanosensors is incorporated.

In this investigation, it is assumed that the primary condition leading to bone growth is a change of the chemical environment caused by transport of matter resulting from stress driven diffusion. The change in the chemical environment may consist of changes in the concentration of different substances stimulating, for example, osteoblast recruitment or suppression of osteoclast activity. Experimental evidence that mechanical loading stimulates lining cells at the periosteum to differentiate into osteoblasts has been reported by Pead et al. (1988) and Boppart et al. (1998). In Cardoso et al. (2013), a review was presented on the porosity and permeability of bone, as well as the interstitial fluid flow through interconnected canals in the bone (e.g. Haversian canals, Volkmann canals or the lacunar-canalicular system). In the present study, the bone is treated as a homogenous material and the interstitial flow, which on the smaller scale was described as flow in canals, is here described as diffusion. As a result of this diffusion, matter that changes the chemical prerequisites for bone remodeling is transported.

Banks-Sills et al. (2011) presented a one-dimensional model based on the hypothesis that the primary condition leading to bone growth is a change of the chemical environment caused by stress driven diffusion. An oscillating bending moment was applied which produced a stress gradient over the cross-section of the bone. The flux J and concentration c of the growth promoting substances were assumed to be governed by Fickian diffusion generalized to include a stress gradient term. In the present study, a two-dimensional finite element (FE) model is established. A steady state solution is sought. Comparisons are made to the one-dimensional analytic results. In addition, the two-dimensional model allows for a more realistic comparison between numerically obtained results and

experiments found in the literature.

The analysis focuses on the concentration distribution over the bone cross-section and the seepage of nutrients into the cambium layer of the periosteum for different loading frequencies. Comparison with experiments shows that the maximum bone growth appears in the regions where the highest concentration occurs, rather than high stress.

In Section 2, the mathematical two-dimensional model describing the behavior of the concentration is presented. Since the applied loading is sinusoidal, the expected solution should be a combination of sines and cosines with the same frequency. With this assumption in Section 3, the two components of the solution and boundary conditions are decoupled. It is shown that there is an analogy between these governing equations and boundary conditions and those for a plate on an elastic foundation. In this way, the finite element method (ABAQUS , 2009) may be utilized to solve for these unknowns. The analogy is developed in Appendix A. In Section 4, results are presented. Comparison is made between bone growth observed by Lanyon and Rubin (1984) and the regions where the concentration of bone growth substances are predicted to be the highest by a finite element analysis.

2 Model

In this investigation, the transport of matter in a cross-section of a mammal's long bone is studied. The bone is assumed to be loaded in bending which produces a strain in the direction perpendicular to the cross-section. In addition to the gradient of a concentration field c, the gradient of the hydrostatic stress σ_h, caused by bending, is assumed to provide a driving force resulting in the transport of matter in the plane of the cross-section. This latter contribution controls the diffusion process. The concentration is assumed to deviate only slightly from a constant concentration c_o. For more details regarding the implications of this assumption see Banks-Sills et al. (2011). The applied load is based on the *in vivo* experiments of Lanyon and Rubin (1984). Avian ulnas were strained in and exposed to oscillating compression of 1 Hz for 100 cycles a day during eight weeks. As a result of the curvature of the bone, a bending moment is produced. The neutral axis shown in Figure 1 as $N-N$ is defined to coincide with the x-axis. This is the axis for which the strain ε_{zz} is zero. The moment only produces bending about this axis.

The flux vector $\boldsymbol{J}$ of a selected substance in the bone environment becomes (Li , 1978)

$$\boldsymbol{J}(x,y,t) = -D\boldsymbol{\nabla}c(x,y,t) + BV_A c_o \boldsymbol{\nabla}\sigma_h(x,y,t)\,, \tag{1}$$

where $\boldsymbol{\nabla}$ is the gradient operator in Cartesian coordinates given in two dimensions by

$$\boldsymbol{\nabla} = \left(\frac{\partial}{\partial x}, \frac{\partial}{\partial y}\right)\,. \tag{2}$$

In eq. (1), D is the diffusion coefficient of the substance-bone system, B is the mechanical mobility, V_A is the atomic volume of the bone nutrients and c_o is the initial concentration. As in Banks-Sills et al. (2011), as a first approximation, it has been assumed that $c \approx c_o$.

Matter is assumed to be conserved and, therefore, the divergence of the flux $\boldsymbol{J}$ is related to the concentration by

$$\boldsymbol{\nabla}\cdot\boldsymbol{J}(x,y,t) = -\dot{c}(x,y,t)\,, \tag{3}$$

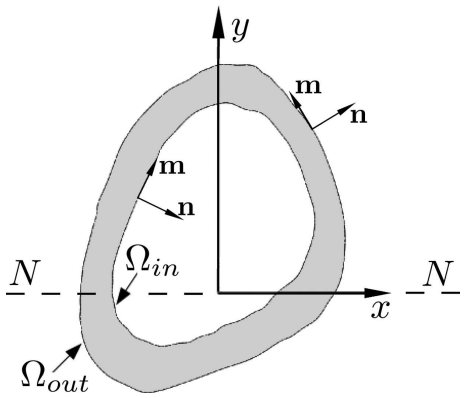

Figure 1: The cross-section of the right intact turkey ulna from Lanyon and Rubin (1984).

where the dot over a quantity indicates its derivative with respect to time and the dot between vectors represents the scalar product. If the flux $\boldsymbol{J}$ is eliminated by combining eqs. (1) and (3), the governing equation becomes

$$\dot{c}(x,y,t) = \boldsymbol{\nabla} \cdot [D\boldsymbol{\nabla} c(x,y,t)] - V_A c_o \boldsymbol{\nabla} \cdot [B\boldsymbol{\nabla}\sigma_h(x,y,t)] \,. \tag{4}$$

The cross-section of the bone is shown in Figure 1. It is from the right ulna of a turkey and was taken from Figure 4a of Lanyon and Rubin (1984). A coordinate system is introduced with the z-axis along the axis of the long bone and the cross-section of the bone within the x-y plane. As explained earlier, bending occurs around the x-axis which coincides with the neutral axis $N - N$ of the cross-section (see Figure 1). The neutral axis was found from experimental results in Figure 3a of Lanyon and Rubin (1984). In addition, two unit vectors are defined on Ω_{out} and Ω_{in}; they are the outward normal vector $\boldsymbol{n}$ and the tangent vector $\boldsymbol{m}$ as shown in Figure 1. The material is assumed to be linear elastic with a modulus of elasticity E. The stress in the z-direction is given by

$$\sigma_z = \kappa E y \tag{5}$$

where κ is the curvature due to the bending about the x-axis. The concentration c contributes to the bending stress. It was seen in Banks-Sills et al. (2011) that its contribution to the solution is negligible. Hence, it is neglected in this study.

The chemical and mechanical state is assumed to vary insignificantly along the z-axis. In addition, apart from σ_z, all other components of the stress tensor vanish. The stress distribution over the cross-section is in equilibrium with a remote moment. In general, this moment is not parallel to the axis of zero strain, i.e., the neutral axis, denoted by $N - N$ in Figure 1. The component along the x-axis is denoted as M. This moment is given by

$$M = \kappa E I \,, \tag{6}$$

where I is the second moment of area of the cross-section about the x-axis. The moment about the y-axis does not contribute to the bending stress (Parnes , 2001, p. 499).

Using eqs. (5) and (6), one obtains the hydrostatic stress as

$$\sigma_h = \frac{1}{3}\sigma_z = \frac{My}{3I} \tag{7}$$

The moment is assumed to be oscillating in time with an angular velocity, ω, according to

$$M = M_o \sin \omega t \, . \tag{8}$$

It may be noted that a different oscillatory function was assumed in Banks-Sills et al. (2011) where the transient behavior of the concentration was also sought. The choice here does not affect the steady state solution. Substitution of eqs. (7) and (8) into eq. (1) leads to the components of the flux vector $\boldsymbol{J}$ as

$$\begin{aligned} J_x(x,y,t) &= -D\frac{\partial c(x,y,t)}{\partial x} \, , \\ J_y(x,y,t) &= -D\frac{\partial c(x,y,t)}{\partial y} + BV_A c_o \frac{M_o}{3I} \sin \omega t \, . \end{aligned} \tag{9}$$

In addition, assuming that the diffusion coefficient D and the mechanical mobility B are constants, together with insertion of eqs. (7) and (8) into eq. (4) results in the governing differential equation for the concentration as

$$\dot{c}(x,y,t) = D\nabla^2 c(x,y,t) \, . \tag{10}$$

In the present study, a particular geometry was selected. This is a cross-section of a turkey ulna that was examined experimentally *in vivo* and *post mortem* by Lanyon and Rubin (1984). The considered geometry is the bone cross-section shown in Figure 1. The studied substance is continuously supplied to the medullary cavity, that is within Ω_{in} in Figure 1, so that the concentration within this region is not affected by the amount that diffuses into the bone. At the outer surface of the bone, Ω_{out}, the outer layer of the periosteal membrane is assumed to be a nearly impermeable layer. Thus, the flux out of the periosteal layer has an insignificant effect of the concentration distribution.

The boundary conditions consist of a constant concentration c_o along the boundary Ω_{in} at the medullary cavity, and a vanishing flux over the outer boundary Ω_{out}. These conditions may be written as

$$c(x,y,t) = c_o \qquad \text{for } (x,y) \, \epsilon \, \Omega_{in} \tag{11}$$

and

$$\boldsymbol{n}(x,y) \cdot \boldsymbol{J}(x,y,t) = 0 \qquad \text{for } (x,y) \, \epsilon \, \Omega_{out} \, . \tag{12}$$

In eq. (12)

$$\boldsymbol{n}(x,y) = n_x(x,y)\boldsymbol{e}_x + n_y(x,y)\boldsymbol{e}_y \tag{13}$$

is the outward unit normal to the boundary Ω_{out} and $\boldsymbol{e}_x$ and $\boldsymbol{e}_y$ are unit vectors in the x and y-directions, respectively. Substitution of eqs. (9) into eq. (12) leads to

$$\boldsymbol{n} \cdot \boldsymbol{\nabla} c(x,y,t) = \frac{\partial c(x,y,t)}{\partial n} = n_y \frac{BV_A c_o}{D} \frac{M_o}{3I} \sin \omega t \quad \text{for } (x,y) \, \epsilon \, \Omega_{out} \, , \tag{14}$$

where n is a coordinate along the direction of $\boldsymbol{n}$. To simplify the analysis, dimensionless variables are introduced for the flux vector and concentration given by

$$\hat{\boldsymbol{J}} = \frac{3I}{BV_A c_o M_o} \boldsymbol{J} \qquad \hat{c} = \frac{3ID}{BV_A M_o a} \frac{c - c_o}{c_o} \tag{15}$$

where a is a measure of the width of the bone obtained as the average at four locations (two along the x-axis and two along the y-axis as in Figure 1); it was found to be 1.8 mm. In addition, the time, space coordinates and the frequency are normalized as

$$\hat{t} = \frac{D}{a^2}t \qquad \hat{x} = \frac{x}{a} \qquad \hat{y} = \frac{y}{a} \qquad \hat{n} = \frac{n}{a} \qquad \hat{m} = \frac{m}{a} \qquad \hat{\omega} = \frac{a^2}{D}\omega \ . \tag{16}$$

Note that n and m represent a local coordinate system normal and tangent to Ω_{out} and Ω_{in} as shown in Figure 1.

Equation (10) may now be written as

$$\dot{\hat{c}}(\hat{x}, \hat{y}, \hat{t}) = \hat{\nabla}^2 \hat{c}(\hat{x}, \hat{y}, \hat{t}) \tag{17}$$

where the $\dot{(\ )}$ now represents differentiation with respect to the dimensionless time $\hat{t}$ and the hat above ∇ indicates differentiation with respect to the normalized spacial coordinates $\hat{x}$ and $\hat{y}$. In addition, the boundary conditions in eqs. (11) and (14) may be normalized as

$$\hat{c}(\hat{x}, \hat{y}, \hat{t}) = 0 \qquad \text{for } (\hat{x}, \hat{y}) \, \epsilon \, \Omega_{in} \tag{18}$$

and

$$\frac{\partial \hat{c}(\hat{x}, \hat{y}, \hat{t})}{\partial \hat{n}} = n_y \sin \hat{\omega}\hat{t} \qquad \text{for } (\hat{x}, \hat{y}) \, \epsilon \, \Omega_{out} \ . \tag{19}$$

The transient problem is governed by eqs. (17) through (19) with the initial condition

$$\hat{c}(\hat{x}, \hat{y}, 0) = 0 \ . \tag{20}$$

Since in the present study, the bone is assumed to be subjected to cyclic loading for an extended period (i.e. $\hat{t} \gg 1$), the steady state solution is sought. The analytical solution for a rectangular bone cross-section found in Banks-Sills et al. (2011) reveals that after a time $1.9t_o$, where $t_o = a^2/D$, the concentration decreased to about one-hundredth of its initial value with an exponential decay. Hence, the steady state solution should be valid for t somewhat greater than about $3t_o$. Limiting the study to steady state reduces the number of variables and eliminates the time dependence as is explained in the next section.

3 Analysis

Since the boundary condition in eq. (19) is sinusoidal, the solution to the partial differential equation in eq. (17) will approach a pure oscillatory state for long time. It may be written in the form

$$\hat{c}(\hat{x}, \hat{y}, \hat{t}) = \hat{c}_1(\hat{x}, \hat{y}) \sin \hat{\omega}\hat{t} + \hat{c}_2(\hat{x}, \hat{y}) \cos \hat{\omega}\hat{t} \tag{21}$$

so that there is a separation of the solution in time and space. Substitution of eq. (21) into eq. (17) leads to

$$\hat{\omega}\hat{c}_1(\hat{x}, \hat{y}) = \hat{\nabla}^2 \hat{c}_2(\hat{x}, \hat{y}) \ , \tag{22}$$

and

$$\hat{\omega}\hat{c}_2(\hat{x}, \hat{y}) = -\hat{\nabla}^2 \hat{c}_1(\hat{x}, \hat{y}) \tag{23}$$

where the sine and cosine terms are independent. Equations (22) and (23) may be decoupled as

$$\hat{\nabla}^4 \hat{c}_i(\hat{x},\hat{y}) + \hat{\omega}^2 \hat{c}_i(\hat{x},\hat{y}) = 0 \tag{24}$$

where $i = 1, 2$. In addition, the solution, eq. (21) may be rewritten as

$$\hat{c}(\hat{x},\hat{y},\hat{t}) = \tilde{c}(\hat{x},\hat{y}) \sin(\hat{\omega}\hat{t} + \varphi) \tag{25}$$

where

$$\tilde{c}(\hat{x},\hat{y}) = \sqrt{\hat{c}_1^2(\hat{x},\hat{y}) + \hat{c}_2^2(\hat{x},\hat{y})} \tag{26}$$

and

$$\varphi(\hat{x},\hat{y}) = \tan^{-1}\left[\frac{\hat{c}_2(\hat{x},\hat{y})}{\hat{c}_1(\hat{x},\hat{y})}\right] . \tag{27}$$

In order to solve eq. (24), four boundary conditions for each function are required.

To this end, by substituting eq. (21) into eq. (18), the boundary condition at the inner boundary of the bone Ω_{in} (see Figure 1) becomes

$$\hat{c}_1(\hat{x},\hat{y}) = \hat{c}_2(\hat{x},\hat{y}) = 0 \qquad \text{for } (\hat{x},\hat{y}) \in \Omega_{in} . \tag{28}$$

As a result of eq. (28), all gradients of $\hat{c}_1$ and $\hat{c}_2$ with respect to $\hat{m}$ along the inner boundary Ω_{in} vanish. Recall that $\hat{m}$ is the normalized coordinate along the tangent of the boundary. When the direction of $\hat{m}$ is followed the body is to the left. Further, from the boundary condition in eq. (18), it follows that the time derivative of the concentration on the inner boundary vanishes. Thus, from eq. (17), one obtains

$$\frac{\partial^2 \hat{c}_1(\hat{x},\hat{y})}{\partial \hat{n}^2} = \frac{\partial^2 \hat{c}_2(\hat{x},\hat{y})}{\partial \hat{n}^2} = 0 \qquad \text{for } (\hat{x},\hat{y}) \in \Omega_{in} . \tag{29}$$

Substitution of eq. (21) into eq. (19), at the outer boundary, Ω_{out}, leads to

$$\frac{\partial \hat{c}_1(\hat{x},\hat{y})}{\partial \hat{n}} = n_y \;\text{ and }\; \frac{\partial \hat{c}_2(\hat{x},\hat{y})}{\partial \hat{n}} = 0 \qquad \text{for } (\hat{x},\hat{y}) \in \Omega_{out} . \tag{30}$$

The fourth set of boundary conditions is obtained by differentiating eqs. (22) and (23) with respect to $\hat{n}$ and inserting eq. (30) into the result to obtain

$$\left.\begin{aligned} \frac{\partial}{\partial \hat{n}}\left[\hat{\nabla}^2 \hat{c}_1(\hat{x},\hat{y})\right] &= \frac{\partial}{\partial \hat{n}}\left[-\hat{\omega}\hat{c}_2(\hat{x},\hat{y})\right] = 0 \\ \frac{\partial}{\partial \hat{n}}\left[\hat{\nabla}^2 \hat{c}_2(\hat{x},\hat{y})\right] &= \frac{\partial}{\partial \hat{n}}\left[\hat{\omega}\hat{c}_1(\hat{x},\hat{y})\right] = \hat{\omega} n_y \end{aligned}\right\} \text{ for } \quad (\hat{x},\hat{y}) \in \Omega_{out} . \tag{31}$$

In summary, as a result of the complicated geometry of the bone cross-section, a numerical solution is required. Assumption of a time harmonic solution led to a differential equation in space, namely eq. (24). This avoids solution of the time dependent differential equation in (17) with the time dependent boundary condition in eq. (19).

The governing equations in eq. (24) together with the boundary conditions in eqs. (28) through (31) are solved using a finite element formulation. The system is analogous to the differential equation for a plate supported by an elastic foundation with corresponding boundary conditions (see Appendix A). Hence, the numerical analyses may be conveniently performed using a commercial finite element code for structural analysis. In this study, the software ABAQUS (2009) was used. For more details on the FE formulation of a plate, see, for example, Zienkiewicz (1977).

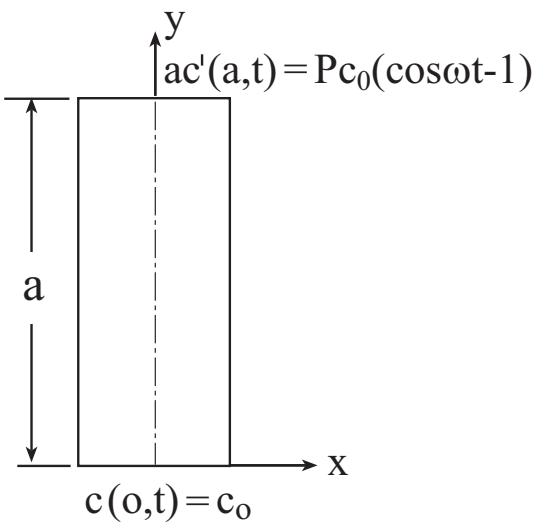

Figure 2: Half the rectangular bone cross-section with boundary conditions.

4 Results

The analogy of a plate on an elastic foundation is used to solve for the distribution of the amplitude, $\tilde{c}$, of the concentration according to eq. (26) in the bone. In Section 4.1, the numerical method is validated by comparison to a one-dimensional analytical solution (Banks-Sills et al., 2011). In Section 4.2, results from the two-dimensional finite element analyses are described.

4.1 Validation of the numerical method using a one-dimensional model

To validate the numerical model, a rectangular cross-section of the bone which does not include the medullary cavity (see Figure 2) is considered first, for which an analytical solution is known (see Banks-Sills et al., 2011). In that case, a second order partial differential equation in space and time given in eq. (43) was solved with the two boundary conditions in eqs. (44) applied at $y = 0$ and $y = a$, respectively, and the initial condition given in eq. (45). The flux across the two remaining sides is assumed to vanish. Thus, the flux across the bone becomes one-dimensional and the problem depends only on one coordinate, namely y. An exact transient solution for this case was obtained by Banks-Sills et al. (2011). The model is described in detail in Appendix B. Although the problem is one-dimensional, in the analogy, the assumption is made of a plate in the xy-plane on an elastic foundation. The behavior in the x-direction is assumed to be uniform.

In the numerical calculations, a mesh consisting of 19,840 three noded plate elements was used. There were approximately 200 elements along the y-axis for the plate in Figure 2. The free mesh was generated with an irregular structure. The solution was obtained by means of a general purpose finite element code ABAQUS (2009) using the fully analogous case of an elastic plate on a flexible foundation. The differential equation is given in eq. (51) and the boundary conditions in eqs. (52) through (55). The variables

Table 1: Finite element ($\tilde{c}_{FE}$) and analytical ($\tilde{c}_A$) results, as well as the relative errors in eq. (33) for different normalized loading frequencies $\hat{\omega}$.

$\hat{\omega}$	$\tilde{c}_{FE}$	$\tilde{c}_A(a)$	err (%)
0	1.0000000	1	0.
0.004	0.9999988	0.9999988	0.
0.04	0.9998756	0.9998756	0.
0.4	0.9878000	0.9877996	$O(10^{-5})$
4	0.5595646	0.5595604	$O(10^{-4})$
40	0.1581535	0.1581505	0.0019
400	$5.0006275 \cdot 10^{-2}$	$5.0000000 \cdot 10^{-2}$	0.0126
4000	$1.5812206 \cdot 10^{-2}$	$1.5811389 \cdot 10^{-2}$	0.0052
40000	$4.9113973 \cdot 10^{-3}$	$5.0000000 \cdot 10^{-3}$	1.8
400000	$0.8878488 \cdot 10^{-3}$	$1.5811389 \cdot 10^{-3}$	44
4000000	$0.9467252 \cdot 10^{-4}$	$5.0000000 \cdot 10^{-4}$	81

$\hat{c}_i$ (concentration) should be thought of as the deflection of the plate. The three noded elements make use of a linear shape function for the displacement.

In carrying out the finite element analysis, the elements are required to be sufficiently small in order to capture the details of the solution. An upper limit to the element size above which the analysis fails is related to the wavelength of the solution. The higher the frequency ω, the smaller the wavelength, so that smaller elements are needed. To understand this, consider the behavior of eqs. (15) through (21) of Banks-Sills et al. (2011) for high frequency i.e. for large values of ηy. It may be observed in eqs. (15) to (21) of Banks-Sills et al. (2011) that for large values of ηy, $\sinh(\eta y) \approx \exp(\eta y)/2$ and $\cosh(\eta y) \approx \exp(\eta y)/2$. This implies that the steady state part of $c(y,t)$ oscillates with a half period of $y_p = \pi/\eta$. The length y_p is a characteristic length of the solution for $c(y,t)$ and therefore an upper limit of the element size ℓ would be

$$\ell \ll y_p = \frac{\pi}{\eta} = \pi a \sqrt{\frac{2}{\hat{\omega}}} \,. \tag{32}$$

The number of elements along the y-axis used in the present solution is 200 meaning that an upper limit of the frequency that will provide an accurate solution is $\ell = \frac{a}{200} \ll \pi a \sqrt{\frac{2}{\hat{\omega}}} \Rightarrow \hat{\omega} \ll 2\pi^2\, 200^2 \approx 8 \cdot 10^5$.

The finite element result $\tilde{c}_{FE}$ is the amplitude of $\hat{c}$ given in eq. (56). The corresponding analytical result, denoted by $\tilde{c}_A$, is the amplitude of the solution and given in eq. (57). The solution $\tilde{c}_A$ is exact; whereas, $\tilde{c}_{FE}$ is a numerical result. The relative percent error is defined by

$$\text{err} = \frac{|\tilde{c}_A - \tilde{c}_{FE}|}{\tilde{c}_A} \times 100\% \,. \tag{33}$$

It is now possible to estimate the error for different frequencies. Values of the exact and numerically calculated concentrations $\tilde{c}_A$ and $\tilde{c}_{FE}$, respectively, at the upper boundary of the bone, namely, $\hat{y} = 1$ are presented in Table 1 for various values of the normalized

frequency $\hat{\omega}$ given in eq. $(16)_6$. The result shows an error that is extremely small, and in some cases zero (to the number of significant figures shown), for small values of the frequency. Recall that the finite element analysis is carried out for a plate on an elastic foundation where in this case, the stiffness of the foundation vanishes; see eqs. (51) and $(40)_4$. It may be noticed in Table 1 that for $\hat{\omega} < 0.4$, the finite element and exact solutions are in complete agreement to many significant figures. As $\hat{\omega} \to 0$, the trivial, rigid body, linear solution in eq. (50) is satisfied by any finite element. Furthermore, the error is within reasonable limits as long as $\hat{\omega} \leq 10^4$; for $\hat{\omega} = 10^4$, the error is less than 2%. It is interesting to note that according to the restrictions on the element size ℓ in eq. (32), approximately nine elements are equivalent to half the wavelength for this frequency along the y-axis (there are 200 elements along the y-axis). One may also observe that the error increases quite dramatically for higher frequencies (see Table 1). In contrast to the one-dimensional model, the two-dimensional model leads to a non-linear distribution of the concentration at vanishing frequencies $\hat{\omega}$ as shown in Section 4.2. The implication is that the error as predicted for the one-dimensional case is likely to underestimate the error occurring in the two-dimensional analyses for low frequencies.

4.2 The two-dimensional model

In this section, the two-dimensional model of the bone illustrated in Figure 1 is considered. The solution of the analogous plate on an elastic foundation is found by means of the finite element method as explained in Appendix A. Recall that the differential equation for the normalized concentration $\hat{c}_i$ is given in eq. (24). The normalized amplitude of the concentration $\tilde{c}$ in eq. (26) is presented in Figure 3 for different normalized frequencies $\hat{\omega}$. These results were obtained with a mesh of 3,780 three noded plate elements and 2,090 nodal points. There were 15 to 19 elements across the bone wall.

The limiting quasi-static case ($\hat{\omega} \ll 1$ and $\hat{t} \gg 1$) is shown in Figure 3a. This case is obtained by replacing the governing equation (17) with $\hat{\nabla}^2 \hat{c} = 0$. Writing $\hat{c}$ as in eq. (21), results in $\hat{c} = \hat{c}_1 \sin \hat{\omega} \hat{t}$. If one considers the boundary conditions in eqs. (28) through (31) for $\hat{c}_2$, noting that $\hat{\omega} \ll 1$, it becomes clear that $\hat{c}_2$ vanishes everywhere. For low frequencies, the concentration becomes large in both the one-dimensional and two-dimensional models. Unlike the result for the one-dimensional model, where the concentration, $\tilde{c}_A$ is proportional to $\hat{y}$ (consider eq. (57) for small values of η), the result in the two-dimensional model is a non-uniform distribution over the bone cross-section. The difference is essential and influences the concentration at the outer regions of the bone at low frequencies.

The results for moderate frequencies with $\hat{\omega}$ being 1 or 2, displayed in Figures 3b and 3c, show that the concentration also becomes large over extended regions of the bone cross-section. Close to the medullary cavity, as well as in two locations (deep blue color) near the lower part of the cross-section, the concentration vanishes. It follows from eq. (5), that the uni-axial stress which acts on the cross-section is proportional to the y-coordinate (see Figure 1) and is zero at the neutral axis (N-N) as may be seen in Figure 4a. It is noted from eq. (5), that as anticipated, the bending stress is linear in y as may be seen by the parallel colors in Figure 4a. Note that the amplitude of the bending stress is plotted. Clearly, the regions close to periosteal surface with high concentration, do not fully correlate with those of high stress. For higher frequencies, such as $\hat{\omega} = 10$,

the most striking effects are, first, that the concentration amplitude decays and, second, that there is a skin effect in the sense that elevated concentrations only develop close to

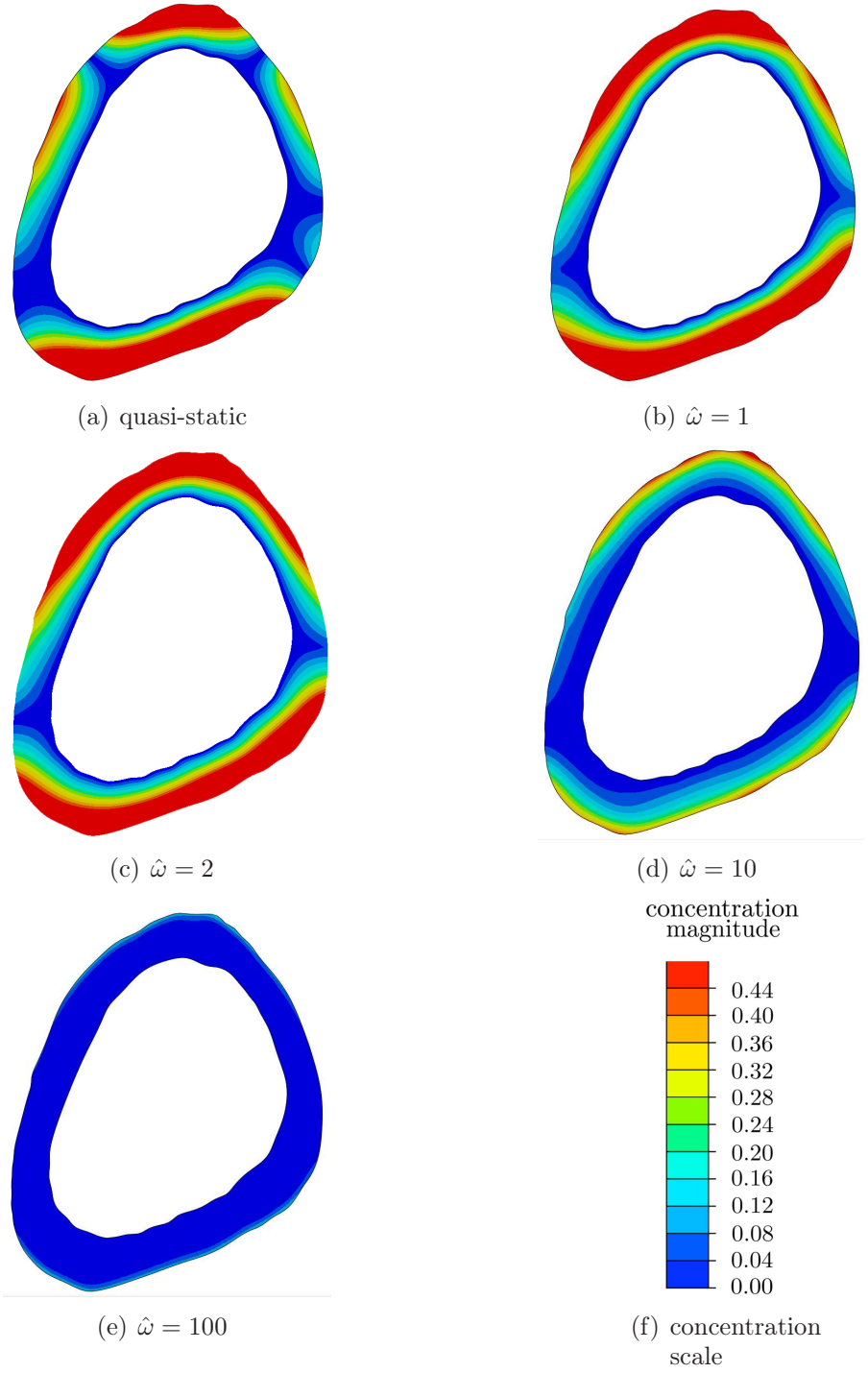

(a) quasi-static (b) $\hat{\omega} = 1$ (c) $\hat{\omega} = 2$ (d) $\hat{\omega} = 10$ (e) $\hat{\omega} = 100$ (f) concentration scale

Figure 3: Normalized concentration amplitude $\tilde{c}$ in eq. (26) distributed over the bone cross-section for different non-dimensional load frequencies $\hat{\omega} = \omega a^2/D$.

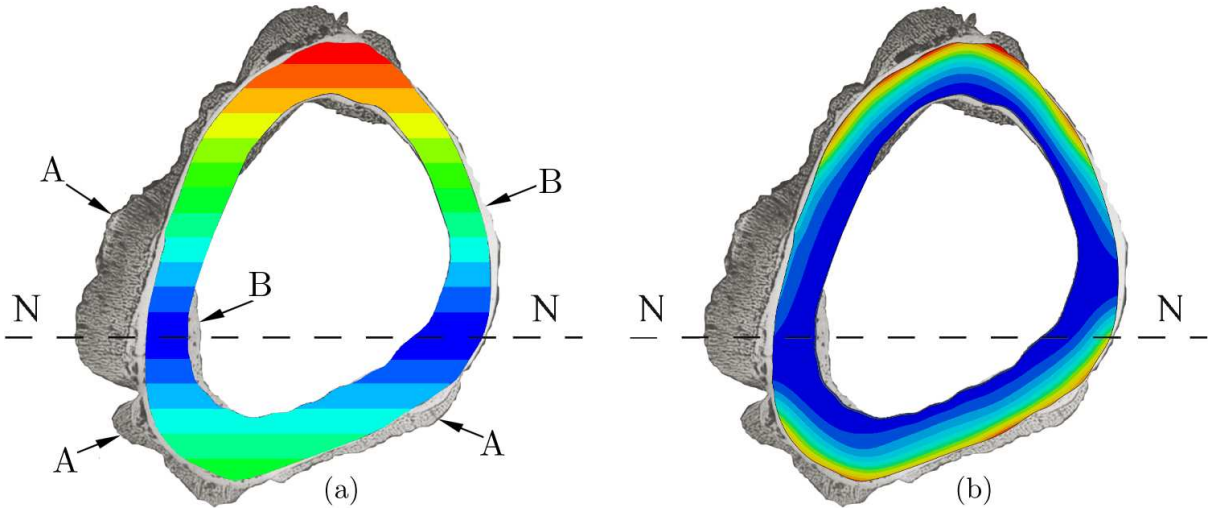

Figure 4: Results on the bone cross-section: (a) amplitude of the bending stress and (b) amplitude of the normalized concentration $\tilde{c}$. A denotes newly formed bone and B denotes original bone.

the periosteal surface (see Figure 3d). For the highest frequency used in the calculations $\hat{\omega} = 100$, according to Figure 3e, the concentration seemingly vanishes everywhere.

It may be noted that a mesh containing 25,312 three noded plate elements with 12,956 nodal points was used to calculate the deflections of the plate for normalized frequencies of $\hat{\omega} = 2$ and $\hat{\omega} = 10$. There were between 32 and 52 elements across the bone. A sampling of a few points showed differences between results obtained with the fine mesh and the coarse mesh to be less than 1% for $\hat{\omega} = 2$ and less than 2% for $\hat{\omega} = 10$.

A thin membrane called the periosteal surface, or the periosteum, covers the outer bone surface. It consists of two layers: an outer fibrous layer and an inner cambium layer consisting of osteoprogenitor cells, i.e. undifferentiated bone cells capable of differentiating into osteoblasts. The outer layer acts as connective tissue to its surroundings, such as muscles. Since the osteoprogenitor cells in the cambium layer can differentiate into osteoblasts, they may initiate bone growth when stimulated (Owen, 1978).

It is assumed here that the chemical conditions at the bone surface are altered through the stress driven diffusion where transport into the cambium layer is initiated. The effectiveness of the process depends on the permeability of the cambium, as well as the outer layer of the periosteum. It is assumed that the cambium layer is permeable and the outer layer of the periosteum is impermeable. The thickness of the cambium layer is very small compared to the diameter of the bone so that the concentration at Ω_{out} is taken to be the same in the cambium layer. The flux mechanisms are assumed to be similar to those of bone, namely, the transport is supposed to occur by means of stress driven diffusion. So that it is assumed that in regions of high concentration, bone growth will occur.

The results obtained using the two-dimensional model can be compared with the classical experimental observations made by Lanyon and Rubin (1984) on turkey ulnae. In the present investigation, the cross-section of the right ulna considered in that study

was analyzed and is illustrated in Figure 1. The birds were exposed to cyclic compression with a frequency of 1 Hz. The average value of the bone width is $a = 1.8$ mm; the tissue level diffusion coefficient D was taken from Patel et al. (2005) as 1.57×10^{-6} m^2/s. This leads to a value of the normalized frequency of $\hat{\omega} \approx 13$, where the natural curvature of the ulnae caused the bone to bend. In Figure 4a, the bending stress distribution is combined with Figure 4b of Lanyon and Rubin (1984) showing the regions of bone growth. It should be noted, that the actual ulna underlying the numerical results shown in Figure 4 is the left turkey ulna. There is a slight difference in the original width of the cortical bone with the left bone being somewhat bigger than the right bone. The original bone is marked in the figure with a B and the bone growth with an A. The differences in gray scale of the bone are distinct with new bone being a deeper shade. The concentration distribution in Figure 3d for $\hat{\omega} = 10$ is combined with their Figure 4b. As may be observed, the bone growth is rather diffuse and does not necessarily occur at the parts of the cross-section that are the farthest from the neutral axis where the stress reaches its maximum (see Figure 4a). Instead growth is spread out around the bone not very unlike the distribution of high concentration of Figure 4b. Further, the absence of bone growth does not necessarily coincide with the neutral axis.

5 Conclusions

Diffusion driven by hydrostatic stress is examined in a cross-section of a long bone. The analysis is two-dimensional and provides an opportunity to study the distribution of growth promoting substances over the cross-section. The analysis is limited to a steady state result with the concentration required not to differ too much from its ambient value. A technique of separating the two phases of the solution into coupled static solutions is used to remove the time dependence of the variables. One part of the solution is in-phase with the applied load, whereas, the other part is out-of-phase. These unknown concentrations are found by means of an analogy with the problem of a plate on an elastic foundation. Using this analogy, the finite element method is used to solve the plate problem.

It is found that at very low frequencies, the variation of the concentration is in-phase with the applied load. It is observed to decay with increasing frequency. It is assumed that the concentration of the bone nutrients leaks into the cambium layer of the periosteum where osteoblasts are excited to create new bone. Comparison is made to experimental results for a turkey ulna (Lanyon and Rubin , 1984). There is an interesting correlation between the experimental results for bone growth and regions of high concentration. The simulations indicate that there is a thin layer close to the periosteum with high concentration. As compared to the stress distribution (see Figure 4a), the concentration is more evenly distributed along the periosteum so that the nutrients are focused in this region. It may be observed in Figures. 3b and 3c that the behavior is the same also at lower frequencies. The predicted growth seems reasonably correlated apart from a segment on the left side of the cross-section in Figure 4b where the growth rate is many times larger than the average. The reason for this is not known. One has to keep in mind that only one experimental observation of a single animal was considered; hence, variations may be expected. Indeed, simulations using the diffusion concept should be

compared with other experimental findings. The simulations of the diffusion process could also be combined with a bone adaptation model where the geometry of the bone cross-section is updated while the bone is loaded. In that case, two time-scales should be considered: over short time, the loading frequency would drive the diffusion process; for longer times, the changes in the bone cross-section would be observed.

It might be worthwhile in the future to reconsider the more accurate eq. (4) when $c_o = c$ to assess the effect of higher concentration values. In addition, more accurate values of the diffusivity constant D and the mechanical mobility B would be worth pursuing.

A Analogy with a plate on an elastic foundation

The analogy between the present problem and a problem for an elastically supported plate is presented in this appendix. The concentration variables $\hat{c}_1$ and $\hat{c}_2$ are governed by eq. (24), which may be written as

$$\nabla^4 \hat{c}_i + \hat{\omega}^2 \hat{c}_i = 0 \,, \tag{34}$$

where $i = 1, 2$. The boundary conditions, eqs. (28) to (31), are rewritten as

$$\begin{aligned}
&\hat{c}_i(\hat{x}, \hat{y}) = 0 && \text{for} \quad (\hat{x}, \hat{y}) \in \Omega_{in} \\
&\frac{\partial^2 \hat{c}_i(\hat{x}, \hat{y})}{\partial \hat{n}^2} = 0 && \text{for} \quad (\hat{x}, \hat{y}) \in \Omega_{in} \\
&\frac{\partial \hat{c}_i(\hat{x}, \hat{y})}{\partial \hat{n}} = f_i && \text{for} \quad (\hat{x}, \hat{y}) \in \Omega_{out} \\
&\frac{\partial}{\partial \hat{n}} \left[\hat{\nabla}^2 \hat{c}_i(\hat{x}, \hat{y}) \right] = g_i && \text{for} \quad (\hat{x}, \hat{y}) \in \Omega_{out} \,,
\end{aligned} \tag{35}$$

where f_i and g_i are prescribed values.

Consider now a plate in its original configuration situated in the x-y plane. Kirchoff's theory for thin plates provides the differential equation for determining the deflection of the plate when it is subjected to a load $p(x, y)$ applied in the z-direction, perpendicular to the plane of the plate. The theory omits effects of shearing on the deflection. The governing differential equation is given by

$$\tilde{D} \nabla^4 w(x, y) = p(x, y) \tag{36}$$

where the plate stiffness is

$$\tilde{D} = \frac{E h^3}{12(1 - \nu^2)} \,. \tag{37}$$

Here E is Young's modulus, h is the thickness of the plate and ν is Poisson's ratio. If the plate is supported by an elastic foundation the load p becomes proportional to the deflection of the plate. This implies that

$$p(x, y) = -k w(x, y) \,. \tag{38}$$

Here k is the stiffness of the foundation with dimensions of force F per unit volume L^3, i.e. F/L^3.

Assume that the plate has the shape of a ring as depicted in Figure 1. The plate is assumed to be simply supported at its inner edge, Ω_{in}; on its outer edge Ω_{out}, both the slope and shear force in the z-direction are prescribed. This leads to the following boundary conditions

$$\begin{aligned}
&w(x,y) = 0 && \text{for} \quad (x,y) \in \Omega_{in} \\
&\frac{\partial^2 w(x,y)}{\partial n^2} = 0 && \text{for} \quad (x,y) \in \Omega_{in} \\
&\frac{\partial w(x,y)}{\partial n} = -\frac{1}{\tilde{D}}\theta(x,y) && \text{for} \quad (x,y) \in \Omega_{out} \\
&\frac{\partial}{\partial n}\left[\nabla^2 w(x,y)\right] = -\frac{1}{\tilde{D}}V(x,y) && \text{for} \quad (x,y) \in \Omega_{out}\,,
\end{aligned} \tag{39}$$

where $\theta(x,y)$ is a given rotation around the outer edge of the ring and $V(x,y)$ is a given line shear load applied at the outer edge in the z-direction.

With the following replacements

$$x \to \hat{x} \qquad y \to \hat{y} \qquad n \to \hat{n} \qquad \frac{ka^4}{\tilde{D}} \to \hat{\omega}^2 \tag{40}$$

both cases may be treated. For the first case, namely $\hat{c}_1(\hat{x},\hat{y})$

$$w \to \hat{c}_1(\hat{x},\hat{y}) \qquad \theta \to -\tilde{D} n_y(\hat{x},\hat{y}) \qquad V \to 0\,; \tag{41}$$

and for the second case, namely $\hat{c}_2(\hat{x},\hat{y})$

$$w \to \hat{c}_2(\hat{x},\hat{y}) \qquad \theta \to 0 \qquad V \to -\tilde{D}\hat{\omega} n_y(\hat{x},\hat{y})\,. \tag{42}$$

Thus, the analogy to the governing equations for $\hat{c}_1$ and $\hat{c}_2$ and their corresponding boundary conditions is established.

It may be interesting to note that the only free variable, the frequency $\hat{\omega}$ of the load on the bone, appears as the analogous stiffness of the foundation for the elastic plate. Thus, obviously, increasing the stiffness of the foundation leads to a distribution of the displacements of the plate that become increasingly concentrated at the outer edge of the plate and in the limit of infinite stiffness, all displacements vanish. Thus, also the concentration of the diffusing substance, c, is assumed to concentrate at the edge of the plate as the frequency increases and ought to decrease everywhere with increasing frequency; in the limit of infinite frequency, it should vanish.

B One-dimensional problem

The numerical method is validated by comparing it to a one-dimensional problem which was solved analytically (see Banks-Sills et al., 2011). The cross-section of the bone is assumed to be rectangular without the medullary cavity; half the cross-section is shown in Figure 2 where $2a$ is the height of the cross-section so that $-a \le y \le a$. Antisymmetry was assumed so that only half the geometry is analyzed here.

The governing partial differential equation (10) becomes

$$\dot{c}(y,t) = Dc''(y,t) \tag{43}$$

where the dot $\dot{(\,)}$ represents differentiation with respect to t and the prime denotes differentiation with respect to the y-coordinate. Two boundary conditions and one initial condition are needed in order to solve eq. (43). The boundary conditions are given as

$$c(0,t) = c_o \qquad \text{and} \quad ac'(a,t) = Pc_o(\cos\omega t \ - 1) \ . \tag{44}$$

The boundary condition at $y = 0$ follows from eq. (11). That at $y = a$ is taken from eq. (12) of Banks-Sills et al. (2011) where P is a normalized driving force for the transported substance. It may be noted that the boundary condition in eq. $(44)_2$ is related to a cosine function, whereas the analogous boundary condition for the two-dimensional problem in eq. (19) is related to a sine function. Since in this study the steady state solution is of interest, the phase of the right hand side of eq. (19) is irrelevant. However, it may be noted that in Section 4.2, the amplitude of the wave is twice that in Banks-Sills et al. (2011). The boundary conditions of the problem are shown in Figure 2. The initial condition from eq. (20) is written here as

$$c(y,0) = c_o \ . \tag{45}$$

The exact transient solution of this problem is found in Banks-Sills et al. (2011), eqs. (15) through (21). It is readily observed that one part of the solution decays exponentially with time with a remaining non-decaying part that forms the steady state solution. The latter consists of a time independent term that is linear in y, and a sinusoidally varying part. In a more compact form, eqs. (15) through (21) of Banks-Sills et al. (2011) may be written as

$$\frac{c(y,t)}{c_o} = 1 + P\left\{\frac{1}{\eta a}\sqrt{\frac{\cosh(2\eta y) - \cos(2\eta y)}{2[\cosh(2\eta a) + \cos(2\eta a)]}}\cos(\omega t + \varphi_o) - \frac{y}{a}\right\} \tag{46}$$

where

$$\eta = \sqrt{\frac{\omega}{2D}} \tag{47}$$

and φ_o is a phase angle that is a function of y. In eq. (46), the exponentially decaying term in time has been neglected. The solution may be approximated as being steady state after a long time, related to a characteristic time scale of the problem, such as $t \gg a^2/D$.

As in eq. (21), the solution is separated into a sine and cosine term, so that

$$\hat{c}(\hat{y},\hat{t}) = \hat{c}_1(\hat{y})\sin\hat{\omega}\hat{t} + \hat{c}_2(\hat{y})\cos\hat{\omega}\hat{t} \ . \tag{48}$$

In eq. (48), some of the variables have been normalized as in eq. (16); note that in the one-dimensional case a represents half the length of the bone (see Figure 2). In addition, $\hat{c}$ is normalized here as

$$\hat{c} = \frac{1}{P}\frac{c - c_o}{c_o} + \frac{y}{a} \ . \tag{49}$$

It may be noted that any linear term such as

$$C_1 y + C_2 \,, \tag{50}$$

where C_1 and C_2 are constants, represents a trivial solution of eq. (43) and may be added without reducing the generality of the solution. The term y/a is added to adjust the boundary condition in eq. $(44)_2$ to the purely sinusoidal boundary condition used in this investigation in eq. (19).

As in the two-dimensional case, the functions $\hat{c}_1(\hat{y})$ and $\hat{c}_2(\hat{y})$ are independent and may be shown to be solutions of

$$\hat{c}_i^{iv}(\hat{y}) + \hat{\omega}^2 \hat{c}_i(\hat{y}) = 0 \tag{51}$$

where $i = 1, 2$. Equation (51) is the counterpart to eq. (24) in one dimension. The boundary conditions at the medular cavity, namely $\hat{y} = 0$, become

$$\hat{c}_1(0) = \hat{c}_2(0) = 0 \tag{52}$$

and

$$\hat{c}_1''(0) = \hat{c}_2''(0) = 0 \,. \tag{53}$$

Equation (52) follows from eq. $(44)_1$; whereas, eq. (53) may be obtained by writing the one-dimensional versions of eqs. (22) and (23). At the outer boundary, namely $\hat{y} = 1$

$$\hat{c}_1'(1) = 0 \quad \text{and} \quad \hat{c}_2'(1) = 1 \,. \tag{54}$$

Equation (54) is obtained from the boundary condition in eq. $(44)_2$, with the normalization in eq. (49) and use of eq. (48). The fourth boundary condition is

$$\hat{c}_1'''(1) = -\hat{\omega} \quad \text{and} \quad \hat{c}_2'''(1) = 0 \tag{55}$$

which is obtained by differentiating the one-dimensional form of eqs. (22) and (23) by $\hat{y}$ and making use of eq. (54).

The fourth order differential equations given by (51) are identical to the equation for a beam on an elastic foundation with a spring stiffness $\hat{\omega}^2$ per unit length. Here, there is an analogy between the governing equations for the concentration and that of the deflection of a beam. The boundary conditions at $\hat{y} = 0$ in eqs. (52) and (53) are those of a simply supported beam. For case 1, i.e. $\hat{c}_1$, eq. $(54)_1$ gives a vanishing rotation and eq. $(55)_1$, a prescribed transverse force at $\hat{y} = 1$. For case 2, eq. $(54)_2$ prescribes a rotation and eq. $(55)_2$ prescribes a vanishing transverse force.

To avoid confusion, it should be recalled that the bone is modeled in the two-dimensional case as a hollow beam with the z-direction (see Figure 1) being along the longitudinal axis. The development above is analogous to a beam on an elastic foundation. Here, the longitudinal direction is along the y-axis (see Figure 2). In order to analyze this latter problem in conjunction with the finite element method which was done for the original bone cross-section, the beam is assumed to be a plate on an elastic foundation in the xy-plane as in Figure 2. The behavior along the x-axis should be uniform. As a result, the yz-plane is in a state of plane deformation as opposed to plane stress which is the usual case for a thin beam. The implication is that the modulus of elasticity

E, would be replaced with $E/(1-\nu^2)$ in the corresponding solution for a beam. However, since only a relative error is sought here, this substitution does not affect the results.

Finally, in making a comparison between results obtained by means of the finite element analysis and the exact solution, the amplitude of each are compared. For the finite element result, $\tilde{c}_{FE}$ is the amplitude of $\hat{c}$ which according to eq. (48) is

$$\tilde{c}_{FE} = \sqrt{\hat{c}_1^2 + \hat{c}_2^2} \, . \tag{56}$$

The corresponding analytical result, denoted by $\tilde{c}_A$, is the amplitude of the solution in eq. (46) when scaled according to eq. (49), and is given by

$$\tilde{c}_A = \frac{1}{\eta a} \sqrt{\frac{\cosh(2\eta y) - \cos(2\eta y)}{2[\cosh(2\eta a) + \cos(2\eta a)]}} \, . \tag{57}$$

The solution $\tilde{c}_A$ is exact; whereas, $\tilde{c}_{FE}$ is a numerical result.

References

ABAQUS. 2009. Version 6.12. Charlès B., editor. 3DS Dassault Systemes, Vélizy-Villacoublay: France.

Banks-Sills L, Ståhle P, Svensson I, Eliaz N. 2011. Strain driven transport for bone modeling at the periosteal surface. Math Biosci 230(1):37–44.

Be'ery-Lipperman M, Gefen A. 2005. Contribution of muscular weakness to osteoporosis: Computational and animal models. Clin Biomech 20(9):984–97.

Boppart MD, Kimmel DB, Yee JA, Cullen DM. 1998. Time course of osteoblast appearance after in vivo mechanical loading. Bone 23(5):409–415.

Coleman JC, Hart RT, Owan I, Tankano Y, Burr DB. 2002. Characterization of dynamic three-dimensional strain fields in the canine radius. J Biomech 35(12):1677–1683.

Cardoso L, Fritton SP, Gailani G, Benalla M, Cowin SC. 2013. Advances in assessment of bone porosity, permeability and interstitial fluid flow. J Biomech 46(2):253–265.

Huiskes R, Ruimerman R, van Lenthe GH, Janssen, JD. 2000. Effects of mechanical forces on maintenance and adaptation of form in trabecular bone. Nature 405:704–706.

Lanyon LE, Rubin CT. 1984. Static vs dynamic loads as an influence on bone remodelling. J Biomech 17(12):897–905.

Li JC-M. 1978. Physical chemistry of some microstructural phenomena. Metall Mater Trans A 9(10):1353-1380.

Mosley JR, Lanyon LE. 1998. Strain rate as a controlling influence on adaptive modeling in response to dynamic loading of the ulna in growing male rats. Bone 23(4):313–318.

Owen M. 1978. Histogenesis of bone cells. Calcif Tiss Res 25(1):205–207.

Parnes R. 2001. Solid mechanics in engineering. Chichester, UK: John Wiley & Sons, Ltd.

Patel RB, O'Leary JM, Bhatt SJ, Vasanja A, Knothe Tate ML. 2005. Determining the permeability of cortical bone at multiple length scales using fluorescence recovery after photobleaching techniques. In: Proceedings of the 51st Annual Meeting of the Orthopaedic Research Society. Washington, D.C.

Pead MJ, Suswillo R, Skerry TM, Vedi S, Lanyon LE. 1988. Increased 3H-uridine levels in osteocytes following a single short period of dynamic bone loading *in vivo*. Calcif Tiss Int 43(2):92–96.

Rubin CT, Lanyon LE. 1984. Regulation of bone formation by applied dynamic loads. J Bone Jt Surg 66-A(3):397–402.

Schwarz P, Courteix D, Karlsson MK. 2006. Exercise and bone. Eur J Sport Sci 6(3):141–144.

Zienkiewicz OC. 1977. The finite element method. 3th ed. London, England: McGraw-Hill.

Paper B

Growth of a Long Bone Cross Section - A 2D Phase-Field Model

Gustav Lindberg and Per Ståhle

Submitted May 15, 2018
Revised manuscript submitted Oct 17, 2018

Growth of a Long Bone Cross Section - A 2D Phase-Field Model

Gustav Lindberg[a] and Per Sthåle[a]

[a]Division of Solid Mechanics, Lund University
SE-221 00 Lund, Sweden

Abstract

An approach to model the effect of exercise on the growth of mammal long bones is described. A Ginzburg-Landau partial differential equation system is utilised to study the change of size and shape of a cross-section caused by mechanically enhanced bone growth. The concept is based on a phase variable that keeps track of the material properties during the evolution of the bone. The relevant free energies are assumed to be elastic strain energy, concentration gradient energy and a double well chemical potential. The equation governing the evolution of the phase is derived from the total free energy and put on a non-dimensional form, which reduces all required information regarding load, material and cross-section size to one single parameter. The partial differential equation is solved numerically for the geometry of a cross-section using a finite element method. Bending in both moving and fixed directions is investigated regarding reshaping and growth rates. A critical non-zero load is found under which the bone is resorbed. The result for bending around a fixed axis can be compared with experiments made on turkeys. Three loading intervals are identified, I) low load giving resorption of bone on the external periosteum and the internal endosteum, II) intermediate load with growth at the periosteum and resorption at endosteum and III) large loads with growth at both periosteum and endosteum. In the latter case the extent of the medullary cavity decreases.

Keywords: *phase-field; bone growth; diffusion; stress enhanced; finite element method; chemical potential; Ginzburg-Landau*

1 Introduction

It is well known that bone, like most living tissue, has the ability to self-repair and can adapt its size and external shape, internal structure and mass density according to the mechanical environment and hormonal changes. The modelling and remodelling is a dynamic process that involves removal of old bone tissue, resorption and formation of new tissue. The process is dominated by the activity of bone cells such as osteoblasts, osteoclasts, osteocytes and bone lining cells (Cowin, 2001).

The cause of activation of these cells is widely discussed, and several hypotheses exist involving both direct and indirect activation of mechanical load. A number of studies focus on the shear forces that arise due to the fluid flow in the bone matrix when subjected to mechanical loading (Weinbaum et al., 1994; Bacabac et al., 2004; Kreke et al., 2008; Ban et al., 2011). Different phenomena, of which one is biological growth, are thought of as evolving processes governed by goal functions in the study by Klarbring et al. (2015). Their results are interesting because it opens a possibility to follow an evolving material structure giving details of its internal characteristics. Other studies suggest an indirect dependence on mechanical load. One such theory, which suggests that the nutrients which are important for bone building are moved through the bone matrix by means of stress driven diffusion, has been tested by the present research group (Lindberg et al., 2015). In that study it was suggested that bone growth appears where the concentration of nutrients is high rather than where the stresses are high. Similar theories using strain driven diffusion in bone tissue has also been presented (Piekarski and Munro, 1977; Knothe Tate and Niederer, 1998; Banks-Sills et al., 2011). The importance of mechanical load is also investigate in the papers by Moore et al. (2014) and Knothe Tate et al. (2016). In Moore et al. (2014) the behaviour of tissue genesis by periosteal progenitor cells within a long bone defect is modelled, where the strains in the periosteum is input to the model. In Knothe Tate et al. (2016) stem cell growth and remodeling through mechanical feedback is modelled.

Load induced fluid flow may enhance the transport of key substances for bone remodelling throughout the bone matrix (Piekarski and Munro, 1977; Knothe Tate and Niederer, 1998; Knothe Tate et al., 1998; Steck et al., 2000; Knothe Tate et al., 2000). Mathematical models (Piekarski and Munro, 1977; Kufahl and Saha, 1990; Knothe Tate and Niederer, 1998) to study stress-induced fluid flow in the lacunar-canalicular system in an osteon suggests that such stress-induced flow may be important in bone remodelling, and that lack of such flow may be causing osteoporosis with immobilised individuals. The mechanisms of how solutes transport in bone have been studied, and how the removing of the waste products that are stored in skeletal tissue is accomplished (Piekarski and Munro, 1977; Maroudas, 1979; Maroudas et al., 1992; Knothe Tate and Niederer, 1998; Knothe Tate et al., 1998; Fernandez-Seara et al., 2002). It was understood that one of the important mechanisms is diffusion, that plays an essential role in accomplishing the transport and also in the removal of waste products. In other studies, it is shown that there is a strong correlation between diffusion coefficients and healthiness of bone, and it is found that the diffusivity in degenerated bone is significantly lower than in normal bone (Piekarski and Munro, 1977; Knothe Tate and Niederer, 1998; Kealey et al., 2005).

A body of work (Knothe Tate et al., 1998, 2000; Tami et al., 2003; Fritton and Weinbaum, 2009; Cardoso et al., 2013) nicely summarise much of the research carried out

this far. Exactly which nutrients that are involved in the process of bone modelling and remodelling are not fully mapped out, but *in vivo* studies (Jee et al., 1990) showed that prostaglandins stimulate osteoblast activity and it has also been found that nitric oxide can prevent bone resorption since it decreases the recruitment of bone resorbing osteoclasts (Fan et al., 2004).

In a recent study (Ganghoffer et al., 2015) a one-dimensional phase-field model was used to understand bone growth. By focusing on osteoclasts that remove bone tissue, they obtain a corrosion-like model. They assume that growth promoting cells (osteoblasts and osteocytes) later take over and fill out the created space.

In the present study Erwin Schrödinger's idea of living cells that seemingly decrease the entropy is used in a two-dimensional phase-field model. The idea is describe in Schrödinger's book "What Is Life? - The Physical Aspect of the Living Cell" (E. Schrödinger, 1944). Schrödinger's discussion is based on Delbrück's discovery that the hereditary substance hidden in living cells is the nucleus, later identified as the DNA. Schrödinger develops a theory that requires the concept of negative entropy or as he expresses it "entropy, taken with the negative sign". As such it is itself a measure of order. The entropy is, as discovered by Boltzman and Gibbs, always increasing in all closed systems, which led Schrödinger to include a larger system with hidden supplies of negative entropy. The origin of the negative entropy might be complex but clearly the ultimate supply on earth would be the sun. Here it is assumed that the release of elastic energy plays a role in the increase of order via the action of the DNA. By that the processes leading to bone growth process is supposed to feed on the virtual uptake of an energy corresponding to a negative fraction m of the elastic energy. Bone growth takes place at the outer bone surface, the periosteum. It is believed that nutrients are transported from the existing cortical bone and out to the periosteum where bone building osteoblasts are activated. The transport is believed to proceed at a sufficiently high pace so that lack of nutrients never occurs. The activation process is assumed to include release of free mechanical energy and dissipation of chemical energy. The chemical energy potential is describing the motion on the microscopic level towards local states with minimum potential energy which in the present study are either the organized bone structure or a disintegrated non-solid state. This is considered to be in analogy with solid-viscous or solid-gaseous system where the phases are kept apart by a barrier of higher potential energy. The strain energy also strives to be minimized which is done by simply removing the material which is being strained. Fundamental thermodynamics say that the entropy, i.e. the disorder, increases in a system with increasing energy. As living tissue can add material where loading is high, its seems as the cells can actually decrease the entropy, i.e. increase the order of the material structure. The cells would of course release heat in the process and hence the total entropy in the biosphere increases, but locally the entropy decreases, i.e. material is added. This hypothesis is tested in this paper by giving the strain energy a negative weight factor, i.e., high strain energy would trigger the recruitment of material rather than dissolving it.

2 Theory

With this background the co-acting processes are assumed to be diffusion, phase transformation and elastic deformation. Other forms of energy apart from diffusion, phase and strain energies are assumed to remain constant. Space is assumed to consist of either bone or not. As described above this physically embodies the solid bone as opposed to a disintegrated state. In the latter state all prerequisites for forming bone apart from the necessary free energy, may be present. Here the phase field variable ψ, is used to keep track of the solid state, i.e., the bone. The considered energies are functions of ψ and its gradients, $\nabla\psi$. The total free energy density F is assumed to be composed of diffusion, phase and strain energies densities as follows

$$F = F_{ch} + F_{gr} + mF_{el} \,, \tag{1}$$

where the energy densities F_{ch}, F_{gr} and F_{el} [F/L^2] here represent the chemical potential, the gradient energy and the elastic strain energy respectively. The brackets [...] mark units, L, F, T and -, for length, force, time and non-dimensional respectively.

The scaling factor $m\,[-]$ is unity in classical physics. In the present analysis m is supposed to be negative. The idea that was suggested by Erwin Schrödinger (E. Schrödinger, 1944) is again that living cells may produce negative entropy, at least seemingly. The gradient energy is responsible for the diffusion of matter, and the chemical potential is the binding energy required to remove a single cell layer at the bone surface. Neither of these are, in the present context, supposed to be different for a living cell vis á vis all other particles. Here it is assumed that the role of the elastic energy could be affected by the complex interaction of advanced molecules during the formation of the bone cells. The consequence could then be an apparent reduction of the entropy invoked by putting $m < 0$.

In the present case a phase field variable ψ [-] is used. The scaling may be arbitrarily selected without affecting the result. To simplify the mathematical presentation, ψ is limited to the interval $|\psi| \leq 1$, where $\psi = -1$ defines the absence of bone and $\psi = 1$ defines fully developed bone. The fully developed phase is suggested to be a dense cortical bone. For this reason ψ is mostly close to 1 or -1, i.e. bone or not bone. There is a region where the material is a weak solid and not fully developed bone. For this region $|\psi| \leq 0.9$, and is called the transition zone. Focus of the growth process concerns the transition zone. It is believed in this study that the bone promoting substances is of no use as long as they are in areas of fully developed cortical bone.

This study utilizes the Ginzburg-Landau theory to describe the development of the bone. The time dependent Ginzburg-Landau relation may be written

$$\frac{\partial\psi}{\partial t} = -L_\psi \frac{\delta F}{\delta\psi} \,, \tag{2}$$

where $\frac{\delta F}{\delta\psi}$ is the variation of F with respect to variation of the material state ψ, cf. Ginzurg and Landau (1950). It is assumed that $F = F(\psi, \psi_{,i})$. Gradients of higher order than $\psi_{,i}$ are assumed to be insignificant. The mobility coefficient L_ψ [L^2/FT] is a positive constant. The Euler-Lagrange equation can be used to express the right hand side term in eq. (2), i.e. the variation of F, as

$$\frac{\delta F}{\delta \psi} = \frac{\partial F}{\partial \psi} - \frac{\partial}{\partial x_i}\frac{\partial F}{\partial \psi_{,i}} \,. \tag{3}$$

In biology the transformation of weak tissue to stiff is well known. During healing of damaged bone and during continuously ongoing bone remodelling the precursor to bone, callus, goes through such a transformation of its mechanical properties. By use of Micro-CT images for geometrical and structural input to a finite element simulation, Rehak and Skallerud (2014) made the conclusion that the CT obtained opacity converted to densities are providing sufficient information of the mechanical state.

The chemical energy potential, also called the Landau potential (Ginzurg and Landau, 1950), should fulfil the condition $\partial F_{ch}/\partial\psi \to 0$ as $|\psi| \to 1$ to prevent $|\psi|$ from exceeding 1. On its simplest polynomial form it is written for two phases,

$$F_{ch} = p(\frac{1}{4}\psi^4 - \frac{1}{2}\psi^2) \,, \tag{4}$$

where p [F/L^2] is a material parameter. The expression has minima at $|\psi| = 1$ and the potential strives to bring the state, ψ, towards any of the two minima.

The gradient energy is, with index notation using Einstein's summation rule, written

$$F_{gr} = \frac{g_b}{2}\psi_{,i}\psi_{,i} \,. \tag{5}$$

The notation $(.)_{,i}$ imply the gradient $\partial(.)/\partial x_i$ of the quantity $(.)$. The constant g_b [F] is a material parameter which affects the width of the transition zone. The gradient energy F_{gr} creates diffusion. The driving force is towards decreasing gradients until the gradients and the gradient energy vanish.

The strain energy for a linear elastic behaviour is in general formulated as

$$F_{el} = \frac{1}{2}\sigma_{ij}\epsilon_{ij} \,. \tag{6}$$

The stress state is uniaxial for pure bending and uniaxial tension and the only stress component, σ_{33}, is the stress normal to the studied bone cross-section. Therefore the stresses depend only on Young's modulus in the x_3-direction, E [F/L^2]. The stiffness of cortical bone often gradually increases from the inner perimeter to the exterior, because of the changes in porosity. The variation in porosity may be from 2 to 20% of volume in cortical bone (Winkelstein, 1950). This most probably affects elastic modulus and hence the evolution of the bone cross section.

In this generic study the analysis is simplified by assuming that Young's modulus, E_b, of the fully developed bone is constant. The development of bone is assumed to be a function of the phase field variable, ψ. Should the bone vanish then Young's modulus is expected to vanish and, reversely, for fully developed bone it should assume the value E_b. The released strain energy provides a driving towards fully dense bone, which vanishes when the material is in a stable configuration. Therefore it is required that $\partial F_{el}/\partial\psi \to 0$ for $|\psi| = 1$. The simplest polynomial form is

$$E = \frac{1}{4}(2 + 3\psi - \psi^3)E_b \,. \tag{7}$$

Poisson's ratio is not required in the present study.

In an experiment by Rubin and Lanyon (1984) turkey ulnas were subjected to compressions and the bone growth was studied. The geometry used in this current paper is the same as one of the cross-sections presented in their paper. The geometry is located in the $x_1 - x_2$ plane (Figure 1). In the experiment (Rubin and Lanyon, 1984) the neutral axis over the cross-section was measured with strain gauges, and their neutral axis is chosen as the x_1-axis in this paper. In this paper the compressions in Rubin and Lanyon (1984) is believed, due to the curvature of the bone, to give rise to a bending moment. The reason why the neutral axis in Rubin and Lanyon (1984) did not coincide with one of the two principal axes of the cross-section is due to the combined load case of compression and bending. Applying a bending around a neutral axis results in bending only about this specific axis. The only stress component is the out-of-plane stress σ_{33}.

In this paper two load cases are evaluated. In the main load case the bending at all times takes place around the second geometrical principal axis of the cross-section, also called the minor centroidal axis (Figure 1a). It is reasonable to believe that a body subjected to an external load will bend in the direction of least resistance, which here would be to where bending occurs around the minor centroidal axis of the cross-section. This hypothesis postulate is borne out by numerous experiments including Steck et al. (2003), Lieberman et al. (2004) and McBride et al. (2011) and is also strengthen by the fact that in the experiment (Rubin and Lanyon, 1984) the neutral axis for natural loading (wing flapping) was measured to be fairly close to the, in this current study, calculated minor centroidal axis of the cross-section. Hence the main load case simulates a bone that can deform freely and so the neutral axis will coincide with the minor centroidal axis. In a second case a bending is applied around the x_1-axis (Figure 1b) treated as the neutral axis. The bending then gives the same stress distribution over the cross-section as in Rubin and Lanyon (1984). It is further believed that no torsion took place in Rubin and Lanyon (1984) and the bone is here treated as slender in comparison to its diameter allowing a Bernoulli-Euler theory for pure bending. Hence, in both load cases the only occurring stress component will be the out-of-plane stress σ_{33}. Tendons that connect muscles to bone introduces a skew deformation of the bone. The shear stress that arise is rearranged into a tensile/compressive and bending loads. The areas where the tendons are attached to the bone are not treated in the present analysis.

Further it is assumed that the bone is an orthotropic material with a principal axis in the x_3 direction, i.e. $\sigma_{33} = E\epsilon_{33}$ where E is the principal stiffness in the x_3 direction. The elastic strain energy in eq. (6) becomes

$$F_{el} = \frac{1}{2}E(\psi)\epsilon_{33}^2\,, \tag{8}$$

and $E(\psi)$ a function of ψ according to eq. (7).

Figure 2 shows the chemical potential, the gradient potential and elastic energy with different magnitudes. By studying eqs. (4), (5) and (8) it is seen that the chemical potential and elastic energy are functions of ψ, and may be plotted without any specific choice of ψ. The gradient potential is a function of the derivative of ψ, and hence requires a specific choice of ψ in order to be studied. Here ψ is chosen as ψ=tanh(x/($\sqrt{}$(2)), which is the exact solution of ψ for a double well for a thin interface $|\psi| \leq 0.9$ for a flat surface in an infinite half-plane, see further Section 3. Also the combined results are shown for

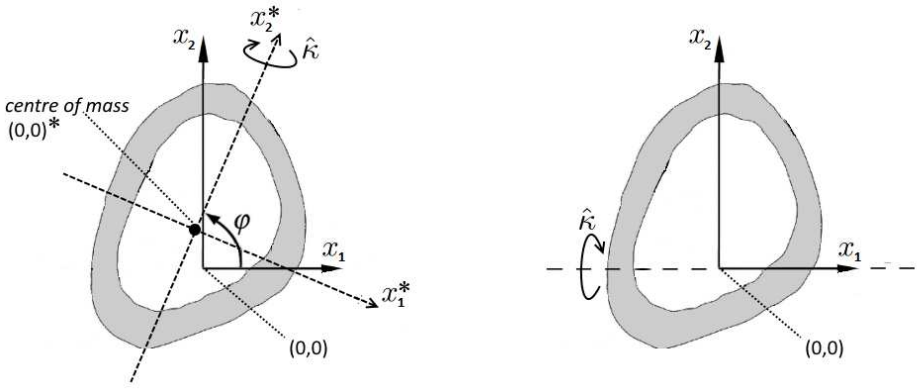

(a) (b)

Figure 1: Geometry and load cases, $\hat{\kappa}$ denotes the bending as defined in eq. (11). a) Main case with the global coordinate system $x_1 - x_2$ with the global origin, and the current system $x_1^* - x_2^*$ which are the geometrical main axes of the section with the centre of mass as origin. The $x_1^* - x_2^*$-system rotates and translates as the bone develops. b) Bending around a fixed axis.

the chemical potential and the elastic energy in Figure 2. In the absence of elastic energy the state is in a thermodynamic equilibrium at the three extreme points. At the left and right those are the two minima at $|\psi| = 1$ giving stable equilibrium whereas at the maximum in between is an unstable equilibrium. The latter represents a tipping point, where the driving force for evolving the phase vanishes. Everywhere except for here, the driving forces pushes the state towards either fully developed bone or the absence of bone, i.e., either one of the two stable states. The different graphs are due to elastic energies of different magnitudes. The elastic energy $m_2 F_{el}$ results in a single-well potential. For this case all initial states evolve toward a fully dense bone which is the only stable form of bone matter; There is only one extremum, i.e. that at $\psi = 1$. For a thin interface $|\psi| \leq 0.9$ for a perfect flat surface in an infinite half-plane, it is seen that the chemical potential and the gradient potential cancel eachother out.

By inserting eqs. (4), (5) and (8) into eq. (3), and then make use of eq. (2) the following is readily obtained as

$$\frac{\partial \psi}{\partial t} = -L_\psi \Big(p(\psi^2 - 1)\psi - g_b \psi_{,ii} - \frac{3}{8} m \epsilon_{33}^2 E_b (\psi^2 - 1) \Big) . \tag{9}$$

In the main case in this paper, i.e. bending around the minor centroidal axis, the strain in an arbitrary point becomes $\epsilon_{33} = \frac{1}{R}[x_1^* \cos(\varphi) + x_2^* \sin(\varphi)]$. The quantity $x_1^* \cos(\varphi) + x_2^* \sin(\varphi)$ becomes the perpendicular distance from the point to the minor centroidal axis if φ is the angle to the major centroidal axis, i.e. if $\varphi = \varphi_1$. R is the bending radius of the bone and x_1^* and x_2^* are the coordinates in the current system $x_1^* - x_2^*$ having the *current mass center* of the cross-section as the origin of the space. The angle to the major centroidal axis, φ_1, of the cross-section is found by using the second moment of area tensor for the cross-section. The mass center and the second moment of area tensor are continuously updated as the bone develops. In the second case where the load is applied around the x_1-axis, the strain becomes $\epsilon_{33} = \kappa x_2$. Let $z = x_1^* \cos(\varphi) + x_2^* \sin(\varphi)$ for

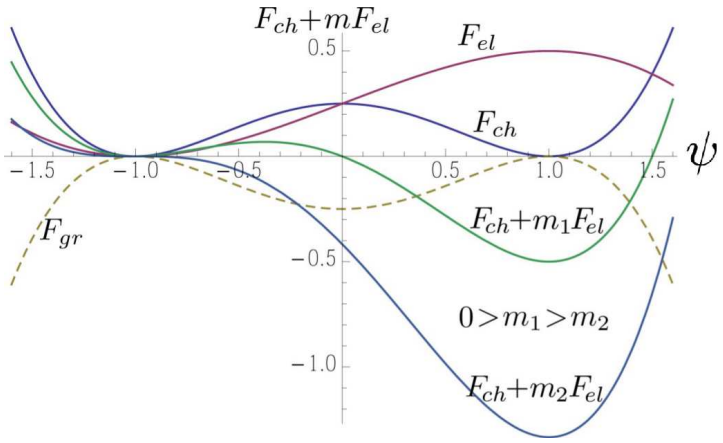

Figure 2: The free chemical, concentration gradient and elastic energies as functions of ψ, where $\psi = -1$ marks vanishing bone density, i.e. soft tissue virtually lacking reasonable stiffness and $\psi = 1$ that marks fully developed bone tissue. The energies are given in an arbitrary scale.

the main case and let $z{=}x_2$ for the second load case. Now the strain is alternatively

$$\epsilon_{33} = \kappa z\,, \quad \text{with}$$
$$z = \begin{cases} x_1^* \cos\varphi + x_2^* \sin\varphi & \text{main case} \\ x_2 & \text{second case.} \end{cases} \tag{10}$$

For convenience dimensionless variables are introduced. A length unit a [L] is introduced. In the selected shape a is the average bone wall thickness. By also introducing a time unit τ [T], non-dimensional variables may be selected as follows,

$$\tau = \frac{a^2}{L_\psi g_b},\ \hat{t} = \frac{t}{\tau},\ \hat{x}_i = \frac{x_i}{a},\ \hat{z} = \frac{z}{a},\ \hat{R} = \frac{R}{a},\ \hat{\kappa} = \frac{1}{\hat{R}}\sqrt{\frac{3E_b}{8p}},\ \text{and}\ \lambda = \frac{pa^2}{g_b}\,. \tag{11}$$

Now eq. (9) is written

$$\frac{\partial\psi}{\partial\hat{t}} - \frac{\partial^2\psi}{\partial\hat{x}_i\partial\hat{x}_i} = \left(\psi - m\hat{z}^2\hat{\kappa}^2\right)(1-\psi^2)\lambda\,. \tag{12}$$

As observed the left hand side of eq. (12) is Fick's law for the continuous quantity ψ with a diffusion coefficient which is independent of concentration and spatial coordinates. The right hand side represents driving force sources or sinks and may be compared to Fick's second law. The equation is also in analogy with Fourier's law with heat sources on the right hand side of eq. (12), which widens the range of numerical codes that can be used for the calculations.

With a selected negative value of m both right hand terms are contributing to $\partial\psi/\partial t$ for $\psi > 0$ meaning that both terms then act together to form bone structure. For $\psi < 0$ the chemical energy strive towards removing the bone while being counteracted by the elastic energy. As observed in Figure 2, below the lower limit m_2 for m the elastic energy dominates for all permissible ψ. As observed in eq. (12) $m = m_2 = (\hat{\kappa}\hat{z})^{-2}$, make the

chemical energy variation a single-well potential with a stable state only at $\psi = 1$, cf. Figure 2.

An exact solution for a flat surface at thermodynamic equilibrium is given by Ginzurg and Landau (1950) for zero load and by Ståhle and Hansen (2014) for arbitrary load as

$$\psi = \tanh(\sqrt{\frac{\lambda}{2}}\,\hat{x} - \lambda m \hat{z}^2 \hat{\kappa}^2 \hat{t}) = \tanh(\sqrt{\frac{p}{2g_b}}x - m\frac{3}{8}\left(\frac{z}{R}\right)^2 E_b L_\psi t)\,. \tag{13}$$

The statement is readily proved by direct insertion of eq. (13) into eq. (12). It is useful to know that $\mathrm{d}^2\tanh(x)/\mathrm{d}x^2 = (\mathrm{d}/\mathrm{d}x)\mathrm{sech}^2(x) = -2\,\mathrm{sech}^2(x)\tanh(x)$.

3 Analysis

For the numerical analysis the finite element software Abaqus is used. In Abaqus it is possible to include the right hand side of eq. (12) in the analysis. In the numerical analysis eq. (12) is treated as the heat equation, where ψ corresponds to the current temperature and the right hand side of eq. (12) is included as a heat flux which is written in a Fortran subroutine to Abaqus.

Input data are a range of values for λ and $\hat{\kappa}$ must be given reasonable values which requires some investigation of the material parameters which define λ and $\hat{\kappa}$. The length scale a is chosen as the mean thickness of the initial bone geometry in this paper after measuring at four locations, where the x_1- and x_2-axis intersect the geometry. The shape selected for the present analysis is that of a ulna cross-section of a turkey, that has been the object of the experimental study in Rubin and Lanyon (1984).

The parameter λ can be estimated by studying the surface energy, γ. One alternative is to express the surface energy as the energy required to create crack surfaces. This is done via the brittle fracture toughness $K_{\mathrm{I}c}$, cf. Broberg (1999). Another alternative is to integrate the gradient energy across the surface as

$$\gamma = \int F_{gr}\mathrm{d}x = \int_{-\infty}^{\infty} \frac{g_b}{2}\left(\frac{\partial\psi}{\partial x}\right)^2 \mathrm{d}x = \frac{2}{3}\sqrt{2g_b p}\,, \tag{14}$$

where the body is assumed to be an infinite half-plane, cf. Massih (2011). For a flat surface the two alternatives give the surface energy as

$$\gamma = \frac{2}{3}\sqrt{2g_b p} = \frac{1}{2}\frac{K_{\mathrm{I}c}^2}{E_b}\,. \tag{15}$$

The fracture toughness should reflect the energy required to extend the surface area. Further the width, b, of the transition zone may be compared with the exact solution of eq. (12) for a flat surface $b = b_o$, which is defined as

$$b_o = \sqrt{8}\,\mathrm{arctanh}(0.9)\sqrt{\frac{g_b}{p}} \approx 4.16\sqrt{\frac{g_b}{p}}, \tag{16}$$

cf. Ginzurg and Landau (1950) for vanishing load and showed by Ståhle and Hansen (2014) to apply also for arbitrary load. A reference transition zone width related to the bone wall thickness, a, is defined as

$$b_{ref} = a/18\,. \tag{17}$$

The transition zone in this paper is the thickness of the outer surface of the bone, the periosteum, and the inner surface towards the medullary cavity, the endosteum. The periosteum consists of an outer fibrous layer and an inner cambium layer while the endosteum is a single layer of connective tissue. Both the periosteum and the endosteum are very thin, for a grown up human the periosteum in mid diaphysis femur is about 0.1-0.2 mm depending on age (Moore, Milz and Knothe Tate, 2014), and the endosteum is even thinner.

The intention is to find solutions for long bones of a class of animals with thin periosteal and endosteal layers. The turkey is included because of the aforementioned experiment (Rubin and Lanyon, 1984). It is explained in Section 4 why the choice of λ does not matter as long as the ratio b/a is sufficiently small. In the light of this a width of 0.1 mm does not appear as particularly large neither for humans with a=7 mm or turkeys, a=1.8 mm. For turkeys, the ratio of width of periosteum, i.e. the transition zone, to the bone wall average thickness then becomes 1/18.

A relation between λ and b_o is obtained after elimination of p/g_b using eqs. (11) and (16),

$$b_o = 4.16\, a/\sqrt{\lambda}\,. \tag{18}$$

For sharp interfaces the surface energy becomes the only relevant quantity that affect the properties of the transient zone. For the phase field model all cases for which the transition zone width is sufficiently small, only the product $g_b p$ is relevant, cf. eq. (15). Opposed to this the ratio g_b/p and thereby the transition zone width becomes irrelevant. The same goes for the form of the chemical energy potential (cf. eq. (4)), as long as the energy barrier between fully developed bone ($\psi = 1$) and the absence of bone ($\psi = -1$) integrates to give the same surface energy, γ.

In the present analysis the expected zone width b_o for a flat surface is selected small so that the sharp interface limit is obtained, cf. Caginalp (1989) and Caginalp and Xic (1993). This gives a numerical advantage, while the high numerical resolution that otherwise would have been necessary for very thin transition zones, would make the calculations very time consuming, especially when the periosteum during the bone growth traverses an sizeable area. In Section 4 the implications and the restrictions of this is to be investigated.

4 Numerical considerations

The following concerns the selections that are made to legitimise the numerical method, especially regarding the parameters $\hat{\kappa}$ and λ. As explained in the previous section, the surface energy becomes the single parameter that defines the state of the interface and its interaction with the surrounding space, if the width of the transition zone is sufficiently thin. It seems obvious that the width of the transition zone should be sufficiently small compared first hand to the bone wall thickness and second hand other characteristic dimensions of the body, e.g. the inner and outer radii. However, the practical implications of the requirement remains to be defined. Apart from this, an additional complication is that the width of the transition zone must not be so small that the element size compromises the necessary resolution of the transition region and the growth processes.

Therefore a number of calculations were made for the main case, where the bending occurs around the minor centroidal axis, i.e. the x_2^*-axis, where a series of transition zone widths are calculated by using different b_o in the range 1 to $32b_{ref}$, cf. eq. (17). The desired widths are obtained by putting

$$\lambda = \frac{8\text{arctanh}(0.9)^2 a^2}{b_o^2} \approx 5610(b_{ref}/b_o)^2\,, \tag{19}$$

using eqs. (17) and (18). Further, by inserting eqs. (15), (17) and (18) into eq. (16), following is obtained,

$$\hat{\kappa} = \frac{1}{\hat{R}}\sqrt{\frac{3E_b b_o}{8\text{arctanh}(0.9)\gamma}} \approx 0.06868\frac{1}{\hat{R}}\sqrt{\frac{E_b a b_o}{\gamma b_{ref}}}\,. \tag{20}$$

The surface energy is kept constant at $\gamma = 2.34 \times 10^{-6} a E_b$. The bending radius R in this section is $\hat{R} = 890$ [a] in all computed cases, see further Section 6. The load reference $\hat{R} = 890$ is selected to give stresses close to failure stress of a human femure.

The limiting results for a vanishing transition zone width should restore classical mechanics of discrete bodies. Commonplace objects of sizes on micron scale and above are generally assumed to be possible to treat as discrete bodies. The requirement is therefore that the transition zone is sufficiently thin compared with the bone wall thickness. In this section it is established what a sufficiently thin transition zones is. The investigation is done for a plane surface for which the surface energy is a constant material parameter. The only relevant parameter is the normalised curvature $\hat{\kappa}$ defined in eq. (20). The study may therefore without loss on generality be performed for variation of the ratio b_o/b_{ref} only.

The results are evaluated along the cut from A to B, and C to D, see Figure 3a. Focus is on the transition zones close to A and C evaluated along the respective cuts. The distribution of ψ around the intersection A is shown in Figure 3b, at four different times from initiation to $\hat{t}$=0.05. The markers show the intersections with element boundaries. The solid lines are least square fitted to the exact solutions for flat surfaces, $\psi = \tanh(\xi_1(\hat{x}_2 - \xi_2))$ for the distribution of ψ as functions of $\hat{x}_2$. The ξ_1 and ξ_2 are fitting parameters, which give the transition zone width and position

$$b = \frac{2}{\xi_1}\,\text{arctanh}(0.9)a \quad \text{and} \quad x_2 = \xi_2 a\,. \tag{21}$$

The position of the surface is defined as where $\psi = 0$. The corresponding procedure is applied also to the transition zone at C.

In Figure 3b, the distribution with the markers $\circ$ is the initial distribution of ψ given at $\hat{t} = 0$. The distribution, with markers $\times$, is at $\hat{t} = 0.060$. The time coincides with the arrival of the expanding bone phase at the coarser part of the FE mesh. Here the resolution is significantly lower in its leading part, $\psi \lesssim 0.5$, as can be observed in the figure.

Figures 4a and b show the calculated transition zone width, b, at A and C as functions of time. The width is scaled with the average wall thickness a. The result in Figure 5b may be compared with the analytical result, $b_o/a = 0.0556$, 0.1112, 0.1668 and 0.2224 for

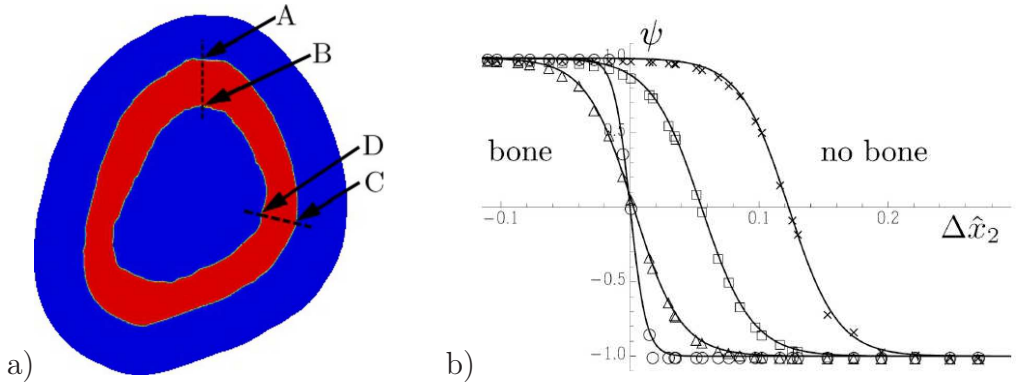

Figure 3: a) The position of cuts AB and CD across the bone wall. b) ψ at four different times along the cut. The markers $\circ$, $\triangle$, $\square$, and $\times$, show the result at increasing times. The solid lines are least square fitted analytical solutions eq. (13) for flat surfaces. The $\Delta\hat{x}_2$ is the distance to the initial position of the periosteum at A.

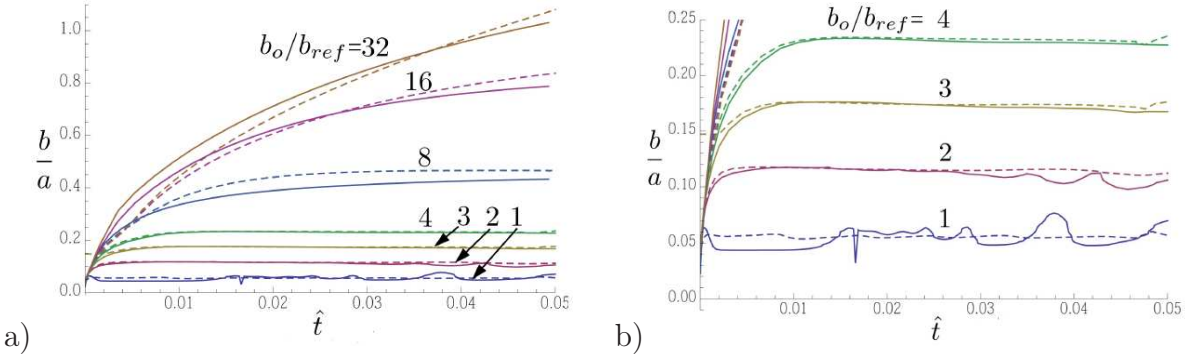

Figure 4: The present width b/a of the surface transition zone versus the non-dimensional time $\hat{t}$ (cf. eq. (11)). The cases are for b_0=b_{ref} to $32b_{ref}$, where $b_{ref} = a/18$. a) shows the result at at A (dashed) and C (solid curves). In b) is a zoom in of the same for the cases b_o from b_{ref} to $4b_{ref}$.

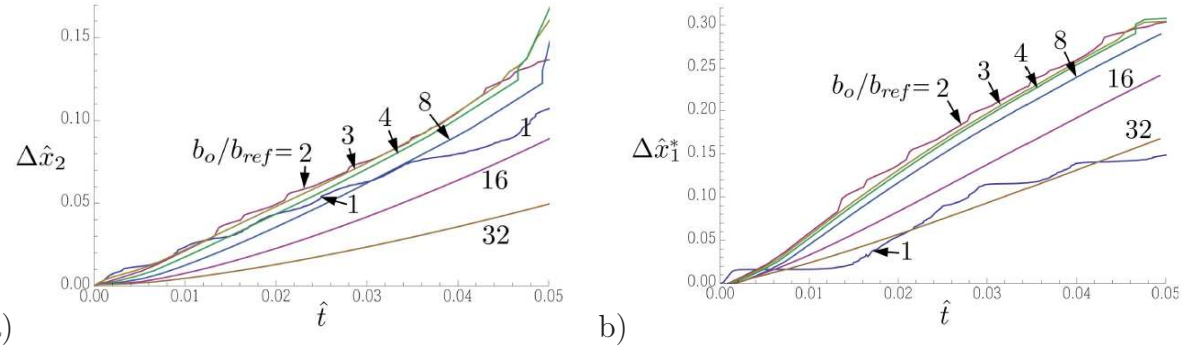

Figure 5: Bone growth versus non-dimensional time a) at A and b) at C along the major centroidal axis $\hat{x}_1^*$ (see Figures 1 and 3).

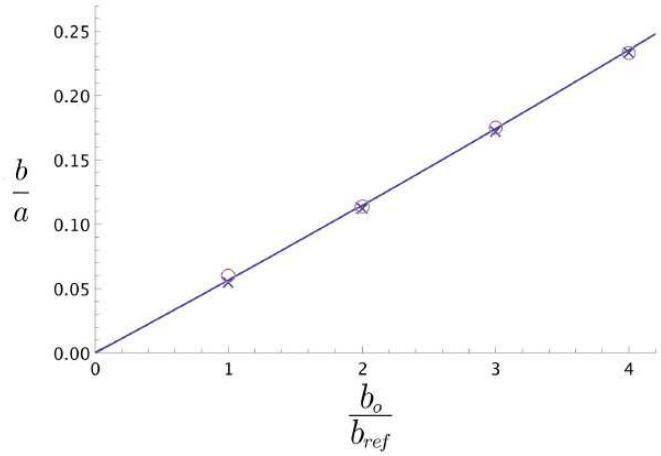

Figure 6: The transition zone width, b, in units a as a function of b/b_o for intersections at A ($\times$) and at C ($\circ$). The solid line is the second order polynomial. Deviation is less than 3.4% from the exact width at a flat surface. The comparison is made at $\hat{t} = 0.02$.

the cases b_o/b_{ref} = 1, 2, 3 and 4 according to eq. (16). For the case $b_o = b_{ref}$ one may note that there is scatter in the range ±20%, throughout the simulation. For $b_o = 2b_{ref}$ the scatter is less and around ±5%, starting at $\hat{t} = 0.03$. Cases $b_o = 2$ and $3\,b_{ref}$ does not show any comparable scatter. For all larger widths the initiation phase is prolonged so that none of the cases $b_o = 8$ to $32\,b_{ref}$ assume a steady state width.

The surface advancing $\Delta\hat{x}_2$, i.e. how the position for ψ=0 moves from its initial position, at A and at C are shown in Figures 5a and b. The graphs correspond to the cases as in Figure 4. Cases b_o equal to 2, 3 and 4 times b_{ref} closely follows a common history in until $\hat{t} \approx 0.048$. The case $b_o = b_{ref}$ suffers from scatter and diverges fairly early, and for the cases with the wider transition zones $b_o = 8\,b_{ref}$ to $32\,b_{ref}$ the deviations are very large. The immediate observation is that the nominal transition zones widths b_o=8 to $32b_{ref}$ are very large, being 40% and more of the wall thickness a.

Figure 6 summarises the resulting transition zone widths for $b_o \leq 4b_{ref}$. The result from intersections A and C according to Figures 4a and b, where least square fitted second

order polynomials are used to extract the transition zone width in the time interval $\hat{t}$=0.01 to 0.05 . A comparison of the width at $\hat{t} = 0.02$ show that the deviation from the flat surface result is 3.4%.

One conclusion is that $b_o \leq 4b_{ref}$may be considered to be small in the sense that the result is independent of b_o and should recover the sharp transition zone result. Hence, the result only depend on the surface energy. The flat surface width is obtained with good accuracy. Regarding the numerical method, i.e., the mesh dependant resolution is too small for $b_o = b_{ref}$. In more convenient terms this may be expressed as: b_o can be as large as $0.22a$ and should be covered by at least 13 elements.

5 Results and discussion

The desired widths are obtained by putting $p = (9/8)\gamma^2/g_b$ and modifying g_b. The surface energy is kept constant at $\gamma = 2.34 \times 10^{-6} aE_b$.

In the following subsections, the results are described in the described initial growth and the overview for the main case, with an instantaneously adopted bending around the minor centroidal axis and for the second case with bending around the x_1-axis, cf. Figure 1. As a result of the previous section b_o=$2b_{ref}$ is selected for the continuing analyses.

5.1 Initial growth

The intersection with the cut AB is selected for the observations. Growth occur at the periosteum (A) and the endosteum (B) (see Figure 3). The width of the transition zone at position (A) is displayed in Figure 7. As observed, the width is not significantly affected by the applied load. This in agreement with the exact result for a plane surface (Ståhle and Hansen, 2014). The result for the largest deformation $\hat{R} = 890$ show some numerically caused variations at around the time $\hat{t} = 0.04$. These variations are observed, only less visible because of the different scaling, in Figure 4. The reason is suggested to be a numerical effect emanating from fluctuations in finite element density. These anomalies appear later for lower loads which indicates that they are related to the mesh discretization and follows from the growth rates that increase with increasing loads. The deviation does not exceed 10% until after $\hat{t} = 0.06$ which is considered to be acceptable in the present study.

The growth rate for different loads have been estimated by use of least square fitting of a second order polynomial to the result for $0.02 \leq \hat{t} \leq 0.04$. Figure 8 shows the obtained data as solid curves and the polynomials as dashed curves. The rate is decaying with time, however almost invisible.

The resulting transition zone widths and growth rates are collected in Figures 9a) and b. The transition zone widths on the inside of the bone (B) are around 20% larger than the widths at the outer bone surface (A). The differences are observed to be less for larger deformation, i.e. smaller $\hat{R}$. At the smallest $\hat{R}$ here investigated, the width at B is less than 10% larger than the width at A. The difference in width observed for zero bending ($\hat{R} \to \infty$) indicates that the different surface shapes, convex at A and concave at B, influences the width. The observation may suggest that convex surfaces in general create a thinner transition zone and vice versa for a concave surface.

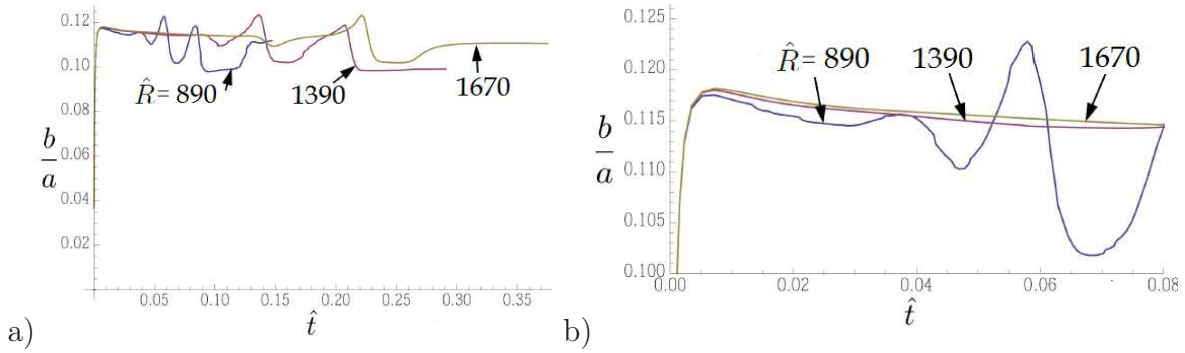

Figure 7: Width versus time for different bendings $\hat{R}$ at (A).

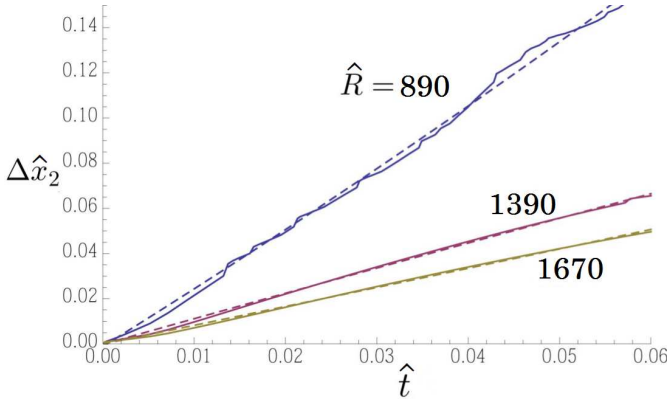

Figure 8: Growth versus time as in Figure 7. Results for different bending with $\hat{R}$=890, 1390, 1670 are shown. The dashed curves are least square linear approximations fitted to the growth data in region $0.02\hat{t}$ to $0.04\hat{t}$.

In Figure 9b) it is interesting to note that there is a lower limit for the bending radius, $\hat{R} \approx 9000$ at point A and $\hat{R} \approx 3300$ at point B, for promoting growth instead of resorption. The differences in growth is close to zero for vanishing bending, which indicates that the different shapes at A and B do not influence the growth rate; At both places the bone reacts with resorption at the same rate. With applied deformation given by a specified curvature, the periosteum (A) grows more than the endosteum (B). It is of course realized that the two surfaces are exposed to different deformations. The graphs reveal three different regions I) small loads give resorption on both the periosteum and endosteum, II) intermediate loads give resorption at the inner surface and growth at the outer surface and III) large loads give growth at both surfaces. At around $\hat{R}$=5000 the growth rate at the outer surface and the resorption at the inner surface are equal meaning that the wall thickness is maintained while the bone diameter is increasing.

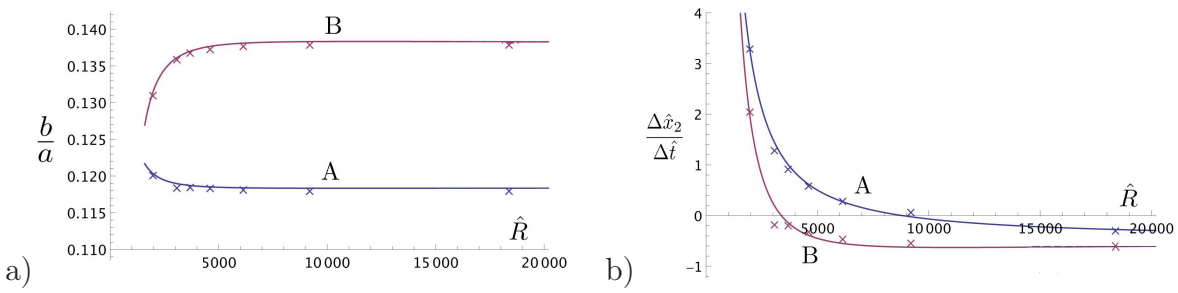

Figure 9: a) transition zone width versus bending radius $\hat{R}$ at positions A (blue) and B (red) at $\hat{t}$=0.02. A fitted approximation is included. b) Growth rate versus load at positions A and B otherwise same as a). Note that positive rate at the endosteum (B) means that the diameter of the medullar cavity is decreasing, i.e. (B) is then moving inwards towards the cavity.

5.2 Main case: Bending around the minor centroidal axis

In Figure 10 results are displayed for a transitions zone of $b_o = 2b_{ref}$. In Figure 10a the undeformed geometry is displayed where the initial loading axis (the minor centroidal axis) is shown together with the initial mass center of the bone section. In Figure 10c the transition zone at point C (cf. Figure 3a) is displayed at $\hat{t}$=0.005 for the deformation $\hat{R}$=890. The development of the full cross-section from three different bending deformation levels are then showed in Figure 10d, e) and f) at time $\hat{t}$=1, i.e. at times not discussed earlier. Here the bone growth appears to almost have stopped at about $\hat{t}$=0.4 as seen in Figure 11.

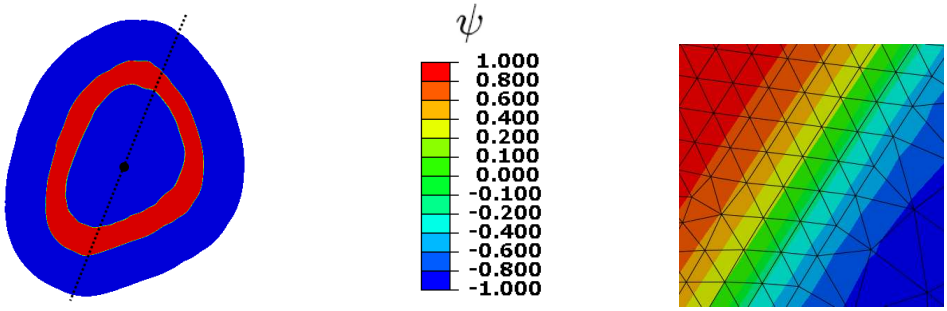

(a) Undeformed.

(b) Phase; 1 for bone and -1 for empty space.

(c) Transition zone at point C (cf. Figure 3a) at $\hat{t}$=0.005 for $\hat{R}$=890.

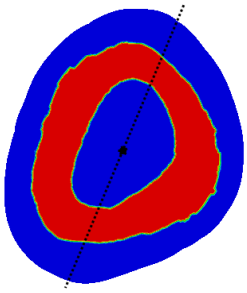

(d) $\hat{R}$=890 at $\hat{t}$=1.

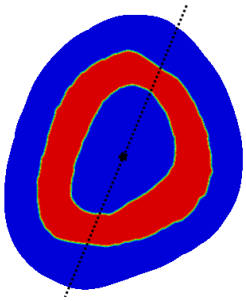

(e) $\hat{R}$=1390 at $\hat{t}$=1.

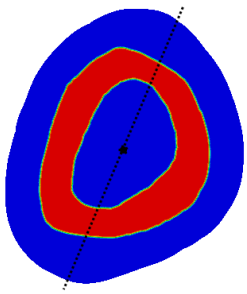

(f) $\hat{R}$=1670 at $\hat{t}$=1.

Figure 10: Results for different $\hat{R}$ for $b_o = 2b_{ref}$ for bending around the minor centroidal axis.

It is obvious that a more aggressive bending, i.e. higher loading, results in eventually more bone growth, as expected. In the cases Figure 10d, e) and f) the angle to the principal axes and the location of the mass center do not vary much during the development of the cross-section. In the undeformed geometry the angel to the load axis is 68° counter clockwise from the global x_1-axis, and the mass centre is located at $\hat{x}_1$=-0.23 and $\hat{x}_2$=1.27, while for $\hat{R}$=890 (Figure 10d) the angle is 68° and the mass centre is located at $\hat{x}_1$=-0.15 and $\hat{x}_2$=1.36.

It is also obvious that the bone growth appears to be highest where the strain energy is high, but the areas close to the minor centroidal axis differs in growth rate between the results. For the case with the largest bending, i.e. $\hat{R}$=890, there still is some bone

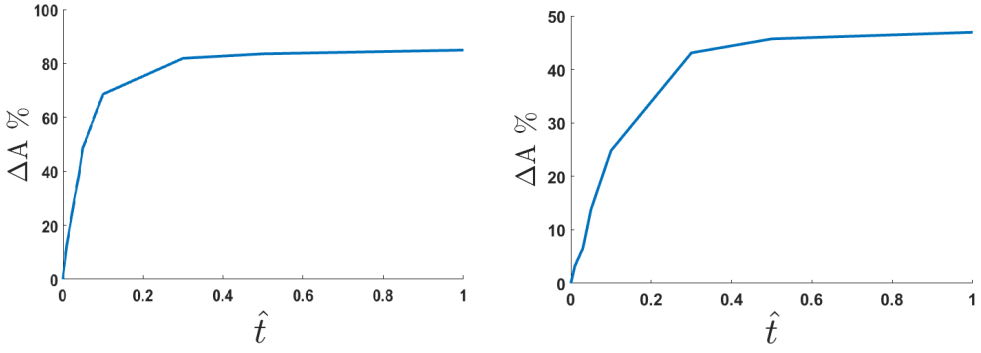

(a) $\hat{R}$=890. (b) $\hat{R}$=1670.

Figure 11: Area increase of the cross-section for two of the cases for $b_o = 2b_{ref}$.

growth taking place here even though the strain energy is zero here, but for the two other cases with lower loading the bone resorbs here.

In Table 1 the area increase in per cent is listed for the different models.

Table 1: Summary of the area increase for the transition zone width $b_o = 2b_{ref}$ at $\hat{t}$=1.

Bending $\hat{R}$	Area increase in %
890	85
1390	56
1670	47

5.3 Second case: Bending around a fixed axis

In Figure 12 the results where the load is applied around the x_1-axis are shown. Now the x_1-axis is treated as the cross-sections neutral axis, as explained in Sec. 2. The bone seems to develop more in this load case as compared to the results in Figure 10. Foremost it becomes obvious that the bone growth where the strain energy becomes high, hence the development becomes easier the farther away from the bending axis the material point is. The development continues until about $0.2<\hat{t}<0.4$. For the bending $\hat{R}$=890 the results are not representative for the reality. This results was not seen in the case where the bending took place around the minor centroidal axis. The reason is simply that in the case with bending around the x-axis the strain energy gets high enough to continue to develop bone.

The results in Figure (12) b) and c) may be compared to the findings of Rubin and Lanyon (1984). Their results are quit similar, except that they also observed rather high bone growth where the x_1-axis intersect the geometry to the very left in the figures.

In Table 2 the area increase in per cent is listed for the case where the bending occurs around the fixed x_1-axis.

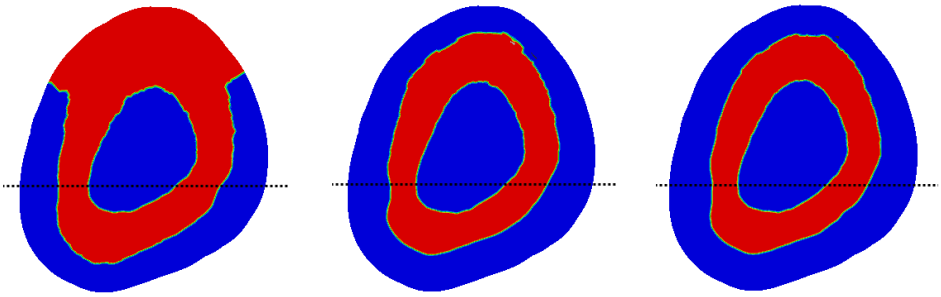

(a) $\hat{R}$=890. (b) $\hat{R}$=1390. (c) $\hat{R}$=1670.

Figure 12: Results for different κ and with $b_o = 2b_{ref}$ for bending around the fixed x-axis treated as a neutral axis.

Table 2: Summary of the area increase for bending around the x-axis at $\hat{t}$=1 for $b_o = 2b_{ref}$.

Bending $\hat{R}$	Area increase in %
890	-
1390	66
1670	58

6 Determining the analysis parameters

Reasonable values of λ and $\hat{\kappa}$ must be used to get useful results which can be connected to real material parameters using eq. (11). A way to chose λ and $\hat{\kappa}$ is described in the following. The choice in using dimensionless variables makes it possible to scale the results to any species as long as the shape of the cross-section do not vary to much. Here the values discussed are for humans. The calculated values are used as inputs for the analysis discussed and presented in previous sections. The values will be reasonable as first input to the dimensionless variables even though the analysis concerns avian ulna.

The two material parameters g_b and p can be estimated by studying the surface energy and the thickness of the transition zone as described in Section 3. If the mode I fracture toughness $K_{\mathrm{I}c}$ and Young's modulus E_b are known the surface energy γ may be determined using eq. (15) and the relation gives $\sqrt{g_b p} = \frac{3\sqrt{2}}{8} K_{\mathrm{I}c}^2 / E_b$.

To the authors knowledge a full parameter set to define $\hat{\kappa}$ and the time scale τ for is not available for neither turkey. Therefore supplementary data for humans is used. For a quantitative study, material data for the specie are required. The quality of the analysis is uncertain and the comparisons aim to elucidate the application of the model. All parameters may be obtained through simple experiments determining Young's modulus, the fracture toughness and the diffusivity constant of the most important growth controlling substance.

Adult developed bone tissue consists of about, by weight, to 60% of the bone mineral and to 30% of the organic matrix (osteoid) (Marcus et al., 2008). The bone mineral has the shape of small crystals consisting of impure hydroxyapatite and is embedded in the organic matrix. Several studies have investigated the fracture toughness $K_{\mathrm{I}c}$ of pure hydroxyapatite, giving values in the range of $K_{\mathrm{I}c}$ from 1.0 to 1.4 $\mathrm{MNm}^{-3/2}$ (Ioku

et al., 1990; Suchanek et al., 1996; Hervas et al., 2016). For human cortical bone K_{Ic} is suggested to be about $3\,\mathrm{MNm}^{-3/2}$ (Norman et al., 1995). In this paper the lowest value is chosen, i.e. K_{Ic}=$1\,\mathrm{MNm}^{-3/2}$. Young's modulus is chosen as 20 GPa, which is a mean value of several studies of human cortical bone in the femur and tibia (McCalden et al., 1993; Kemper et al., 2007; Duchemin et al., 2008; Malo et al., 2013). In all cases the fracture toughnesses are supposed to represent splitting of planes that are perpendicular to the longitudinal direction. Using K_{Ic}=$1\,\mathrm{MNm}^{-3/2}$ and Young's modulus E_b=20 GPa, eq. (15) gives

$$\sqrt{g_b p} = 0.0265\ \frac{\mathrm{N}}{\mathrm{mm}}. \tag{22}$$

The transition zone in this paper is the thickness of the outer surface of the bone, called the periosteum. A value of 0.1 mm for the transition zone is used, i.e. b_{ref}=0.1 mm. Eq. (16) then gives

$$0.1 = 4.16\sqrt{\frac{g_b}{p}}, \tag{23}$$

Using eq2. (22) and (23), g_b and p become

$$g_b = 6.3 \cdot 10^{-4}\mathrm{N} \text{ and } \ p = 1.1\ \frac{\mathrm{N}}{\mathrm{mm}^2}\,. \tag{24}$$

The ultimate stress σ_u of the human cortical bone has been found to be about 150 MPa in tension (Kemper et al., 2007). With the previous used value of E=20 GPa along with an outer radius r of an human femur set to e.g. 12 mm, a maximum bending radius R would be

$$R = \frac{r}{\sigma_u}E = 1600\mathrm{mm}. \tag{25}$$

After some convenient choice of the length scale a, $\hat{\kappa}$ and λ are calculated according to eq. (11).

7 A real case

If eq. (9) is studied, it is seen in that the quantity $L_\psi g_b$ is the diffusion coefficient for ψ as the relation between the gradient of the flux versus the rate of concentration decrease (cf. any text book on diffusion). The quantity $L_\psi g_b$ will have the dimension $[\mathrm{L}^2/\mathrm{T}]$. Indeed eq. (9) and eq. (12) are the same equations. The length unit in this study is chosen as a and the time unit as τ, hence the diffusion coefficient D has the dimension $[\mathrm{a}^2/\tau]$.

Again the choice in using dimensionless variables makes it possible to scale the results to any species. It has to be remembered that the analysis is based on the assumption that $a \gg b$. As an example the diffusion coefficient of potassium chloride, KCl, in the direction going from the endosteum to the periosteum in bovine femur (mid diaphysis) was estimated earlier by Lindberg et al. (2014), where the over all mean value of the diffusion coefficient became about $1.8 \times 10^{-4}\,\mathrm{mm}^2/\mathrm{s}$. KCl is possible not of direct interest for studying bone growth, however the value might be used to determine the diffusion coefficient of other substances in bone tissue with the same molecular weight. KCl has a weight of 74 Da (39 for potassium and 35 for chloride). It was assumed that the KCl diffused as separate ions through the micro porosity of the cortical bone.

By studying eq. (11) the time scaling becomes $\hat{t}=\frac{tL_\psi g_b}{a^2}$. The quantity $L_\psi g_b$, i.e D, is now set to $1.8\times10^{-4}\,\mathrm{mm}^2/\mathrm{s}$. In the results it was seen that for the lowest evaluated load ($\hat{R}$=1670), 10% growth was reached after $\hat{t}$=0.05. If the mean bone wall thickness a is set to 15 mm, (a typical value for a bovine femur) the actual time it would take to receive 10% growth becomes $t=a^2\hat{t}/D$=62 500 s, i.e. about 17 hours. I.e. 17 days if work out takes place for one hours a day. For a human (mid diaphysis) femur a might be chosen to 7 mm. Then the time until 10% bone growth is reached becomes about 4 hours (it assumed that cortical cow and human bone are similar). These exercise times are very short and suggest that important substances for bone growth have smaller diffusion coefficients. For instance, important substances for the remodelling process are the prostaglandins, e.g. prostaglandin E2 (PGE-2) (Jee et al., 1990) and the proteins BMP-2 (Wutzl et al., 2010; Moore et al., 2014). PGE-2 has a molecular weight of about 350 Da, and BMP-2 about 40 kDa. In the study by Patel et al. (2005) diffusion coefficients for tracers with the different sizes were investigated. The 300 Da tracer had a diffusion coefficient in the transverse direction of bovine cortical bone of $D=7\times10^{-8}\,\mathrm{mm}^2/\mathrm{s}$. With this value the exercise time for a human would be 405 days. Say that one can exercise one hours a day, it would take about 27 years to reach 10% growth. For the highest load ($\hat{R}$=890), the exercise time becomes 81 days, or about 5 years with one hours work out per day. For a bovine the same figure becomes 24 years.

8 Conclusions

By assuming that the transport of the matter necessary for bone growth is fast compared with the consumption in the growth process, a modified Ginzburg-Landau theory is successfully used for studying exercise promoted bone growth. The modification follows Schrödinger's theory concerning life molecules ability to decrease entropy (E. Schrödinger, 1944).

A finite element method is used to solve the obtained partial differential phase equation fully coupled with an exact Euler-Bernoulli beam solution for the mechanical state. Preliminary results show that mesh independent solutions are obtained if the linear extent of the finite elements in the bone surface transition zone is less than around 0.15 of the transition zone width b_o.

Further, by comparing physical parameters giving different transition zone widths, it is found that $b_o \leq 4b_{ref}$, e.g. around 4.5 times the width of a femur periosteum of a typical human, can be considered to be small. This is in the sense that the result becomes independent of b_o and recovers the sharp surface result. As a consequence the result only depends on the surface energy. All other properties of the transition zone develops without any interaction with the rest of the body.

The exact solution for a flat surface coincides as regards the transition zone width within only a one or two percent in the studied load cases for $b_o \leq 4b_{ref}$.

Very small external load leads to bone resorption. The minimum required load for growth is found and growth rate has been established. The analyses are performed in natural units where the length scale is given by the bones wall thickness and the time unit is given by the diffusion constant for the bone growth promoting specie.

The application to different animals requires bone size, and the diffusion coefficient

of a growth promoting agent. A fair guess would be that the agent is common for large groups of mammals, if not for all mammals.

Bovine and human bone where chosen as test cases. As an example of a bone promoting agent prostaglandin E2 was picked for both animals. The selected physical parameters suggest that the cross-section area increases 10% after 372 days for bovine and 81 days for human bone, effective loading, with the highest load investigated in this paper.

The case results should be taken with great caution whereas there is an expected large individual variation and also an uncertainty regarding the growth promoting agent. For immediate application, a suitable diffusion constant is suggested to be obtained by statistical fitting.

Funding

This research was funded by The Crafoord Foundation, Lund, Sweden, project 20170999. The authors are grateful to their financial support.

References

Cowin, S.C. (2001) 'Bone Mechanics Handbook 2nd Edition', CRC Press, Taylor and Francis Group, Florida, USA.

Bacabac, R.G., Smit, T.H., Mullender, M.G., Dijcks, S.J., Van Loon, J.J.W.A., Klein-Nulend, J. (2004) 'Nitric oxide production by bone cells is fluid shear stress rate dependent', *Biochemical and Biophysical Research Communications*, 315(4): 823-9. DOI: 10.1016/j.bbrc.2004.01.138

Ban, Y., Wu, Y.Y., Yu, T., Geng, N., Wang, Y.Y., Liu, X.G., Gong, P. (2011) 'Response of osteoblasts to low fluid shear stress is time dependent', *Tissue Cell*, 43(5): 311-7. DOI: 10.1016/j.tice.2011.06.003

Kreke M.R., Sharp L.A., Lee Y.W., Goldstein A.S. (2008) 'Effect of intermittent shear stress on mechanotransductive signaling and osteoblastic differentiation of bone marrow stromal cells', *Tissue Engineering Part A*, 14(4): 529-37. DOI: 10.1089/tea.2007.0068

Weinbaum, S., Cowin, S.C., Zeng, Y. (1994) 'A model for the excitation of osteocytes by mechanical loading-induced bone fluid shear stresses', *Journal of Biomechanics*, 27(3): 339-60. DOI: 10.1016/0021-9290(94)90010-8

Klarbring, A., Torstenfelt, B., Satha, G. (2015) 'Nutrient modulated structural design with application to growth and degradation', *Zamm-Zeitschrift für Angevandte Mathematik und Mechanik*, 95(11): 1323-1334. DOI: 10.1002/zamm.201400008.

Lindberg, G., Banks-Sills, L., Ståhle, P., Svensson, I. (2015) 'A Two-Dimensional Model for Stress Driven Diffusion in Bone Tissue', *Computer Methods in Biomechanics and Biomedical Engineering*, 19(5): 457-67. DOI: 10.1080/10255842.2013.807507

Piekarski, K., Munro, M. (1977) 'Transport mechanism operating between blood supply and osteocytes in long bones', *Nature*, 269(5624): 80-2 DOI: 10.1038/269080a0

Knothe Tate M.L., Niederer, P. (1998) 'A theoretical FE-based model developed to predict the relative contribution of convective and diffusive transport mechanisms for the maintenance of local equilibria within cortical bone', HTD - Vol. 362/BED - Vol. 40, *Advances in Heat and Mass Transfer in Biotechnology*, (Ed. S. Clegg) The American Society of Mechanical Engineers

Banks-Sills, L. Ståhle, P. Svensson, I. Eliaz, N. (2011) 'Strain driven transport for bone modelling at the periosteal surface', *Mathematical Bioscience*, 230(1): 37-44. DOI: 10.1016/j.mbs.2010.12.008

Moore S., Saidel G., Knothe U., Knothe Tate M.L. (2014) 'Mechanistic, Mathematical Model to Predict the Dynamics of Tissue Genesis in Bone Defects via Mechanical Feedback and Mediation of Biochemical Factors', *PLoS Computational Biology*, 10(6):e1003604. PMID: 24967742. DOI: 10.1371/journal.pcbi.1003604

Knothe Tate M.L., Gunning P., Sansalone V. (2016) 'Emergence of form from function: role of stem cell mechanoadaptation in sealing of cell fate', *BioArchitecture*, 6(5): 85-103.' DOI: 10.1080/19490992.2016.1229729

Knothe Tate M.L., Niederer P., Knothe U. (1998) 'In vivo tracer transport through the lacunocanalicular system of rat bone in an environment devoid of mechanical loading', *Bone*, 22(2): 107-17. DOI: 10.1016/S8756-3282(97)00234-2

Steck R., Niederer P., Knothe Tate M.L. (2000) 'A Finite Difference model of load-induced fluid displacements within bone under mechanical loading., *Medical Engineering & Physics*, 22(2): 117-25. DOI: 10.1016/S1350-4533(00)00017-5

Knothe Tate, M.L., Steck, R., Forwood, M.R., Niederer, P. (2000) 'In vivo demonstration of load-induced fluid flow in the rat tibia and its potential implications for processes associated with functional adaptation', *Journal of Experimental Biology*, 203(Pt 18):2737-45.

Kufahl, R.H., Saha, S. (1990) 'A theoretical Model for Stress-generated Fluid Flow in the Canaliculi-lacunae Net Work in Bone Tissue', *Journal of Biomechanics*, 23(2): 171-80. DOI: 10.1016/0021-9290(90)90350-C

Fernandez-Seara, M.A., Wehrli, S.L., Wehrli, F.W. (2002) 'Diffusion of Exchangeable Water in Cortical Bone Studied by Nuclear Magnetic Resonance', *Biophysical Journal*, 82(1): 522-9. DOI: 10.1016/S0006-3495(02)75417-9

Maroudas, A. (1979) 'Physicochemical Properties of Articular Cartilage', In: *Adult Articular Cartilage*, pp.215-90. Edited by MAR Freeman. Pitman Medical, London.

Maroudas, A., Schneiderman, R., Popper, O. (1992) 'The Role of Water, Proteoglycan, and Collagen in Solute Transport in Cartilage', In: *Articular Cartilage and Osteoarthritis*, pp.355-72. Edited by Kuettner, K.E., Schleyerbach, R., Peyron, J.G.,and Hascall, V.C., Raven Press, New York.

Kealey, S.M., Aho, T., Delong, D., Barboriak, D.P., Provenzale, J.M., Eastwood, J.D. (2005) ' Assessment of Apparent Diffusion Coefficient in Normal and Degenerated Intervertebral Lumbar Disks: Initial Experience', *Radiology*, 235(2): 569-74. DOI: 10.1148/radiol.2352040437

Tami A., Schaffler M.B., Knothe Tate M.L. (2003) 'Probing the tissue to subcellular level structure underlying bones molecular sieving function', *Biorheology*, 40(6): 577-90.

Cardoso, L., Fritton, S.P., Gailani, G., Benalla, M., Cowin, S.C. (2013) 'Advances in assessment of bone porosity, permeability and interstitial fluid flow', *Journal of Biomechanics*, 46(2): 253-65. DOI: 10.1016/j.jbiomech.2012.10.025

Fritton, S.P., Weinbaum, S. (2009) 'Fluid and Solute Transport in Bone: Flow-Induced Mechanotransduction', *Annual Reviews Fluid Mechanics*, 41: 347-374. DOI: 10.1146/annurev.fluid.010908.165136

Jee, W.S.S., Mori, S., Li, X.J., Chan, S., (1990) 'Prostaglandin E2 enhances cortical bone mass and activates intracortical bone remodelling in intact and ovariectomized female rats', *Bone*, 11(4): 253-366. DOI: 10.1016/8756-3282(90)90078-D

Fan, X., Roy, E., Zhu, L., Murphy, T.C., Ackert-Bicknell, C., Hart, C.M., Rosen, C., Nanes, M.S., Rubin, J. (2004) 'Nitric oxide regulates receptor activator of nuclear factor -κB ligand and osteoprotegerin expression in bone marrow stromal cells', *Endocrinology*, 145(2): 751-9. DOI: 10.1210/en.2003-0726

Ganghoffer, J.-F., Rahouadj, R., Boisse, J., Forest, S. (2015) 'Phase field approaches of bone remodeling based on TIP', *Journal of Non-Equilibrium Thermodynamics*, 41(1): 49-75. DOI: 10.1515/jnet-2015-0048.

Schrödinger, E. (1944) 'What is life? - The Physical Aspect of the Living Cell', *Cambridge University Press*, Cambridge, UK, 1-194.

Rehak, K., Skallerud, B., (2014) 'Micro-CT Based lmaging and Numerical Analysis of Bone Healing', *Key Engineering Materials*, 606: 141-4. DOI: 10.4028/www.scientific.net/KEM.606.141.

Ginzburg, V.L., Landau, L.D. (1950) Zh. Eksp. Teor. Fiz. 20(1064). English translation in: 'L. D. Landau, Collected papers', Oxford: Pergamon Press, 1965.

Winkelstein, B.A. (2012) 'Ortopaedic Biomechanics', *CRC Press*, Fl, USA, 2012.

Lanyon, L.E., Rubin, C.T. (1984) 'Static vs dynamic loads as an influence on bone remodelling', *Journal of Biomechanics*, 17(12): 897-905. DOI: 10.1016/0021-9290(84)90003-4

Steck R., Niederer P., Knothe Tate M.L. (2003) 'A finite element analysis for the prediction of load-induced fluid flow and mechanochemical transduction in bone', *Journal of Theoretical Biology*, 220(2): 249-259. DOI: 10.1006/jtbi.2003.3163

Lieberman, D.E., Polk, J.D., Demes, B. (2004) 'Predicting long bone loading from cross-sectional geometry', *American Journal of Physical Anthropology*, 123(2): 156-171. DOI: 10.1002/ajpa.10316

McBride S.H., Dolejs S., Miller R.M., Knothe U., Knothe Tate M.L. (2011) 'Major and Minor Centroidal Axes Serve as Absolute Reference Points to Test Mechanobiological Hypotheses Using Histomorphometry', *Journal of Biomechanics*, 44(6):1205-1208. DOI: 10.1016/j.jbiomech.2011.01.033

Ståhle, P., Hansen E. (2015) 'Phase field modelling of stress corrosion', *Engineering Failure Analysis*, 47: 241-251. DOI: 10.1016/j.engfailanal.2014.07.025

Broberg, K.B. (1999) 'Cracks and Fracture', *Cambridge University Press*, Cambridge, UK, 1-752.

Massih, A.R. (2011) 'Second-phase nucleation on an edge dislocation', *Philosophical Magazine*, 91(31): 3961-3980. DOI: 10.1080/14786435.2011.598883.

Moore, S.R., Milz, S., Knothe Tate, M.L. (2014) 'Periosteal thickness and cellularity in mid-diaphyseal cross-sections from human femora and tibiae of aged donors', *Journal of Anatomy*, 224(2): 142-49. DOI: 10.1111/joa.12133

Caginalp, G. (1989) 'Stefan and Hele-Shaw Type Models as Asymptotic Limits of the Phase-Field Equations', Physical Review A, 39: 5887-5896. DOI: 10.1103/PhysRevA.39.5887

Caginalp, G., Xic, W. (1993)'Phase-Field and Sharp-Interface Alloy Models', Physical Review E, 48: 1897-1909 DOI: 10.1103/PhysRevE.48.1897

Marcus, R., Feldman, D., Nelson, D.A, and Clifford J. Rosen, J.D. (2008) '*Osteoporosis, (3rd Edition)*', Elsevier Academic press, online.

Suchanek, W., Yashima, M., Kakihana, M,. Yoshimura, M. (1996) 'Processing and mechanical properties of hydroxyapatite reinforced with hydroxyabatite whiskers', *Biomaterials*, 17(17): 1715-23.

Ioku, K., Yoshimura, M., Somiya, S. (1990) 'Microstructure and mechanical properties of hydroxyapatite ceramics with zirconiad ispersionp repared by post-sintering', *Biomaterials*, 11(1): 57-61. DOI: 10.1016/0142-9612(90)90053-S

Hervas, I., Montagne, A., Van Gorp, A., Bentoumi, M., Thuault, A., Iost, A. (2016) 'Fracture toughness of glasses and hydroxyapatite: A comparative study of 7 methods by using Vickers indenter', *Ceramics International*, 42(11): 12740-50. DOI: 10.1016/j.ceramint.2016.05.030

Norman, T.L., Vashishth, D., Burr, D.B. (1995) 'Fracture toughness of human bone under tension', *Journal of Biomechanics*, 28(3): 309-20. DOI: 10.1016/0021-9290(94)00069-G

Malo, M.K.H., Rohrbach, D., Isaksson, H., Tüoyräs, J., Jurvelin, J.S., Tamminen, I.S., Krüger, H., Raum, K. (2013) 'Longitudinal elastic properties and porosity of cortical bone tissue vary with age in human proximal femur', *Bone*, 53(2): 451-8. DOI: 10.1016/j.bone.2013.01.015

Duchemin, L., Bousson, V., Raossanaly, C., Bergot, C., Laredo, J.D., Skalli, W., Mitton, D. (2008) 'Prediction of mechanical properties of cortical bone by quantitative computed tomography', *Medical Engineering and Physics*, 30(3): 321-8. DOI: 10.1016/j.medengphy.2007.04.008

McCalden, R.W., McGeough, J.A., Barker, M.D., Court-Brown, C.M. (1993) 'Age-related changes in the tensile properties of cortical bone. The relative importance of changes in porosity, mineralization, and microstructure', *The journal of bone and joint surgery*, 75(8): 1193-205. DOI: 10.2106/00004623-199308000-00009

Kemper, A., McNally, C., Kennedy, E., Manoogian, S., Duma, S. (2007) 'The Material Properties of Human Tibia Cortical Bone in Tension and Compression: Implications for the Tibia Index', Virginia Tech Wake Forest, Center for Injury Biomechanics, Paper number 07-0470.

Lindberg, G., Shokry, A., Reheman, W., Svensson, I. (2014) 'Determination of diffusion coefficients in bovine bone by means of conductivity measurement', *International Journal of Experimental and Computational Biomechanics,*, 2(4): 324-42. DOI: 10.1504/IJECB.2014.066086

Wutzl, A., Rauner, M., Seemann, R., Millesi, W., Krepler, P., Pietschmann, P., Ewers, R. (2010) 'Bone morphogenetic proteins 2, 5, and 6 in combination stimulate osteoblasts but not osteoclasts in vitro', *Journal of Orthopeadic Research*, 28(11): 1431-9. DOI: 10.1002/jor.21144

Patel, R.B., O'Leary, J.M., Bhatt, S.J., Vasanja, A., Knothe Tate, M.L. (2005) 'Determining the permeability of cortical bone at multiple length scales using fluorescence recovery after photobleaching techniques', *Proceedings of the 51st Annual Meeting of the Orthopaedic Research Society*, Washington D.C.

Paper C

Determination of diffusion coefficients in bovine bone by means of conductivity measurement

Gustav Lindberg, Abdallah Shokry, Wureguli Reheman and Ingrid Svensson

International Journal of Experimental and Computational Biomechanics

2014 2(4):324-342

https://doi.org/10.1504/IJECB.2014.066086 (2014)

Determination of diffusion coefficients in bovine bone by means of conductivity measurement

Gustav Lindberg[a], Abdallah Shokry[a,b], Wureguli Reheman[a] and Ingrid Svensson[a]

[a]Division of Solid Mechanics, Lund University
SE-221 00 Lund, Sweden
[b]Industrial Engineering Department, Fayoum University
63514 Fayoum, Egypt

Abstract

Measuring the diffusivity of various substances in cortical bone is in general difficult. For instance, making use of micro computed tomography requires agents that can be separated from bone, blood and other substances that exist in cortical bone. Here a more easily accessible method is presented. A series of cortical bovine bone samples were put in a saturated solution of potassium chloride for a time period that was long enough for the samples to be regarded as saturated. The samples were removed from the solution and molded in polyester leaving only the radial directions open. In the next step, the bone samples were put in distilled water and the conductivity of the water was registered over time. An analytical model fulfilling Fick's law was introduced and by means of Kalman filtering an estimation for the diffusion coefficient of potassium chloride in bovine bone is presented.

Keywords: *diffusion in bovine bone; diffusion experiment; conductivity measurement; Fick's law; Fourier series; Kalman filter; transient solution; experimental biomechanics*

1 Introduction

It is well known that bone, like other living tissue, has the function of self-repairing and can adapt its size and external shape, internal structure and mass density according to mechanical environment and hormonal changes. The modelling and remodelling is a dynamic process that involves removal of old bone tissue, resorption and formation of new tissue. This process is dominated by the activity of bone cells such as osteoblasts, osteoclast, osteocytes and bone lining cells. The cause of activation of these cells is widely discussed, and several hypotheses exist. A number of studies focus on the shear forces that arise due to the fluid flow in the bone matrix when exerted to mechanical loading. The hypothesis is that activation of the bone building osteocytes is directly or indirectly depending on shear forces, see for instance Weinbaum et al. (1994). The studies of Cardoso et al. (2013) and Fritton and Weinbaum (2009) nicely summarise some of the research carried out this far. In a recent published article by Lindberg et al. (2013a) a theory is tested which suggests that the nutrients which are important for bone building are moved through the bone matrix by means of stress driven diffusion, here having a special focus on the mathematical modelling of the process. A similar theory using strain driven diffusion in bone tissue is presented by Banks-Sills et al. (2011). Knothe Tate et al. (2000) hypothesize that load-induced fluid flow enhances the transport of key substances for bone remodelling throughout the bone matrix. Kufahl and Saha (1990) developed a mathematical model to study stress-induced fluid flow in the lacunar-canalicular system in an osteon, suggesting that it is possible that such stress-induced flow may be important in bone remodelling, and that lack of such flow may be one cause for producing osteoporosis due to immobilization. Some investigations show that molecules with lower molecular weight are dominantly transported through diffusion, while a pumping effect caused by mechanical load mainly controls the transportation of higher molecular weight solutes (Bali and Shukla, 2000; Tandon and Agarwal, 1989). In other studies, it is shown that there is a strong correlation between diffusion coefficients and healthiness of bone, and it is found that the diffusivity in degenerated bone is significantly lower than in normal bone, (Kealey et al., 2005).

Because of its complex micro and macro structure, and due to the minute size and inaccessibility of the lacunar-canalicular system that serves as a transportation network, the study of diffusion in bone is quite complicated. The mechanisms of diffusion of substances in the bone matrix, and the effects of mechanical load triggering bone cells to remodel, are poorly understood. The diffusion based magnetic resonance image (MRI) and nuclear magnetic resonance (NMR) methods have been used to characterize the structure, and evaluate the composition of bone (Burstein et al., 1993; Sigmund et al., 2008). Several studies have investigated the mechanisms of how solutes transport in bone, and how the removing of the waste products that are stored in skeletal tissue is accomplished. It was understood that one of the important mechanisms is diffusion, which plays an essential role in accomplishing these transports and also in the removal of waste products (Fernandez-Seara et al., 2002; Maroudas, 1979; Maroudas et al., 1992). Better understanding of the diffusion in bone is needed in biomedical research and medical application in order to study bone diseases, like osteoporosis, and the degradation of bone and fracture healing. For the various models that exist, using mechanical loading, the diffusion coefficient for the nutrient-bone system has to be determined in order to make

exact recommendation of load amplitude and frequency in order to maximize remodelling of bone. What kind of nutrients that are involved must of course also be determined, and research is ongoing. *In vivo* studies by Jee et al. (1990) showed that prostaglandins stimulate osteoblast activity and Fan et al. (2004) found that nitric oxide can prevent bone resorption since it decreases the recruitment of bone resorbing osteoclasts.

To directly study transport of matter through the complicated cellular structure of the bone matrix requires access to technically complicated instruments (e.g. NMR, CT scanners etc). To make research of such kind more accessible an experiment was set up in this study to investigate diffusion in bone by measuring electrical conductivity using a more common equipment, namely a conductivity meter. The diffusion parameters are extracted from the experimental result by using Kalman filtering, see Kalman (1960). This is a recursive method, here based on an analytical solution, for extracting values of unknown parameters from noisy input data. The mathematical analysis assumes that the bone is homogeneous.

Bone growth takes place at the outer bone surface, the periosteum. This study focuses on the diffusivity properties in the radial direction going from the nutrient rich bone marrow inside the bone out to the periosteum. It is believed that the diffusivity parameters of potassium chloride, KCl, in bovine bone found in this study may serve as an average over the bone cross-section and may be used to compute the transport in radial direction of the nutrients trigging bone growth at the periosteum.

2 Method

The right side femur of a 15 month old male bovine of type Charolais was step by step cut in to small bone cubes approximately of size 1 cm^3, see Table 1, giving a total of 16 pieces. The femur was cut up four days after slaughter, and up until then it had been stored in a fridge with the meet not yet removed. An important part of the process was, at all

Table 1: The mean values and the standard deviations for the side lengths for all samples.

Direction	mean value [mm]	standard deviation [mm]
Axial	9.97	0.38
Radial	9.70	0.65
Tangential	9.74	0.84

time, to keep track of the three axial directions (axial, radial and tangential) and where exactly on the femur each piece was taken from. The 16 pieces were taken from four places over the cross-section, see Figure 1. At each location two pieces were taken above the midplane and two below the midplane. In each row the samples were numbered from 1 to 4, where 1 is the sample closest to the proximal end and 4 closest to the distal end. Eight pieces were taken from the lateral side (outside), where four of them were located slightly towards the anterior side (front side) and the other four were located slightly towards the posterior side (back side). The other eight were taken from the medial side (inside), where four of them were located slightly towards the anterior side and the other four were located slightly towards the posterior side. During the process the pieces were kept in a freezer overnight holding a temperature of minus two degrees Celsius, making the bone

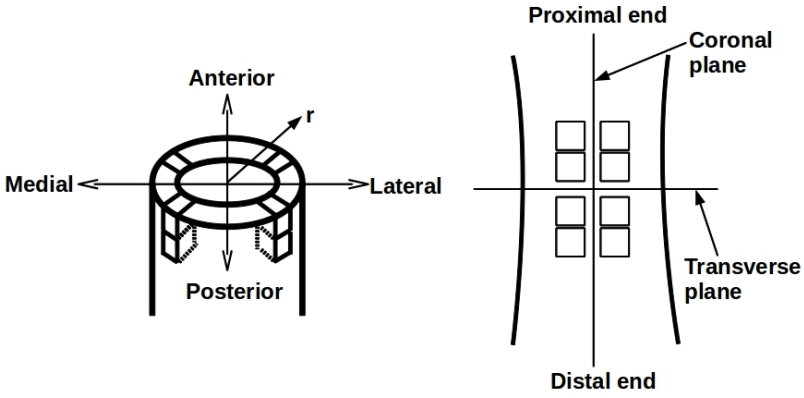

Figure 1: Location of samples.

barley freeze. On the day of experiment each set of samples was taken from the freezer and kept in room temperature for an hour, after which each piece was put in a beaker with saturated KCl solution which had been prepared by stirring 37 grams of KCl in 100 grams of distilled water. KCl was chosen since it has a high ability to conduct electricity, hence being suitable to use in conductivity measuring giving a strong read, along with the linear relationship between concentration and conductivity giving an easy mathematical approach. Although salts may affect the tissue, it is here believed that the mass transfer ability of the bone samples is not affected. The bone pieces were put in the beakers for 24 hours exposing them to a very high concentration, after which they were quickly rinsed with distilled water, lightly wiped with paper and then molded in polyester in order to close the axial and tangential directions leaving only the radial direction ends opened, see Figure 2. The choice of 24 hours was based on the assumption that this was enough to make the samples saturated. This is discussed further down. The polyester was left to

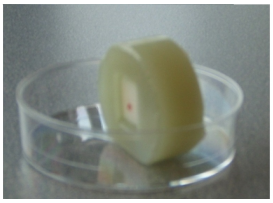

Figure 2: Polyester closing axial and tangential directions of bone sample.

dry for 60 minutes, after which the measurements started. The polyester did not give any conductivity increase for water when tested. During the experiments measurements were taken for samples that had been completely molded in with polyester after being in the salt solution, i.e. all six sides were closed. After 48 hours the conductivity had increased about 1 μS/mm. By that it was decided that the diffusion through the polyester from the closed sides could be neglected.

To measure the conductivity the instrument SevenEasy S30 from Mettler Toledo was used along with a cell that had two electrode plates. The samples were put in beakers with 100 ml distilled water where the ions that came from the KCl in each sample diffused into

the water and changed its conductivity. The increased conductivity was registered over time, and measurements went on for 24 hour for each sample. Before each measurement the beakers were stirred in order to obtain a homogeneous concentration. During night time automatic measuring was done for one sample taking values every second. The other three samples were not measured during night, here assuming that the progress behaves in the same manner for all samples. An overview of the experimental set-up for the measurements is shown in Figure 3. In general conductivity is measured in Siemens

Figure 3: The conductivity measurement.

per length unit, normally μS/cm where μ is the prefix for 10^{-6}. The conductivity ξ of a solution is determined as

$$\xi = G\,K = \frac{1}{\rho}K\,, \tag{1}$$

where G [S] is the conductance of the sample, which is the inverse of the resistance ρ [Ω]. The cell constant, or probe constant, K [cm^{-1}] is specific for the used cell, and consists of the ratio of the distance between the electrodes and the area of the electrodes. The cell constant must be determined which is done by calibrating the base unit for the used cell.

The experiments took place in a temperature controlled room, holding a constant temperature of 22 degrees Celsius. However, to be sure that the measurements did not get affected by some temporary temperature change, the in-built temperature compensation was used. Since pre-trials showed that the conductivity would be above 10 μS/cm, except for in the very beginning, but still not becoming strongly conductive the temperature dependence was assumed to be linear and so the conductivity is determined as (Down and Lehr, 2005)

$$\xi_{ref} = \frac{1}{1 + (\alpha/100)(T_{ref} - T)}\frac{K}{\rho}\,. \tag{2}$$

Here α is the temperature correction factor, T_{ref} is the chosen reference temperature and T is the actual temperature of the sample. If α is set to zero the actual conductivity of the sample is given, compare eq. (1). The correction factor is determined as

$$\alpha = \frac{(\xi_{T2} - \xi_{T1})100}{(T_2 - T_1)\xi_{T1}}, \tag{3}$$

and was for this experiment determined to α=2.1 meaning an error of 2.1% of the relative correction per centigrade.

3 Theory

3.1 Governing equations

The flux vector $\bar{J}$ of a selected substance in the bone environment becomes, due to differences in concentration of matter,

$$\bar{J} = -D\bar{\nabla}c\,. \tag{4}$$

Here D is the diffusion coefficient of the substance-bone system, being the same in all directions, and $\bar{\nabla}c$ is the gradient vector of the concentration where

$$\bar{\nabla} = (\frac{\partial}{\partial x}, \frac{\partial}{\partial y}, \frac{\partial}{\partial z}) \tag{5}$$

in a Cartesian coordinate system. Matter is assumed to be conserved and therefore the divergence of the flux $\bar{J}$ relates to the concentration as

$$\bar{\nabla}\bar{J} = -\dot{c}\,, \tag{6}$$

where the dot indicates the derivative with respect to time. If $\bar{J}$ is eliminated by using eq. (6), the divergence of eq. (4) becomes

$$\dot{c} = \bar{\nabla}(D\bar{\nabla}c)\,. \tag{7}$$

If the diffusion coefficient D is assumed not to be dependent of the current concentration nor explicitly dependent of spatial coordinates eq. (7) now changes to

$$\dot{c} = D\Big(\frac{d^2c}{dx^2} + \frac{d^2c}{dy^2} + \frac{d^2c}{dz^2}\Big)\,, \tag{8}$$

which is the partial differential equation to solve. Here x, y and z are serving as Cartesian coordinates. There is, of course, an option to choose a polar coordinate description, however with greater mathematical complexity. The cross-section of the long bone is not a perfect circle, but rather quite irregular. By that shifting to the standard cylindrical coordinate system is believed to be irrelevant. The bone pieces were hence chosen to be cut out as cubes so that the Cartesian coordinate system could be used. For each sample the coordinate system is placed so that the x-axis runs from the endosteum out to the periosteum, i.e. in the radial direction. To clarify that, x is replaced by r and eq. (8) is written as

$$\dot{c} = D\Big(\frac{d^2c}{dr^2} + \frac{d^2c}{dy^2} + \frac{d^2c}{dz^2}\Big)\,. \tag{9}$$

4 Mathematical model

A solution to the one-dimensional Fick's second law with a constant diffusion coefficient can be

$$C(r,t) = X(r)T(t)\,, \tag{10}$$

where the most general solution is readily given as (Crank, 1975),

$$C(r,t) = \sum_{m=1}^{\infty} \Big(A_m \sin(\lambda_m r) + B_m \cos(\lambda_m r) \Big) e^{(-\lambda_m^2 Dt)}\,. \tag{11}$$

In the experiment each sample had a volume of 1/100 of the surrounding water. By that the concentration increase in the water was ignored, and the boundary conditions were regarded as constant. See Lindberg et al. (2013b) for a comparison with the case where the increase of concentration at the boundaries is compensated for. For a one-

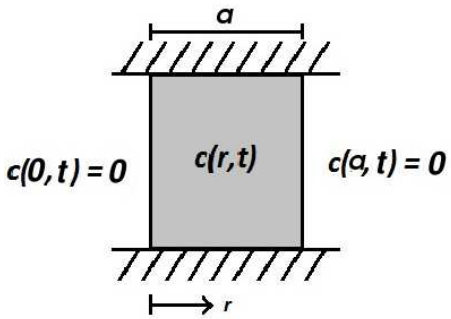

Figure 4: One-dimensional slab.

dimensional slab having an initial concentration of C_0 at $t = 0$ for $0 < r < a$ and the constant boundary conditions $C = 0$ at the boundaries $r = 0$ and $r = a$, see Figure 4, the solution becomes

$$C(r,t) = C_0 \sum_{n=1}^{\infty} e^{-\lambda_n^2 Dt} A_n \sin\Big[\lambda_n r\Big]\,, \tag{12}$$

where

$$A_n = \frac{4}{\pi} \frac{1}{(2n-1)} \tag{13}$$

and

$$\lambda_n = (2n-1)\frac{\pi}{a}\,. \tag{14}$$

More details about analytical diffusion problems can be found in e.g. the rigorous book by Glicksman (2000). The mean value $\tilde{C}_b$ of the concentration in the bone sample is given by taking the integral of eq. (12) over r and then divide it by the integration length a which is expressed as

$$\tilde{C}_b(t) = C_{b0}\frac{1}{a}\sum_{n=1}^{\infty} e^{-\lambda_n^2 Dt} A_n \int_0^a \sin(\lambda_n r)dr \,, \tag{15}$$

where index b is for bone. Deriving the integral the mean value of the concentration in the bone sample becomes

$$\tilde{C}_b(t) = C_{b0}\sum_{n=1}^{\infty} e^{-((2n-1)\frac{\pi}{a})^2 Dt}\frac{8}{\pi^2(2n-1)^2} \,. \tag{16}$$

From the experiments the conductivity ξ in the distilled water surrounding the bone sample was registered over time. The relationship between conductivity and concentration for a KCl solute is almost ideally linear. The relation between concentration and conductivity for a KCl solute is described by

$$C = \frac{\xi}{\varrho V} \,, \tag{17}$$

where V $[l^3]$ is the volume of the solute, ϱ has the unit S/l mole and l is the used length unit. The product ϱV [S l^2/mole] is the molar conductivity of the solute. The concentration C [mole/l^3] of matter in the solution may be described by the number of existing moles of matter m_i divided by the volume of the solution. The decrease of the concentration of KCl in the bone sample once put in the distilled water may hence be described by

$$\Delta\tilde{C}_b = \frac{-\Delta m_i}{V_b} \,. \tag{18}$$

Since the same amount Δm_i of KCl has diffused out to the distilled water, the increase of concentration of KCl in the water becomes

$$\Delta\tilde{C}_w = \frac{\Delta m_i}{V_w} \,, \tag{19}$$

where index w is for water. Using eqs. (17), (18) and (19) the change of conductivity of the water can be expressed as

$$-\Delta\tilde{\xi}_w = \varrho_w V_b \Delta\tilde{C}_b \,. \tag{20}$$

The mean conductivity $\tilde{\xi}_w$ of the distilled water may hence be modelled by

$$\tilde{\xi}_w(t) = A - B\sum_{n=1}^{\infty} e^{-((2n-1)\frac{\pi}{a})^2 Dt}\frac{8}{\pi^2(2n-1)^2} \,. \tag{21}$$

Here A $[\mathrm{S}/l]$ is the final value of the conductivity, i.e. the conductivity after infinity of time, since the dimensionless summation converges towards zero. $A - B$ is the start value, i.e. $\xi_{t=0}$, since the summation equals 1 for $t = 0$. It is by that very interesting to determine the constant B $[\mathrm{S}/l]$ as well as the diffusion coefficient D. If B is determined it can be calculated what the very end value A of the conductivity will be, and by that the measurements can be much more time effective.

4.1 Kalman filtering

In order to extract the diffusion coefficient a Kalman filter is used. The technique has several advantages; The random noise from the measurements and other process parameters is included into the equations and a non-linear behaviour can be included. The technique has shown very good results, which is obtained due to minimization of the mean square root of the difference between the measured conductivity and the model.

The Kalman filter is a versatile estimator and the algorithm operates recursively and results in an incrementally improved estimate of the model parameters D and B, whereas $A-B$ is obtained directly from a measurement immediately before the experiment starts. An introduction to the Kalman filter is, e.g., found in Brown (1983). Kalman filter recursive equations are expressed as

$$\hat{x}_k = \hat{x}_k^- + K_k[z - h(\hat{x}_k^-)], \tag{22}$$

$$K_k = P_k H_k^T R^{-1}, \tag{23}$$

and

$$P_k = \left[(P_k^-)^{-1} + H_k^T R^{-1} H_k\right]^{-1}. \tag{24}$$

Here $\hat{x}_k = [D_k \quad B_k]^T$ is an *a posteriori* estimate vector of the state that contains the two unknown parameters D and B at increment k. The vector $\hat{x}_k^-$ is an *a priori* estimate vector for the state at increment k and K_k is denoted the optimal Kalman gain. It is introduced to minimize the error of the *a posteriori* estimate at increment k. The vector z contains the measured conductivity at times t_i. The vector $h(\hat{x}_k^-)$ is a function that contains the analytical result, i.e. eq. (21), using the *a priori* estimated parameters $\hat{x}_k^-$ at times t_i.

The Kalman gain K_k is defined in eq. (23) using P_k, a matrix containing the *a posteriori* estimate of the error, and R, which is a scalar giving the maximum difference between the measurement z and the predicted result, as explained in more detail below. The matrix H_k is the derivatives with respect to B and D of $h(\hat{x}_k^-)$ at increment k and at times t_i.

The predicted non-linear conductivity function $h(\hat{x}_k^-)$ is a bi-quadratic form approximating eq. (21). The interpolation is performed for D and B in the region $D^{(1)} \leq D \leq D^{(3)}$ and $B^{(1)} \leq B \leq B^{(3)}$, where $D^{(1)}$, $D^{(3)}$, $B^{(1)}$ and $B^{(3)}$ are selected to give a sufficient span so that the given space includes the expected D and B. The remaining values $D^{(2)} = (D^{(1)} + D^{(3)})/2$ and $B^{(2)} = (B^{(1)} + B^{(3)})/2$. To be able to catch any possibly present local convergence sets for D and B, the algorithm is executed for many starting values $\hat{x}_0^-$. The initial state values $\hat{x}_0^- = [D_0 \quad B_0]^T$ are chosen as $11 \times 11 = 121$ equidistant values in the range $D^{(1)} \leq D \leq D^{(3)}$ and $B^{(1)} \leq B \leq B^{(3)}$. The predicted non-linear conductivity functions are computed using rectangular nine set Lagrange interpolation as

$$\left[h(\hat{x}_k^-)\right]_i = \sum_{p=1}^{3}\sum_{q=1}^{3}\left[\left(\prod_{m=1\neq p}^{3}\frac{D_k - D^{(m)}}{D^{(p)} - D^{(m)}}\right)\left(\prod_{n=1\neq q}^{3}\frac{B_k - B^{(n)}}{B^{(q)} - B^{(n)}}\right)\xi_{pq}\right], \tag{25}$$

where $\left[h(\hat{x}_k^-)\right]_i$ is element i, for time $t = t_i$, of $h(\hat{x}_k^-)$. Further, ξ_{pq} is the analytically calculated conductivity for $D = D^{(p)}$ and $B = B^{(q)}$, at time $t = t_i$ according to eq. (21). The matrix H_k is obtained by taking the derivative of the interpolated conductivity function and is expressed as

$$H_k = \left[\frac{\partial h(\hat{x}_k^-)}{\partial D_k}, \frac{\partial h(\hat{x}_k^-)}{\partial B_k} \right] . \tag{26}$$

A single iteration requires hours of computing time on a standard desktop computer using the analytical derivative of the model for 1000 terms while only a few seconds are required using the interpolation algorithm in eq. (25). Therefore, a little decrease of accuracy is accepted for a considerable saving of computer time.

The quantity R, being a difference between measurement and prediction, is computed as the largest difference in the entire set of measurements, i.e.

$$R = max_{i=1,2,..} \left(\left| \left(z - h(\hat{x}_0^-) \right)_i \right| \right) , \tag{27}$$

where the index i denotes vectorial element i, which corresponds to measurement and prediction at time $t = t_i$. The error R is usually an updated quantity. However, in the present case the result was found to be very insensitive to reasonable variations of R. Therefore R is chosen as the error according to eq. (27) as the value for the best out of all 121 initial state values for $\hat{x}_0^-$ that is used for analysing each experiment. The error R differs from one bone piece to another.

The Kalman filter update equations are given as

$$\hat{x}_{k+1}^- = \hat{x}_k \tag{28}$$

and

$$P_{k+1}^- = P_k + Q, \tag{29}$$

where Q is selected to be the unit matrix (Brown, 1983).

The initial value of the *a posteriori* estimate error is selected to be

$$P_0 = \begin{bmatrix} 100 & 0 \\ 0 & 100 \end{bmatrix} . \tag{30}$$

The process of extracting the unknown parameters is repeated for different ranges of initial state values ranging from larger range to smaller range until a good fitting between the measured conductivity and the model is obtained. The standard deviation σ_e of the difference between the experimental data and the obtained approximated Kalman data is determined according to

$$\sigma_e = \sqrt{\frac{1}{N} \sum (z - h(\hat{x}_k^-))_i^2}, \tag{31}$$

where N is the number of measurements. In Table 3 the final σ_e for each sample is shown.

5 Analysis and Results

The determination of the diffusion coefficient D and the constant B for the second bone sample from the medial posterior side, MP_2, is explained but the process for all bone samples follow the same strategy. The units used during the experiment were for convenience millimetres and minutes. The initial eleven different state values of D_0 were at first placed in the interval 0.0001 to 0.1001 mm^2/min with the midpoint 0.0501. For B_0 the initial eleven different state values were placed in the interval 10 to 90 μS/mm with the midpoint 50. These values were chosen to introduce an initially large range, and are based on experimental and preliminary curve fitting result.

The calculations were repeated with smaller range of initial state values until a sufficiently small standard deviation between the model and measured conductivity was found. The ranges and results are shown in Table 2. The combinations of D and B in

Table 2: Values of D, B and σ_e for four different initial ranges for sample MP_2.

Range for D_0 [mm^2/min]	Range for B_0 [μS/mm]	D [mm^2/min]	B [μS/mm]	σ_e [μS/mm]
0.0001-0.1001	10-90	0.00030	334.86	11.90
0.0010-0.0410	10-90	0.00212	94.087	4.010
0.0010-0.0110	10-90	0.00760	41.911	0.411
0.0060-0.0100	40-48	0.00749	42.805	0.298

$\hat{x}_0^-$ converged to one single point after some different iterations for the first, second, and fourth range but they converged towards two different points for the third range. Here 114 combinations of D and B converged to the point that fits well with the experimental data and seven combinations converged to another one that does not and can be excluded because it gave negative value for D with no physical meaning. Figure 5 shows the process of convergence between D and B after 1, 2, 10, 40, 120, and 500 iterations for sample MP_2 for the third range. The rectangle shows the border of the initial state range. A study was performed to investigate how many terms n that should be used in the summation operator in the model, see eq. (21). It showed that consistency can be reached after 10 000 terms. Extrapolation from this value to infinity of terms showed that the value for the diffusion coefficient changed by less than $5 \cdot 10^{-6}$ mm^2/min. Hence summation over 10 000 terms are used in this study.

The four different initial state ranges are figured with the experimental data for sample MP_2 in Figure 6. Table 2 along with Figure 6 show that the best approximated values that were achieved by the Kalman filter for D and B are 0.0074906 mm^2/min and 42.8049 μS/mm respectively for the MP_2 sample.

The process was performed in the same way for all samples. For the lateral posterior sample no 1, LP_1, the diffusion coefficient was for instance found to be 0.014360 mm^2/min and for sample no 2 from the lateral anterior side, LA_2, it was determined to 0.010660 mm^2/min. These results are plotted in Figure 7 and as can be seen the model has a good match with the experimental data. One observation is that the experimental data seems to behave more linear rather than exponential at the end of the measuring. The reason for this is unclear. It is possible that the real inhomogeneity of the bone tissue has a

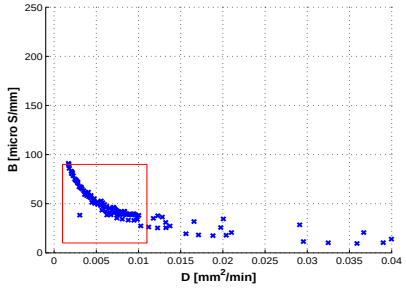

(a) Convergence after 1 iteration for MP_2.

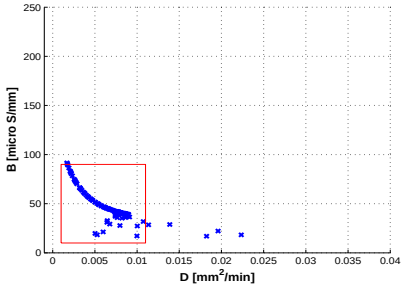

(b) Convergence after 2 iterations for MP_2.

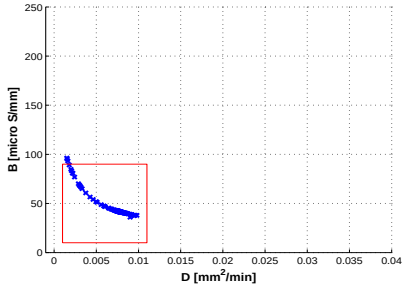

(c) Convergence after 10 iterations for MP_2.

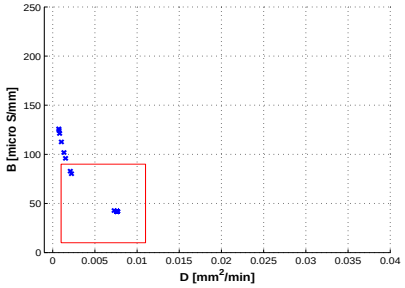

(d) Convergence after 40 iterations for MP_2.

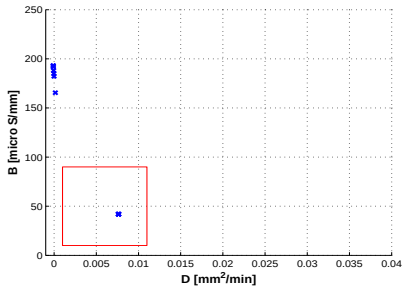

(e) Convergence after 120 iterations for MP_2.

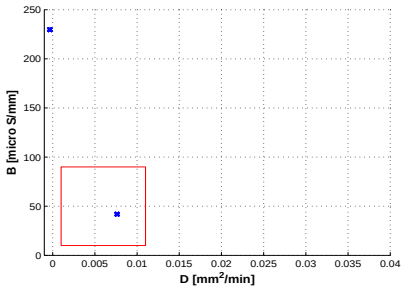

(f) Convergence after 500 iterations for MP_2.

Figure 5: Convergence between D [mm^2/min] and B [μS/mm] after six different iterations for sample MP_2 using range 3. The initial state borders are marked by the square.

greater effect when the concentration in the bone samples starting to get lower. In Table 3 all the obtained values from the Kalman filter can be found. The average value and the standard deviation of the bone samples become $D = 0.0110 \pm 0.0069$ mm^2/min. These values are derived using the final diffusion coefficient D for each sample.

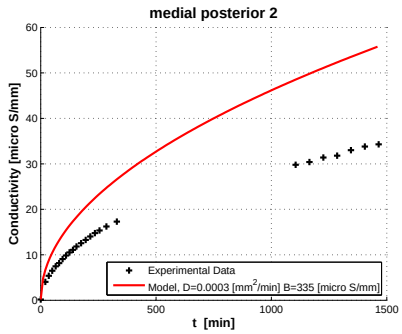

(a) Model vs exp. data for the first range in Table 2.

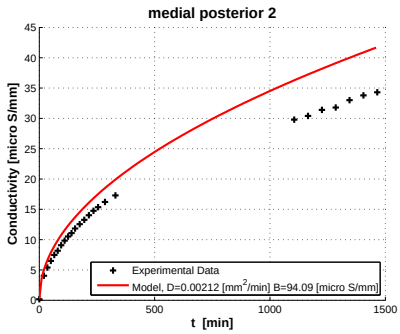

(b) Model vs exp. data for the second range in Table 2.

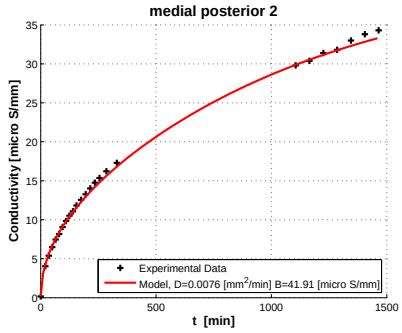

(c) Model vs exp. data for the third range in Table 2.

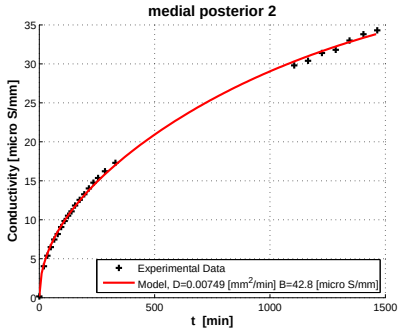

(d) Model vs exp. data for the fourth range in Table 2.

Figure 6: Kalman approximated conductivity versus data for the four different ranges in Table 2 for sample MP_2.

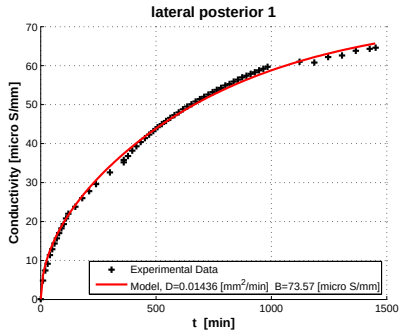

(a) Lateral posterior 1.

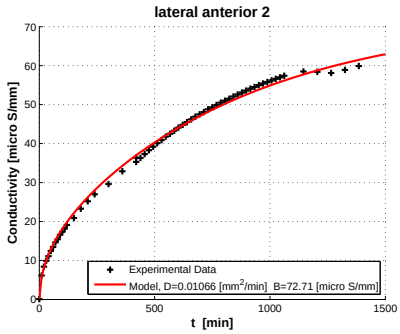

(b) Lateral anterior 2.

Figure 7: Experimental data and analytical function for samples from the lateral posterior (a) and anterior (b) side.

Table 3: Diffusion coefficient D, the constant B and σ_e for all series.

Sample	D [mm^2/min]	B [μS/mm]	σ_e [μS/mm]
MP1	0.001762	90.892	0.391
MP2	0.007491	42.805	0.298
MP3	0.006860	46.116	0.223
MP4	0.010631	42.551	0.332
MA1	0.020988	39.925	3.300
MA2	0.001666	57.780	0.476
MA3	0.001685	71.022	0.513
MA4	0.015418	23.181	0.323
LA1	0.011802	65.384	0.419
LA2	0.010660	72.713	0.983
LA3	0.008483	86.706	0.835
LA4	0.025767	73.503	1.127
LP1	0.014360	73.573	0.935
LP2	0.016701	61.779	0.862

Note: The two last samples from the lateral posterior side were tested for an alternative approach, but were excluded from the study.

6 Discussion

An experimental study determining the diffusion coefficient for KCl in bovine bone was performed using easily accessible equipment in form of a conductivity meter. The study was focused on the diffusion in radial direction, i.e. between the endosteum and the periosteum. The diffusion was described in mathematical terms using a Fourier series expansion and the diffusion coefficient was obtained from the experimental data using Kalman filtering. An average value and a standard deviation of D of the bone samples from the same animal can be computed from the values in Table 3 and become $D = 0.0110 \pm 0.0069$ mm^2/min. The distribution of the value of the diffusion coefficient for the samples is quite large. This can be explained through both bovine bone being an inhomogeneous material and limitations in the experimental method. The experiment includes several steps, as described in the Method section, which are executed as equally as possible for all samples. But each step is a possible source for differences between the samples. The solution was stirred before each measurement but still, the distribution of the KCl might not be homogeneous. This and any other noise introduced during the measurements such as temperature change or any inaccuracy of the instrument is captured by the Kalman filter. The standard deviation σ_e of the difference between the experimental data and the obtained approximated Kalman data for each sample, as defined in eq. (31), is included in Table 3. No significant difference between the different locations from which the bone samples were taken was achieved in the study.

The results could be compared to the findings of Patel et al. (2005). They used FRAP, Fluorescence Recovery After Photobleaching, to measure the diffusion coefficient in bovine bone. They found that the permeability of cortical bone differs extensively depending on what length scale and direction that is studied, having values for D in the longitudinal direction in the range of 94.20 ± 5.23 to $6.11 \cdot 10^{-6} \pm 2.37 \cdot 10^{-7}$ mm^2/min. The FRAP technique was also used by Wang et al. (2005). They measure the diffusion of fluorescein in cortical bone of mice and present a value of $D = 0.0198 \pm 0.0036$ mm^2/min, here using sodium fluorescein which has a molecular weight of 376 Da. In the study of Li et al. (2009), further results are presented using the FRAP technique. They report diffusion coefficients of five different exogenous fluorescence tracers in mice bone. Values range from $D = 0.0039 \pm 0.0013$ for Ovalbumin, 43 000 Da, to $D = 0.0177 \pm 0.0028$ mm^2/min for sodium fluorescein, 376 Da. It is also interesting to notice that they also have quite big standard deviations. The comparison should be done keeping in mind that the fluorescence tracers are much bigger molecules than KCl. The fluorescein tracers have a molecular weight from 376 to 43 000 Da compared to 74 Da for KCl. A summary of the here discussed studies is presented in Table 4. The assumption that 24 hours in the KCl solution was enough to make the bone samples saturated can be easily checked using the calculated diffusion coefficient inserted in eq. (12). Although eq. (12) must first be modified for three dimensions since all sides were open when the samples were in the KCl solution. If this is done the results show that the value in the middle of the samples is about 95% of the value of the boundaries after 24 hours. I.e. the samples were close to saturated. As earlier explained the end value of the conductivity will be the constant A, see eq. (21). The start value can be expressed as $A - B$. Since this study uses distilled water, the start value of the conductivity in each measurement is very low, close to zero. By that $A \approx B$, meaning that B can here be regarded to be the end value. As can

Table 4: Summary of comparable studies for femoral cortical bone.

Study	Species	Direction	Tracer [Da]	D [mm^2/min]
Patel et al. (2005)	Bovine	Transverse	300	4.2e-6±3.6e-7
Patel et al. (2005)	Bovine	Longitudinal	300	6.0e-6±1.2e-6
Wang et al. (2005)	Mice	Transverse	376	2.0e-2±3.6e-3
Li et al. (2009)	Mice	Transverse	376	1.8e-2±2.8e-3
Li et al. (2009)	Mice	Transverse	43 000	3.9e-3±1.3e-3
Current study	Bovine	Transverse	74	1.1e-2±6.9e-3

be seen in Table 3 the end value differs some from sample to sample. The reasons for this are several. One reason is that the volume of the samples differs a few per cent. In general a larger volume indicates a larger amount of KCl and hence a higher end value of conductivity. For some samples this was not the case. One explanation for this could be that the density over the bone might vary, indicating that more or less salt water could be trapped inside the bone samples.

It would be interesting to study samples of different sizes in future studies. A variation of the dimensions could reveal possible size effects, possible statistical variation, deviation of the assumed uniaxial flux and end effects that arise when the area of the open ends is small compared to the length in the direction of the flux.

Besides the 16 samples some measurements were performed for bone pieces that had not been in the KCl solution before going into the distilled water. After 24 hours the conductivity in the distilled water had reached about 5.5 μS/mm for these samples, i.e. about 7-13 % of the end values shown in Table 3. By that the diffusion coefficients calculated here cannot be said to be for purely KCl through bone tissue, but rather KCl mixed with a small part of bone substances moving through the bone tissue.

7 Conclusions

The idea of this study is that determination of diffusion coefficients and material constants in bone tissue will be more easily accessible. Since the calculated values of the diffusion coefficients are in line with other studies, as discussed in previous section, this method could be considered as an option for avoiding using more advanced and expensive equipment. Even so, the experiment should be further evaluated and developed. More test samples should be used and it would be interesting to use a mathematical model which considers the inhomogeneity of bone tissue.

Acknowledgements

The authors would like to acknowledge the anonymous reviewers and the editor of this journal. Further G. Lindberg, I. Svensson and W. Reheman would like to acknowledge the Swedish Research Council for funding this research. Likewise A. Shokry would like to thank the Erasmus Mundus Action 2 Project. A special thanks to Prof. Per Ståhle at the Division of Solid Mechanics, Lund University, for his valuable comments and insights.

Finally the authors would like to thank Ekerödsrasten, Hörby, Sweden for their donations of bovine bone.

References

Bali R., Shukla, A.K. (2000) 'Rheological Effects of Synovial Fluid on Nutritional Transport', *Tribology Letters*, 9(3-4):233-9.

Banks-Sills, L. Ståhle, P. Svensson, I. Eliaz, N. (2011) 'Strain driven transport for bone modelling at the periosteal surface', *Mathematical Bioscience*, 230(1):37-44.

Brown, R.G. (1983) '*Introduction to Random Signal Analysis and Kalman Filtering*', Wiley, New York.

Burstein, D., Gray, M.L., Hartman, A.L., Gipe, R., Foy, B.D. (1993) 'Diffusion of Small Solutes in Cartilage as Measured by Nuclear Magnetic Resonance (NMR) Spectroscopy and Imaging', *Journal of Orthopaedic Research.*, 11(4):465-78.

Cardoso, L., Fritton, S.P., Gailani, G., Benalla, M., Cowin, S.C. (2013) 'Advances in assessment of bone porosity, permeability and interstitial fluid flow', *Journal of Biomechanics*, 46(2):253-65.

Crank, J. (1975) '*The Mathematics of Diffusion*', Oxford University Press Inc, Oxford.

Down, R.D., Lehr, J.H. (2005) 'Environmental Instrumentation and Analysis Handbook' [online], Wiley, Hoboken New Jersey. http://eu.wiley.com/WileyCDA/WileyTitle/productCd-0471473324,descCd-ebook.html (Accessed 05 August 2013).

Fan, X., Roy, E., Zhu, L., Murphy, T.C., Ackert-Bicknell, C., Hart, C.M., Rosen, C., Nanes, M.S., Rubin, J. (2004) 'Nitric oxide regulates receptor activator of nuclear factor -κB ligand and osteoprotegerin expression in bone marrow stromal cells', *Endocrinology*, 145(2):751-9.

Fernandez-Seara, M.A., Wehrli, S.L., Wehrli, F.W. (2002) 'Diffusion of Exchangeable Water in Cortical Bone Studied by Nuclear Magnetic Resonance', *Biophysical Journal*, 82(1):522-9.

Fritton, S.P., Weinbaum, S. (2009) 'Fluid and Solute Transport in Bone: Flow-Induced Mechanotransduction', *Annual Reviews Fluid Mechanics*, 41(1):347–74.

Glicksman, G.E. (2000) '*Diffusion in Solids*', Wiley, New York.

Jee, W.S.S., Mori, S., Li, X.J., Chan, S., (1990) 'Prostaglandin E2 enhances cortical bone mass and activates intracortical bone remodelling in intact and ovariectomized female rats', *Bone*, 11(4):253-66.

Kalman, R.E. (1960) 'A New Approach to Linear Filtering and Prediction Problems', *Journal of Basic Engineering.*, 82(4):35-45.

Kealey, S.M., Aho, T., Delong, D., Barboriak, D.P., Provenzale, J.M., Eastwood, J.D. (2005) ' Assessment of Apparent Diffusion Coefficient in Normal and Degenerated Intervertebral Lumbar Disks: Initial Experience', *Radiology*, 235(2):569-74.

Knothe Tate, M.L., Steck, R., Forwood, M.R., Niederer, P. (2000) 'In vivo demonstration of load-induced fluid flow in the rat tibia and its potential implications for processes associated with functional adaptation', *Journal of Experimental Biology*, 203(18):2737–45.

Kufahl, R.H., Saha, S. (1990) 'A theoretical Model for Stress-generated Fluid Flow in the Canaliculi-lacunae Net Work in Bone Tissue', *Journal of Biomechanics*, 23(2):171-80.

Li, W., You, L., Schaffler, M.B., Wang L., (2009) 'The dependency of solute diffusion on molecular weight and shape in intact bone', *Bone*, 45(5):1017-23.

Lindberg, G., Banks-Sills, L., Ståhle, P., Svensson, I. (2013) 'A Two-Dimensional Model for Stress Driven Diffusion in Bone Tissue', *Computer Methods in Biomechanics and Biomedical Engineering*, [online] http://dx.doi.org/10.1080/10255842.2013.807507

Lindberg, G., Ståhle, P., Svensson, I. (2013) *A Perturbation Analysis of Non-Linear Diffusion from a Permeable Solid into a Finite Volume Containing a Liquid*, Division of Solid Mechanics, Lund University, Sweden, LUTFD2/(TFHF-3088)/1-8/(2013).

Maroudas, A. (1979) 'Physicochemical Properties of Articular Cartilage', In: *Adult Articular Cartilage*, pp.215–290. Edited by MAR Freeman. Pitman Medical, London.

Maroudas, A., Schneiderman, R., Popper, O. (1992) 'The Role of Water, Proteoglycan, and Collagen in Solute Transport in Cartilage', In: *Articular Cartilage and Osteoarthritis*, pp.355–372. Edited by Kuettner, K.E., Schleyerbach, R., Peyron, J.G.,and Hascall, V.C., Raven Press, New York.

Patel, R.B., O'Leary, J.M., Bhatt, S.J., Vasanja, A., Knothe Tate, M.L. (2005) 'Determining the permeablility of cortical bone at multiple length scales using fluorescence recovery after photobleaching techniques', *Proceedings of the 51st Annual Meeting of the Orthopaedic Research Society*, Washington D.C.

Sigmund, E.E., Cho, H., Chen, P., Byrnes, S., Song, Y.Q., Guo, X.E., Brown, T.R. (2008) 'Diffusion-Based MR Methods for Bone Structure and Evolution', *Magnetic Resonance in Medicine*, 59(1):28-39.

Tandon, P.N., Agarwal, R. (1989) 'A Study on Nutritional Transport in a Synovial Joint', *Computers & Mathematics with Applications*, 17(7):1131-41.

Wang, L., Han, Y., Henderson, S.C., Majeska, R.J., Weinbaum, S., Schaffler, M.B., (2005) 'In situ measurement of solute transport in the bone lacunar-canalicular system', *PNAS.*, 102(33):11911-6.

Weinbaum, S., Cowin, S.C., Zeng, Y. (1994) 'A model for the excitation of osteocytes by mechanical loading-induced bone fluid shear stresses', *Journal of Biomechanics*, 27(3):339–60.

Paper D

A Superposition Procedure for Calculation of Effective Diffusion and Elastic Parameters of Sparsely Porous Materials.

Abdallah Shokry, Gustav Lindberg, Ghias Kharmanda and Per Ståhle

Transport in Porous Media

2017 118(3):472-94

https://doi.org/10.1007/S11242-017-0866-4 (2017)

A superposition procedure for calculation of effective diffusion and elastic parameters of sparsely porous materials

Abdallah Shokry[a,b], Gustav Lindberg[a], Ghias Kharmanda[a] and Per Sthåle[a]

[a]Division of Solid Mechanics, Lund University
SE-221 00 Lund, Sweden
[b]Industrial Engineering Department, Fayoum University
63514 Fayoum, Egypt

Abstract

Effective material parameters for diffusion and elastic deformation are calculated for porous materials using a continuum theory based superposition procedure. The theory that is limited to two-dimensional cases, requires that the pores are sufficiently sparse. The method leads to simple manual calculations that can be performed by e.g. hospital staff for clinical diagnoses of bone deceases that involve increasing levels of porosity. An advantage is that the result relates to the bone material permeability and stiffness instead of merely pore densities. The procedure uses precalculated pore shape factors and exact size scaling. The remaining calculations do not require any knowledge of the underlying field methods that are used to compute the shape factors. The paper establishes the upper limit for the pore densities that are sufficiently sparse. A cross-section of bovine bone is taken as an example. The superposition procedure is evaluated against a full scale finite element calculation. The study compares the pore induced change of the diffusion coefficient and elastic modulus. The predictions differ between superposition and full scale calculations with 0.3 percentage points when pore contribution to the diffusion constant is 3 to 7%, and 0.7 percentage points when the pore contribution to the modulus of elasticity is 4.5 to 5%. It is uncertain if the error is in the superposition method, which is exact for small pore densities while the full scale finite model is not.

Keywords: *porous materials; mechanical; stiffness; diffusion coefficient; superposition principle*

1 Introduction

Bone is a complex material, with a multiphase, heterogeneous and anisotropic microstructure. One of the main goals of this work is to define the relationship between bone porosity and both diffusion coefficient and elastic modulus. The reason for calculating the material parameters is that they are difficult to obtain experimentally or clinically. Further, the state of the diffusion coefficient and the modulus of elasticity may be used as a tool for clinical diagnosis. The porosity of bone can vary continuously from 2 to 95%, and it is usually distinguished between trabecular bone with 40-95% porosity and cortical bone with 2-20% porosity (Winkelstein, 2012).

The porosity affects the diffusivity and the elastic modulus of the material. The diffusivity is important for maintaining a proper supply of nutrients and for removing waste products, while the elastic modulus determines the quality and the reliability of bone strength. Some useful models have been proposed for studies of the properties of bone tissues in the presence of pores. These are based on the poroelastic theory, in which the mechanical properties of a material are affected by the movement of the fluid in the pores (Biot, 1941; Rice and Cleary, 1976; Showalter, 2000; Cowin, 2003). In bone tissue, the transport of fluids and solutes is a concern for the bone formation and remodelling. The diffusion coefficients of different solutes in cortical bone of mammals were investigated using different techniques (Patel et al., 2004; Wang et al., 2005; Li et al., 2009; Lindberg et al., 2014). Further, the diffusion coefficients of water in trabecular bone tissue for humans were studied by Marinozzi, Bibi and Marinozzi (2014b) and Marinozzi et al. (2014a). The result was needed to understand the transportation process of substances on the cell level, and to make realistic models for bone remodelling and bone healing.

It has been shown by Marinozzi, Bibi and Marinozzi (2013) that hygroscopic driving forces lead to significant swelling of bone. The deformation compatibility that generally restricts the swelling introduces both compressive and tensile residual stresses in different parts of the bone. The stresses that counteracts the swelling, depend on the stiffness of the bone. It is therefore, of interest also to estimate the elastic modulus and how it is affected by the pore sizes and densities.

The mechanical properties such as elastic modulus of bone are affected by the pore sizes and densities. To investigate the interrelationships between the pore size and the bone strength, several experiments are required. The relationship between the pore size and the elastic modulus may be established analytically or experimentally. The elastic modulus decreases as the pore size increases as is obtained by Schaffler and Burr (1988) and Grimal et al. (2011). In Helsing and Jonsson (2002) and Helsing (2011) numerical models with the capability to compute mechanical properties of porous media containing many pores are given. The methods give accurate results without any limitations regarding pore density and shape. Also sharp corners that produce stress singularities are effectively treated.

One dimensional models (Redwood, Rall and Perl, 1974; Ochoa-Tapia, Stroeve and Whitaker, 1994) are developed with the ambition to simplify the calculations. Two or three dimensional field calculations are avoided altogether. In these models the diffusion coefficient is supposed to be different in one or several subregions and the result is calculated as a series of one dimensional subregions. References to pores with real shapes are absent apart from cylindrical/spherical pores which means that the applicability is

limited to nearly cylidrical/spherical pores or a wider range of shapes but randomly oriented. The assumption is based on earlier results (Perrins, McKenzie and McPhedran, 1979) that concern pores with random orientation. Pores in mammal bones are often irregular and not seldom crack like which affect the diffusion and the stiffness. In human long bones the pores are often shorter in the radial direction which seriously increase the apparent diffusion coefficient and modulus of elasticity.

The use of CT-scanning of human tissues in vivo is rapidly increasing. Frequently bone is scanned to discover increased porosities. The estimation of the porosity is used for diagnoses of osteoporosis and related illnesses. It is also used to keep track of the development of diseases. However, diagnoses based relevant parameters such as chemical permeability and stiffness should be better than simply total pore area which is used today. Moreover, the analysis can still be simple and without requiring advanced field calculations on case level. In the proposed model only a small set of individual pores are pre-computed and is then used as references together with an exact size scaling. To this end different reference sets could be used for, e.g., female human long bones, male ditto, sets for other mammals, etc.

The present study demonstrates a simple but asymptotically exact procedure to calculate the diffusion coefficient and the elastic modulus of a material with sparse irregular pores by using superposition of known contributions to the diffusion coefficient and the modulus of elasticity. A geometry dependent correction factor is obtained for a few pore shapes along with a proper pore size scaling. The factor is based on a single finite element calculation of the local diffusive and elastic properties of a region surrounding the pore. The orientation of the pore is included as a model parameter. The method is demonstrated using a porous bovine bone sample with irregularly distributed pores. The method does not require specific knowledge of the continuum field treatment of diffusion or mechanics. However, a few pre-calculated parameters for some characteristic shapes needs to be done. The result is compared with a full scale calculation of the same sample.

2 Theory

2.1 Diffusion

Consider a body containing a single pore. The material surrounding the pore is called the matrix. In the pore, the diffusion coefficient is set to D_p and in the matrix the diffusion coefficient is set to D_m. A two-dimensional flow of matter that is driven by the concentration gradient is considered. The flow rate per unit of area, also called flux is denoted J_i, where the index denotes the direction in Cartesian coordinates $x_i \equiv \{x_1, x_2, x_3\}$. Tensor notation including the summation rule is applied. The indices i, j assume the values 1 and 2. The flux vector J_i of a selected substance becomes, due to differences in concentration of matter,

$$J_i = -D\frac{\partial c}{\partial x_i}\,, \tag{1}$$

where c is the concentration of the flowing matter. The material parameter D is the diffusion coefficient of the substance-matrix system. Further, matter is conserved giving

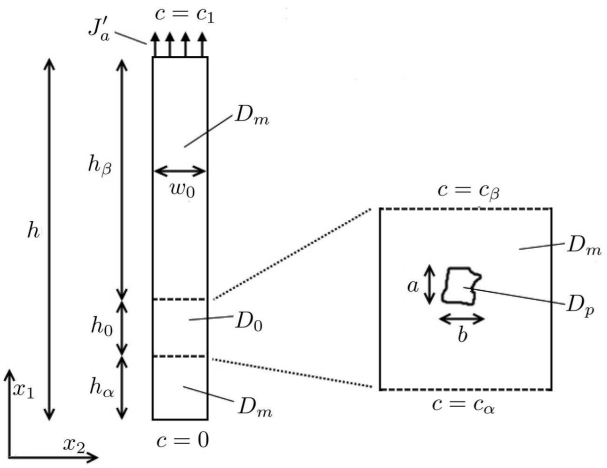

Figure 1: A thin section containing an area $h_0 \times w_0$ with a pore. The average diffusion coefficient in the $h_0 \times w_0$ rectangular region is D_0.

that

$$\frac{\partial c}{\partial t} = -\frac{\partial J_i}{\partial x_i} \,. \tag{2}$$

In the present study steady-state solutions, i.e., $\partial c/\partial t = 0$ are sought. The consequence is that the flux will be divergence free, i.e.

$$\frac{\partial}{\partial x_i}\left(D\frac{\partial c}{\partial x_i}\right) = 0 \,. \tag{3}$$

The governing eq. (3) is solved for the boundary conditions

$$\frac{\partial c}{\partial x_2} = 0 \qquad \text{at } 0 < x_1 < h \text{ for } x_2 = 0 \text{ and } x_2 = w_0 \,. \tag{4}$$

Further,

$$c = 0 \qquad \text{at } x_1 = 0 \;\text{ for }\; 0 \le x_2 \le w_0 \,, \tag{5}$$

and

$$c = c_1 \qquad \text{at } x_1 = h \;\text{ for }\; 0 \le x_2 \le w_0 \,. \tag{6}$$

At first, a thin strip of the structure is examined, see Figure 1. The strip contains a small inserted section with the height h_0 and the width w_0, where a pore, or something else that affects the effective diffusion coefficient, is located. In this small section, the effective diffusion coefficient is set to D_0. The diffusion is assumed to be uniaxial along the boundaries of the section. The relation between D_0 and the diffusion coefficients for the matrix, D_m, and for the pore, D_p, and the influence of size and shape of the pore will be dealt with later in this section.

The effective diffusion coefficient D_1 for the strip is derived in the following. The total flux J'_a, see Figure 1, through every cross-section in the strip remains constant. Therefore according to eq. (1)

$$D_1\frac{c_1}{h} = D_m\frac{c_1 - c_\beta}{h_\beta} = D_0\frac{c_\beta - c_\alpha}{h_0} = D_m\frac{c_\alpha}{h_a} \,, \tag{7}$$

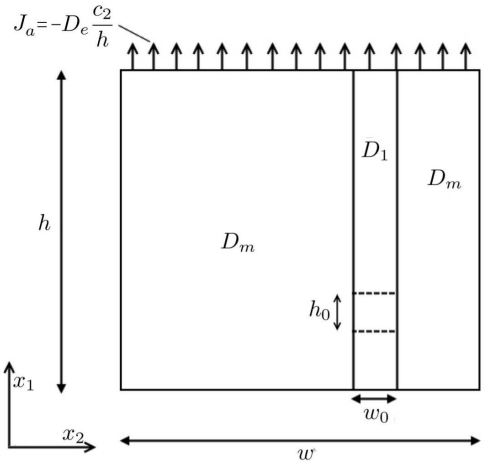

Figure 2: The geometry from Figure 1 embedded in a larger section.

applies. The concentrations c_α and c_β are the concentrations on each side of the insert section as can be seen in Figure 1. By using that $h = h_\beta + h_0 + h_\alpha$, some algebra gives

$$D_1 = D_m \left(1 - \left(1 - \frac{D_m}{D_0}\right)\frac{h_0}{h}\right)^{-1} . \tag{8}$$

Now a wider structure, where the strip is being an insert, is considered, see Figure 2. By introducing an effective diffusion coefficient D_e for the entire structure, the average flow through the entire structure is described as

$$J_a = -D_e \frac{c_2}{h} . \tag{9}$$

Uniaxial flow is again assumed for along the boundaries of the strip with the width w_0. The requirement is again that the pore should be sufficiently small for this to be an acceptable assumption. According to Figure 2 it is then obvious that the total amount of matter that passes a cross-section of the structure is

$$J_a w = -D_1 \frac{c_2}{h} w_0 - D_m \frac{c_2}{h}(w - w_0) , \tag{10}$$

where the first term on the right hand side represents the flux through a cross-section of the inserted strip with the width w_0. The second term is the remaining part of the total flux through matrix material. If eq. (8) is used to express D_1 in given quantities and Eqs. (9) and (10) are used to eliminate J_a and c_2, then the effective diffusion coefficient is obtained as

$$D_e = D_m \left(1 + \frac{1 - D_m/D_0}{1 - (1 - D_m/D_0)\frac{h_0}{h}} \frac{h_0 w_0}{hw}\right) . \tag{11}$$

The derived scaling $h_0 w_0/hw$ relates the rectangular area, $h_0 w_0$, to the area of the full body, hw. The quantities defining D_e are the height ratio h_0/h, the area ratio $h_0 w_0/hw$ and the ratio of the diffusivity coefficients, D_m/D_0.

Since the derivation leading to eq. (11) did not explicitly utilise the shape of the region $h_0 \times w_0$ it is here assumed that the result eq. (11) can be used also for pores of general shape. Therefore, the diffusivity inside the pores is given by the diffusion coefficient, D_p. Further, the quantity $h_0 w_0$ in eq. (11) is replaced with θA_p, where A_p is the pore area in the $x_1 - x_2$ plane, and θ is a geometrical factor that apart from shape and size of the pore also depends on the orientation of the pore with respect to the nominal flow direction. Finally, the relative height h_0/h in eq. (11) is replaced with $\sqrt{A_p/hw}$, and a shape correction factor κ. As a consequence, the following two relations replace eq. (11), and D_e is written

$$D_e = D_m \left(1 + \frac{\theta s}{1 - \kappa s \sqrt{\frac{A_p}{hw}}} \, \frac{A_p}{hw} \right) , \tag{12}$$

where the relation between D_m and D_p for convenience is represented by the quantity

$$s = 1 - \frac{D_m}{D_p} \, . \tag{13}$$

The values θ and κ, must be established. In order to do so eq. (12) is expanded as a power series of $\sqrt{A_p/hw}$ as

$$(\frac{D_e}{D_m} - 1)\frac{hw}{sA_p} = \theta \left[1 + \kappa s \sqrt{\frac{A_p}{hw}} + (\kappa s)^2 O\left(\frac{A_p}{hw} \right) \right] \, . \tag{14}$$

Finite element calculations for the current pore shape are done for different pore sizes A_p, as described in Sect. 3. By studying the flux it is now possible to determine θ and κ from the two leading terms of the right hand side of eq. (14). The parameters are obtained through least square fit. The determination of θ and κ is done for a range of pore sizes and the limiting values for vanishing pore sizes are sought. The procedure is performed for relevant pore shapes and orientations relative to the direction of the flux.

The effective diffusion coefficient D_e of the entire structure is defined as

$$D_e = -J_a \frac{h}{c_o}, \tag{15}$$

where c_o is the prescribed concentration at $x_1 = h$ and J_a is the average flux through the body calculated as

$$J_a = \frac{1}{w} \int_0^w J_1 \mathrm{d}x_2 \text{ at } x_1 = h \, , \tag{16}$$

where J_1 is the flux in the x_1-direction, cf. eq. (1). The effective diffusivity coefficient D_e can be calculated for bodies with large geometries and multiple pores. It is obvious from the analysis above that as long as the individual pores do not interact, the result is found using superposition of the individual contributions from each pore. This is supposed to be possible if the pores are sufficiently small as compared with the distance between the pores. The following is used,

$$D_e = D_m \left(1 + \frac{s}{hw} \sum_{i=1}^{N} \frac{\tilde{\theta}^{(i)} A_p^{(i)}}{1 - s\kappa^{(i)} \sqrt{\frac{A_p^{(i)}}{hw}}} \right) , \tag{17}$$

where summation is performed for N pores. The geometry factors $\tilde{\theta}^{(i)}$ and $\kappa^{(i)}$ are chosen as the result of θ and κ for sufficiently small pore sizes and are selected as the one of a limited set of representative pores. By studying the pores in a region of the material specimen which is believed to be representative for the total specimen, and follow the procedure just described, the total D_e for the specimen can be established using eq. (17).

2.2 Elastic theory

In this section, a method to compute how present pores influence the elastic modulus is presented. The same geometries and pores as above, are assumed. To follow the conventional tensor notation, the stresses are written σ_{ij}, the strains ϵ_{ij} and the displacements u_i. The stresses are given by Hooke's law as

$$\sigma_{ij} = \frac{E}{1+\nu}(\epsilon_{ij} + \frac{\nu}{(1-2\nu)}\delta_{ij}\epsilon_{kk}) \tag{18}$$

and the strains ϵ_{ij}, which are assumed to be small, are defined by

$$\epsilon_{ij} = \frac{1}{2}(u_{i,j} + u_{j,i})\,. \tag{19}$$

The equations of equilibrium, $\sigma_{ij,j} = 0$, after insertion of Eqs. (18) and (19) give the equation

$$u_{i,jj} + \frac{1}{1-2\nu}u_{j,ij} = 0. \tag{20}$$

Eq. (20) governs the linear elastic behaviour of the body. For stretching in the x_1-direction the boundary conditions are

$$u_1 = 0 \quad \text{at} \quad 0 \leq x_2 \leq w \quad \text{for} \quad x_1 = 0 \tag{21}$$

and

$$u_1 = \delta \quad \text{at} \quad 0 \leq x_2 \leq w \quad \text{for} \quad x_1 = h. \tag{22}$$

Normal tractions on the remaining edges $x_2 = 0$, $0 < x_1 < h$ and $x_2 = w$, $0 < x_1 < h$ vanish. Finally, shear tractions on all edges vanish.

The average tractions at $x_1 = h$ are calculated as

$$\sigma_a = \frac{1}{w}\int_0^w \sigma_{11}\mathrm{d}x_2. \tag{23}$$

The effective modulus of elasticity is defined as

$$E_e = \sigma_a \frac{h}{\delta}\,. \tag{24}$$

The presence of pores will weaken the structure, whereas the stiffness of the pore material, being a fluid, is assumed to be insignificant. It seems reasonable that the weakening may be ignored at large distance from the pore. It is also assumed that the linear extent of this region scale with the width of the pore b perpendicular to the loading direction. As for the diffusion case the change of the modulus of elasticity is assumed to be proportional

to the area of the pore. To make it possible to include a crack, the square of the linear extent in the direction perpendicular to the nominal loading direction versus the body area is selected as the scaling parameter. The assumption is verified for a crack and a circular pore, see APPENDIX. In the same way as for the diffusion theory a geometry factor θ_E is included for the influence of other geometrical details of the pore apart from the width b. This leads to the first order approximation

$$E_e = E_m\left(1 - \theta_E \frac{b^2}{hw}\right) \tag{25}$$

for loading in the x_1-direction. To obtain the geometry factor θ_E, numerical values of E_e for single pore geometries for different pore sizes are calculated using the finite element method. A power expansion for small pores gives the expression

$$(\frac{E_e}{E_m} - 1)\frac{hw}{b^2} = \theta_E + O\left(\frac{b^2}{hw}\right), \tag{26}$$

where E_m is the modulus of elasticity of the matrix material. The value θ_E is fitted to the numerical result of E_e for different pore shapes and orientations and by taking vanishing pore size result. Details are given in Sect. 3.

For a large body with multiple pores, the effective modulus of elasticity, E_e, may be calculated using the same superposition principle as for the diffusion case, cf. eq.(17). The calculation is performed as

$$E_e = E_m\left(1 - \frac{1}{hw}\sum_{i=1}^{N} \tilde{\theta}_E^{(i)} \left(b^{(i)}\right)^2\right), \tag{27}$$

where the summation is performed for N pores. The geometry factors $\tilde{\theta}_E^{(i)}$ are chosen for sufficiently small pores and for a corresponding shape.

By studying the pores in a region of the material specimen that is believed to be representative for the total specimen, if necessary by using statistics, and following the procedure just described, the total E_e for the specimen can be established employing eq. (27).

3 Numerical analysis

The scanned bone images are transferred to a mesh that is used for finite element calculations. This is done i two steps. First a CAD program is used to create an intermediate object mesh that describes the cross section of the bone sample (see an example in Figure 3). Smaller sections of the object mesh, each containing a pore, are then transferred to the finite element program ABAQUS (ABAQUS User's manual 6.14, 2014) and covered by isoparametric elements in a pre-processor. ABAQUS offers the possibility to compute elastic deformation and steady-state diffusion. Eq. (3) is the governing equation for diffusion and eq. (20) is the governing equation for deformation. The boundary value problem is solved for the region $0 \leq x_1 \leq h$ and $0 \leq x_2 \leq w$ using a free mesh composed of trilateral 6-node and quadrilateral 8-node isoparametric elements. Full integration is

a) 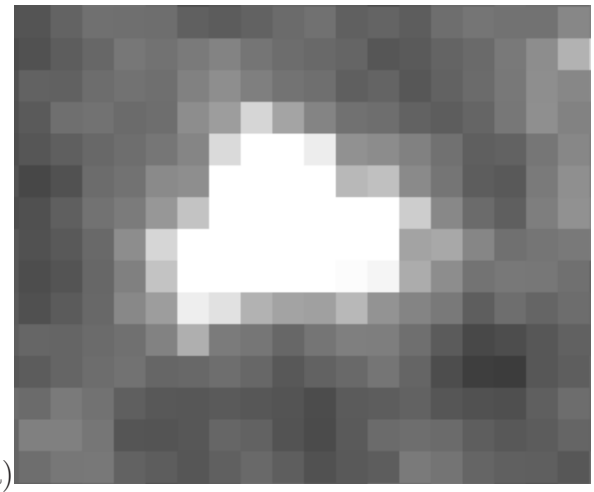 b) 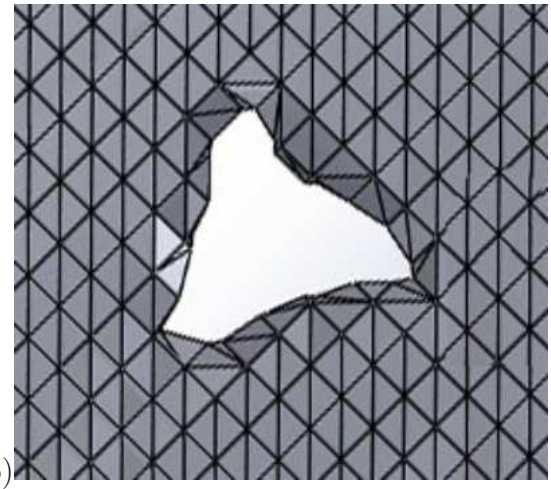

Figure 3: a) An original image of a typical pore with a linear extent of around 35μm. The linear extent of the cubic voxels is 4.2 μm. b) Shows the geometry as a prepared object mesh using a 50% grayscale threshold. The object mesh is in a last step transformed into a mesh of 6-node and 8-node isoparametric elements.

used. For each type of pore geometry, same element mesh is used for both the diffusion and the deformation problem. A representative case is shown in Figure 4.

The ratio of the linear extent of adjacent elements is never more than 2 and normally around 1.2. The meshes for the different pore geometries are built up of eight to ten thousand nodes and two to three thousand six-node and eight-node isoparametric plane elements.

4 Establishing Material Parameters

The procedure is evaluated using a sample of bovine ulna. A single CT scan image of the bone sample is used, see Figure 5. The image is produced by Ståhle, Persson and Isaksson (2013). The original image is a 10×10 mm^2 cross section of an around $10 \times 10 \times 30$ mm^3 bone specimen from a bovine ulna. It shows traces of multiple cracks that almost inevitably occur in bone samples as soon as they are exposed to air. The x_1-axis goes from the endosteum (i.e. the inner surface of the bone, facing towards the bone marrow) in the radial direction out to the periosteum (i.e. the outer surface of the bone). The x_2-axis is along the tangential direction of the bone cross-section. The longitudinal direction along the ulna is perpendicular to the plane of the image in Figure 4.

The four pores marked A to D are assumed to be a fair representation of the various shapes that are present in the segment of the bone cross-section, cf. Figure 5a. Images showing the geometrical details of the selected pores are shown in Figure 5b. By rotating the pores 90° an additional set of pores A' to D' are obtained. Apparent values of θ, κ and θ_E are obtained for small pore sizes. Convergent values for the set of parameters were obtained in all cases.

The height of the pores, a, is along the direction of the nominal flux or load, and the

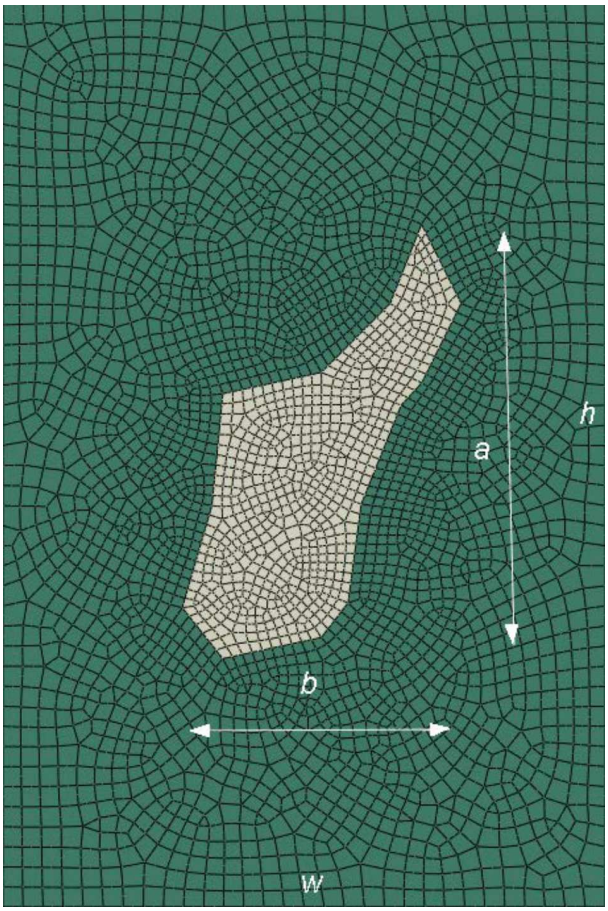

Figure 4: A typical mesh. Here for pore C' and with $h/a = w/b = 2$. The pore is the central grey area. In the original image the pore covers 6×9 pixels. The meshed area $hw = 97 \times 57 \mu\text{m}^2$.

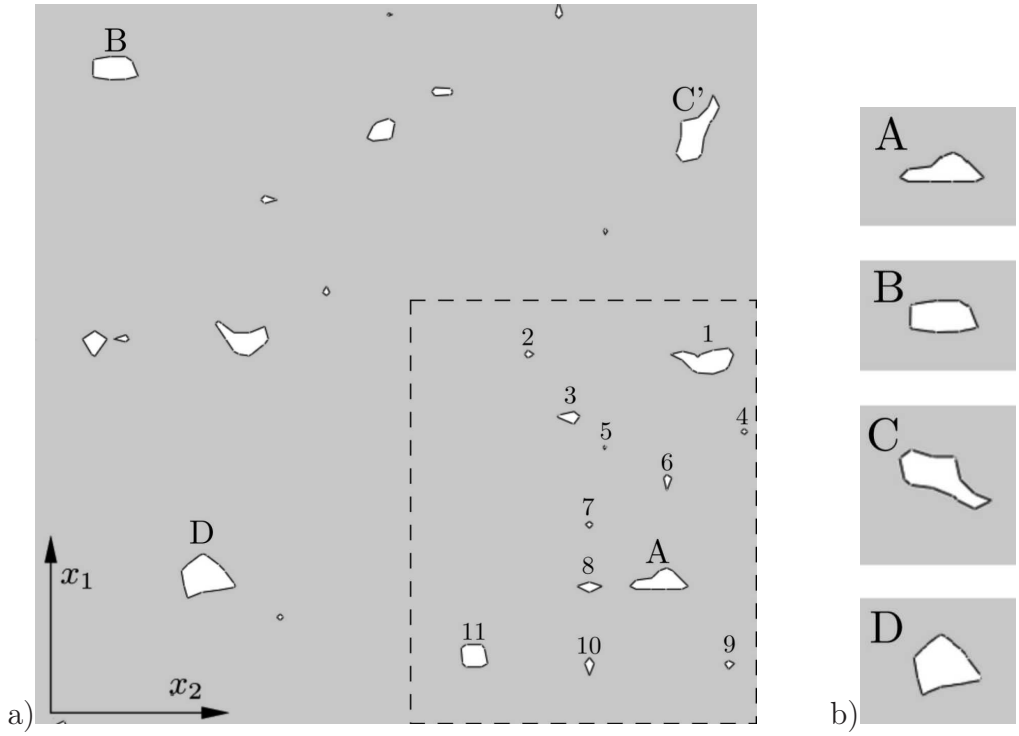

Figure 5: a) A $0.22 \times 0.20\,\mathrm{mm}^2$ part of a $10 \times 10\,\mathrm{mm}^2$ bovine ulna sample (Ståhle, Persson and Isaksson, 2013). A 50% grayscale threshold has been used (cf. Figs. 4a and b). The pores A, B, C, and D are used as reference cases. Evaluation is then performed on the region with numbered pores in the lower right corner of the image marked with dashed edges. b) detailed view of the selected pores.

Table 1: Data for the pores A to D and their counterparts A' to D' that are rotated 90°. Length scale is in units of pixel size.

Case	A	B	C	D	D'	C'	B'	A'
a	3	3	6	6	7	9	6	8
b	8	6	9	7	6	6	3	3
a/b	0.38	0.50	0.67	0.85	1.17	1.50	2.00	2.67
A_p	12	15	21	24	24	21	15	12

width, b, is perpendicular to that. The ratio a/b is from 0.38 for pore A to 2.67 for pore A', see Table 1. The unit of length is a pixel, that is 4.2μm. The voxel depth is also a unit making a cubic shape with the length of each side of 4.2μm.

4.1 Diffusion coefficient results

The content of the pores is assumed to have diffusive and mechanical properties similar to water. Diffusion coefficients of a large number of substances in water are listed in the book Cussler (1997). With only a few exceptions the diffusion coefficients are in the range $1\cdot 10^{-9}$ to $3\cdot 10^{-9}$ m^2/s and the diffusion coefficient in the pore is here taken to be $D_p = 2\cdot 10^{-9}$ m^2/s. Patel et al. (2004) studied diffusion of different molecules in bovine bone. They found that the diffusivity varied considerably when measured on tissue level, cellular syncytium level and matrix microporosity level. On the matrix microporosity level the diffusion coefficient was found to be close to $1\cdot 10^{-13}$ m^2/s for a molecule mass of 300 atomic mass units (u). Therefore, the calculations in the present study are performed for a ratio of the diffusion coefficient in water versus that in bone of $D_p/D_m = 2\cdot 10^4$.

The distribution of the normalised concentration inside the computed region is shown in Figure 6. The geometry corresponds to the one found in Figure 4. The pore C' is displayed as the dashed curve. The extent of the geometry is $h \times w$. The side ratio of the geometry is the same as the ratio of the pore size meaning that $a/b = h/w$. The extent of the area of the pore versus that of the geometry is $A_p/hw = 0.09$. One readily observes how the flux in the neighbourhood of the pore diverts from uniaxial flux and approaches the pore.

The colours represent constant concentration. The increased diffusion rate in the neighbourhood of the pore reveals itself as an increase of the distances between the colour contours. The flux direction is perpendicular to the concentration levels as indicated by the inserted arrows. The diffusion, which nominally flows in the x_1-direction, is observed to be diverted towards the pore. Obviously the increased diffusion rate also increases in a region surrounding the pore. Close to all four edges of the geometry, the diffusion is less affected by the presence of the pore. The affected region seems to be a few times the extent of the pore (see Figure 6).

The calculated normalised average flux, $J_a h/(D_m \Delta c)$, where Δc is the difference in concentration between $x_1 = 0$ and $x_1 = h$ for different flow directions and different pore sizes, is displayed in Figure 7. The nominal flux, i.e. the flux for $\sqrt{A_p/hw} = 0$ is $J_a h/(D_m \Delta c) = 1$. It is seen that the flux as expected increases with increasing pore sizes. As an example, when the area of the pore is 5% of the total area hw, i.e. $\sqrt{A_p/hw} \approx 0.2$,

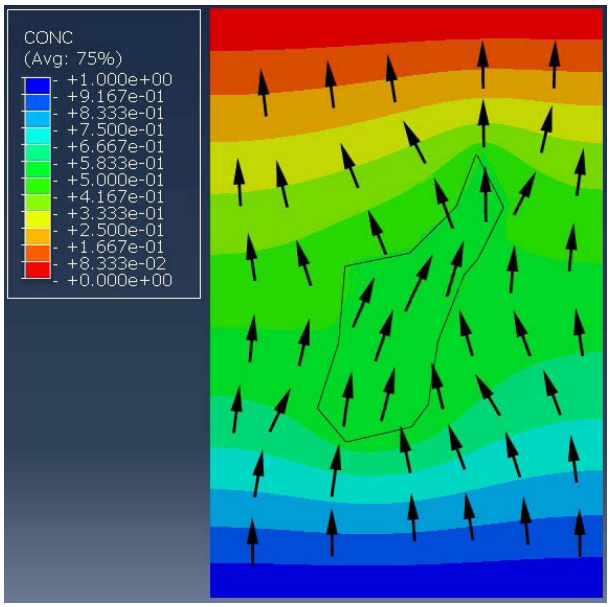

Figure 6: Distribution of the concentration. The nominal flux is vertical. The contour shows pore C' with an around 20 000 times larger diffusion constant than the surrounding bone.

the flux is in the region of around 5% to 8% larger than the nominal flux in the absence of a pore. When the area of the pore is 40% of the total area hw, the flux is as much as two times the nominal flux.

The interaction between the ratio of the pore size, in terms of the left hand side of eq. (14), versus the linear body size $\sqrt{A_p/hw}$ is shown in Figure 8. An interesting observation is that eq. (14) is practically constant for pores smaller than $\sqrt{A_p/hw} < 0.3$. The meaning is that the value for very small pores is applicable as long as the linear size of the pore is less than a third of the linear size of the body, or to be more precise, the calculated cell hw. For application purposes this would be replaced with the distance to the nearest pore.

To utilise this, the small pore value of the geometry factor θ is denoted $\tilde{\theta}$ and is defined as,

$$\tilde{\theta} = \lim_{\sqrt{\frac{A_p}{hw}} \to 0} \theta \,. \tag{28}$$

The limit value, $\tilde{\theta}$ is a pure shape factor and is independent of the relative size of the pore A_p/hw. To achieve reliable results, the numerical values for θ, which are vitiated with scatter, are least square fitted using the first four terms of a series expansion of θ as it is obtained for different pore sizes using eq. (14), as described in Sect. 2. A Matlab function that employs the least square fit is used to find the leading term. The obtained factors $\tilde{\theta}$, κ and $\tilde{\theta}_E$ are given in Table 2.

Figure 9 summarises the values of $\tilde{\theta}$ as a function of the pore aspect ratio a/b. The figure shows that $\tilde{\theta}$ increases with increasing a/b. The result from a series of six rectangular pores is included. The rectangular pores has a smaller scatter which indicates that

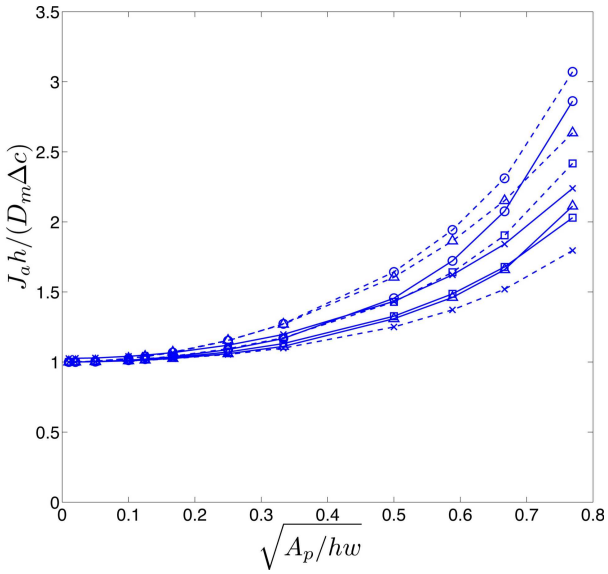

Figure 7: Normalised average flux $J_a h/(D_m \Delta c)$ for pores A (□) , B (○), C (△) and D (×) (solid lines) and A' to D' with corresponding markers and dashed lines, as a function of the pore size $\sqrt{A_p/hw}$.

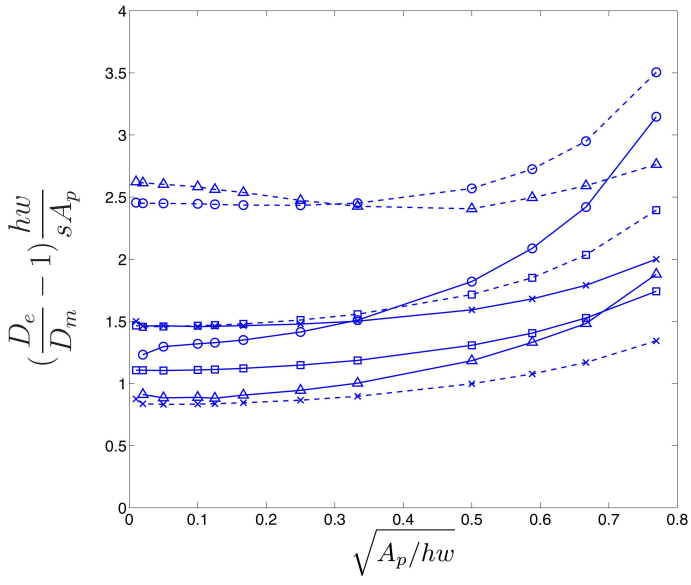

Figure 8: The left hand side of eq. (14) for pores A (□) , B (○), C (△) and D (×) (solid lines) and A' to D' with corresponding markers and dashed lines, as a function of the relative pore size $\sqrt{A_p/hw}$.

Table 2: $\tilde{\theta}$, κ, and $\tilde{\theta}_E$ values for the pores A to D and A' to D'.

Case	A	B	C	D	D'	C'	B'	A'
$\tilde{\theta}$	1.1	1.3	0.9	1.5	0.8	2.6	2.5	1.5
κ	-1.10	-0.05	-0.11	-0.11	-0.01	-0.16	-0.02	-0.09
$\tilde{\theta}_E$	2.0	1.9	1.7	1.2	2.4	3.3	3.4	1.9

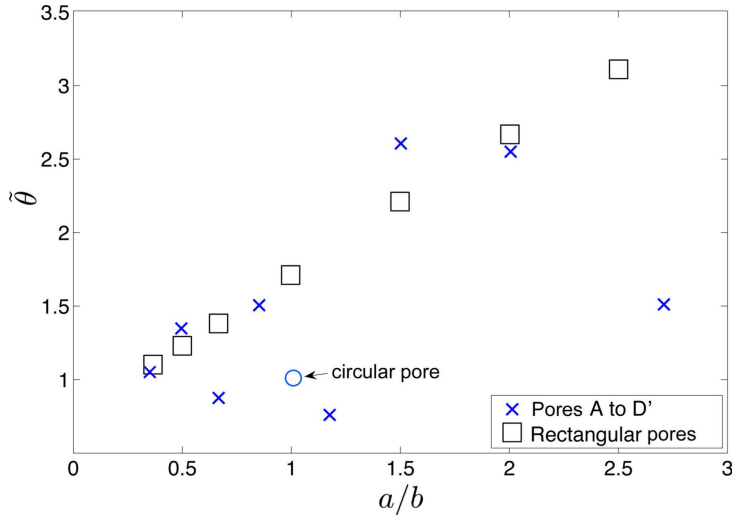

Figure 9: $\tilde{\theta}$ versus the shape ratio a/b for pores A to D and A' to D' ($\times$). $\tilde{\theta}$ for six rectangular pores with $a/b = 2.5, 2, 1.5, 1, 0.67, 0.5$ are also included ($\square$). The result for a circular pore is included (Ochoa-Tapia, Stroeve and Whitaker, 1994) .

there are more influential possibly mesh related details, regarding the shape than merely the aspect ratio.

4.2 Elastic modulus results

Calculation of the elastic modulus of a region containing a single pore is performed along the same lines as for the diffusion analysis. The modulus of elasticity of the matrix is E_m and Poisson's ratio is $\nu = 0.3$. The displacement difference of two opposed edges, separated by the distance h, is δ. Plane stress is assumed. The material in the pore is assumed to lack stiffness, meaning that the body is treated as a hollow section.

The distribution of the normalised largest principal stress $\sigma_1 h/E_m\delta$ for pore C', for which $a/b = 1.5$, is shown in Figure 10. The figure shows that stresses are high at two points on the edges of the pore. Here the stress is expected to be high but is probably overestimated because of the rather coarse mesh that is used in the vicinity of the pore. The pore geometry is obtained from the CT scanned bone sample as displayed in Figure 4. Due to the small dimensions of the pore of only 6×9 pixels the details of the pore are by necessity rather edgy. The shape is obtained from a 50% grayscale threshold and interpolation between the pixels. The process removes the original zig-zag contour but

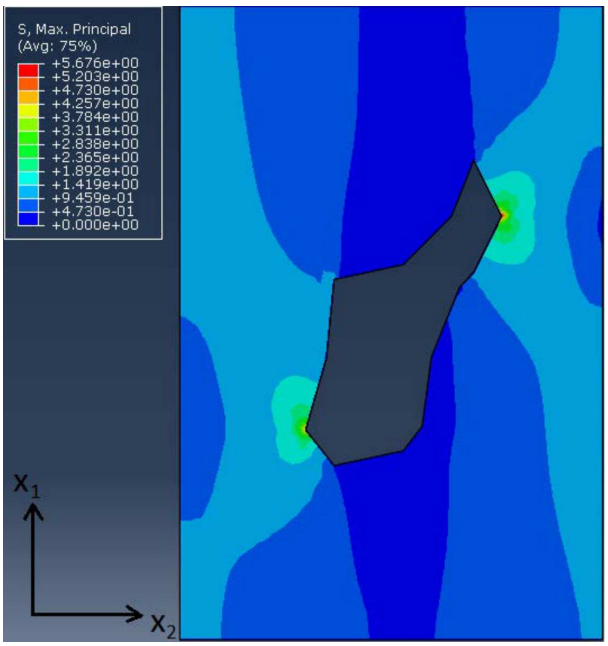

Figure 10: Distribution of the largest principal stress $\sigma_1 h/E_m \Delta u$ for pore C' with $a/b = 1.5$. The nominal loading is in the x_1-direction.

leaves some sharp corners (cf. Figure 3).

The stress distribution along the edges of the body is fairly homogeneous and close to the nominal value $\sigma_1 h/E_m \delta = 1$, which shows that the disturbance of the remote uniaxial stress field is more or less localised to a fairly small region around the pore.

The average stress, σ_e/σ_m, for different loading directions and different pore sizes is shown in Figure 11. The nominal stress is defined as $\sigma_m = E_m \delta/h$. The effective stress σ_e is obtained from the finite element calculations. As expected, the figure shows that the stress decreases as the pore size increases. For large pores ($b/\sqrt{hw} > 0.3$) the resulting stress decays approximately linearly with $b/\sqrt{hw}$. Obviously the stress should become zero at $b/h = 1$ when the entire body is transversed by the pore which decreases the stiffness to zero.

The shape factor $\tilde{\theta}_E$ is defining the influence of pores of infinitesimal size. As for the diffusion case the estimated value of the geometry factor is denoted θ_E. Following eq. (25) the definition is

$$\theta_E = \left(1 - \frac{E_e}{E_m}\right) \frac{hw}{b^2} \,. \tag{29}$$

The influence which the pore size has on the effective Young's modulus is shown in Figure 12, where the the left hand side of eq. (26) is plotted against b^2/hw. As shown in the figure, eq. (26) is dependent on the pore shape and size. Further, eq. (26) decreases as the pore size increases which is an expected consequence of the switch off behaviour of the pore size dependence described in the previous paragraph. The limiting value for small pores is

$$\tilde{\theta}_E = \lim_{\frac{b^2}{hw} \to 0} \theta_E \,. \tag{30}$$

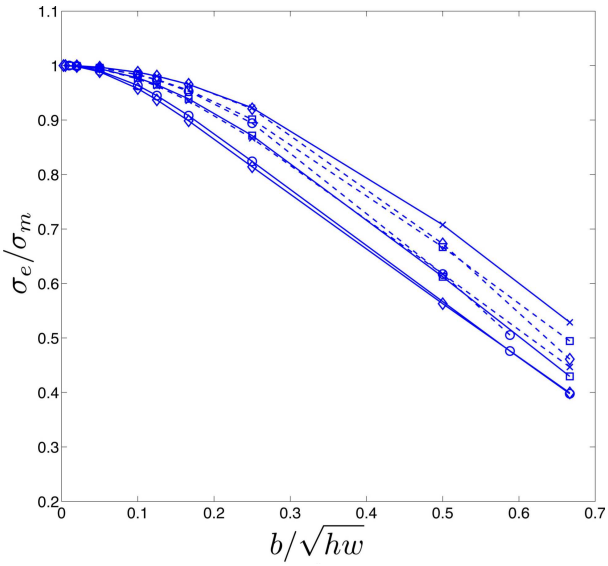

Figure 11: Computed average normalised stress σ_e/σ_m for pores A (□) , B (○), C (△) and D (×) (solid lines) and A' to D' with corresponding markers and dashed lines, for different pore sizes $b/\sqrt{hw}$. σ_m is the stress in the matrix without a pore.

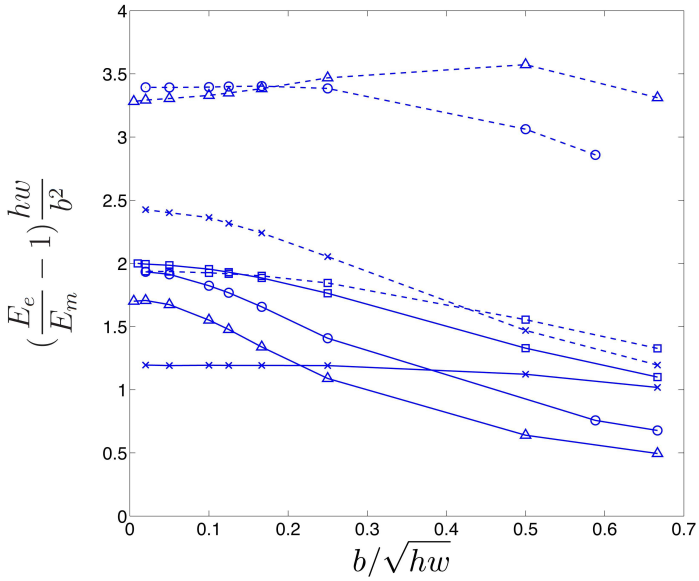

Figure 12: The left hand side of eq. (26) for pores A (□) , B (○), C (△) and D (×) (solid lines) and A' to D' with corresponding markers and dashed lines, for different pore sizes $b/\sqrt{hw}$.

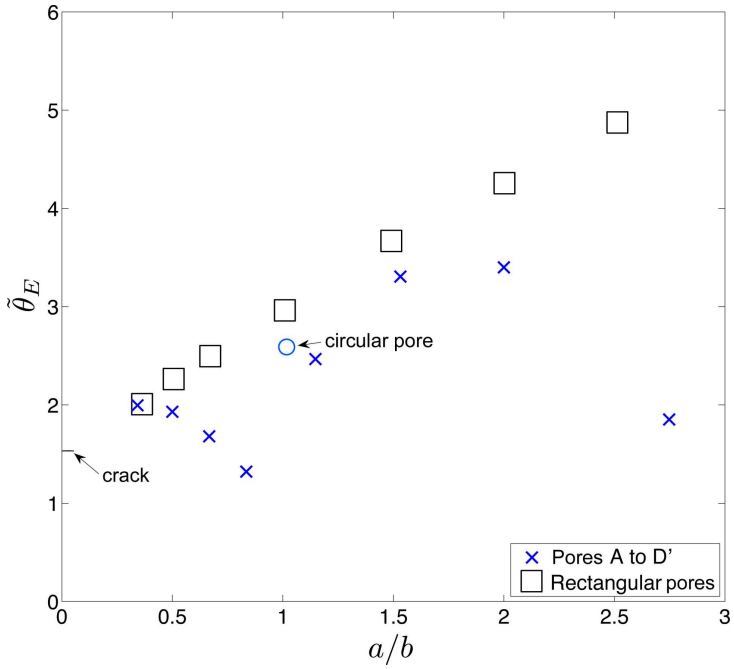

Figure 13: $\tilde{\theta}_E$ versus the shape ratio a/b for pores A to D' with markers $\times$. The $\tilde{\theta}_E$ for six rectangular pores with side ratios $a/b = 2.5, 2, 1.5, 1, 0.5, 0.67$ are also presented here with markers $\square$. The side length is a in the direction of the load. The known limit result as $a/b \to 0$, i.e. for a crack, with $\tilde{\theta}_E = \frac{\pi}{2}$ and for a circular hole, $\tilde{\theta}_E = \frac{3\pi}{4}$ with $a/b = 1$ are included.

The obtained $\tilde{\theta}_E$ for pores A to D' and the rectangular pores versus the ratio a/b is shown in Figure 13. In Table 2 $\tilde{\theta}_E$ is listed for pores A to D'. A couple of diverging results are observed. Both are for the slender pores A and C when the nominal stress is along the longest side of the pore, which is b for both. It is known from crack mechanics that energy released at the introduction of a crack vanishes for a crack that is parallel with the loading direction and reaches a maximum if the crack is perpendicular to the loading direction. The exact result as derived in the APPENDIX, $\tilde{\theta}_E = \pi/2$ for a crack and $\tilde{\theta}_E = 3\pi/4$ for a circular pore, is added to Figure 13. The result is obtained by using the analytical solution for an infinite stretched plane body with a circular hole cf. Muskhelishvili (1953). For pores with $a > b$ the nominal stress is parallel with the longer side of the body while eq. (25), that defines the θ_E, only involves the pore width b. This inadvertence might be the reason for the observed influence on the results.

5 Qualifying examples

The method is qualified by applying the superposition technique on real cases for diffusion coefficients and elastic moduli. The porous region of the image in Figure 5 is chosen. The region is recognised as the region with pores labeled A and 1 to 11, framed in the dashed rectangle. Finite element calculations were performed using 17 682 8-node isoparametric elements.

The diffusion coefficient was found to be $D_{e,\mathrm{FEM}} = 1.033D_m$ in the radial (x_1) direction, and $1.071D_m$ in the tangential (x_2) direction. This is compared with the superposition technique using (17), where values for the characteristic shapes were determined using FEM, and are listed in Table 2. The resulting $D_{e,\mathrm{sup}} = 1.030D_m$ in the radial direction and $1.068D_m$ in the tangential direction.

The numerically calculated elastic modulus was found to be $E_{e,\mathrm{FEM}} = 0.895E_m$ in the radial direction and $0.955E_m$ in the tangential direction. The superposition technique gives $E_{e,\mathrm{sup}} = 0.889E_m$ and $0.948E_m$ in the radial and the tangential directions respectively. In both cases the superposition method gives smaller moduli than the finite element method.

The reason for these differences regarding diffusion coefficient and elastic modulus is for the presence somewhat unclear. For the superposition model, applied in both radial and tangential directions, the increase of the diffusion coefficients due to the pores is 0.3 percentage points less, while the decrease of the elastic moduli is 0.7 percentage points more than the FEM result (see Table 3. The expectations from the result displayed in Figs. 8 and 12 where the real diffusion coefficients are larger and the elastic moduli are smaller for larger pore densities excludes the possibility that the deviations should be caused by a too small mesh to pore size ratio. Another possibility is that the meshing of the regions bwteen the cells with pores where the flux and stress, in the superposition model is supposed to be uniaxial. The uniaxial field should be modelled with a very high accuracy, if not with machine precision. On the other hand 0.7% and 0.3% is normally considered to be rather good for being a FEM result.

Finite element approximations are known to give a upper bound for the stiffness when full integration is performed, as is done here. At prescribed displacements and concentrations, stress and flux is overestimated which leads to an overestimation of D_e

Table 3: Superposition and FEM results compared, for diffusion and elastic deformation.

	Sup.	FEM	difference
radial diffusion	3.0%	3.3%	0.3%
tangential diffusion	6.8%	7.1%	0.3%
radial stress	−11.1%	−10.5%	0.7%
tangential stress	−5.2%	−4.5%	0.7%

and E_e. It is also worth noting that the result in this respect is the same in both radial and tangential directions, which could indicate a relatively weak dependence of the pore shape and orientation. The latter could, implicate that the superposition results are the most accurate. A definite answer regarding the accuracy requires further studies of more examples with a variation of pore densities.

The differences between the FEM results and the superposition model as fractions of the rather small pore induced changes are between 4% and 16%. Considering this it is important to realise that the obtained results should be used with caution especially at low pore densities.

6 Conclusions

Superposition principles are derived that employ dimensional scaling of material parameters. The correction is asymptotically exact for small pore sizes. In the present study the error is found to be less than 10% of the pore correction of the diffusion coefficient if $\sqrt{A_p/hw} < 0.3$, and 10% of the correction of the modulus of elasticity if $b/\sqrt{hw} < 0.1$ (cf. Figs. 8 and 12).

In the present analysis the pores have width to height ratios w/h in the range 0.37 to 2.7. The difference between the pore influence on the effective diffusion coefficient and the modulus of elasticity is of the order of 2.5, cf. Figs. 9 and 13.

The method is evaluated for a sample of bovine ulna for both the diffusion and deformation case. The superposition results are compared with full scale finite element results. Specifically, the change of the diffusion coefficient and the change of the elastic modulus due to the presence of pores, are compared with the corresponding finite element results. The change of the diffusion coefficient is 3 to 7% depending of the direction of the flux. The change of the modulus of elasticity is 5 to 11% depending on the loading direction.

Compared with finite element results a difference of 0.3% of the diffusion coefficient and of 0.7% of the modulus of elasticity is found. Relative to the correction itself the difference make up 4 to 16%. The reason for the differences between the two models is discussed. Since the requirement that the pores should be sparse is well fulfilled. A possible reason could be that the smallness of the correction amplifies expected errors of the finite element calculation. A support is found in the fact that the superposition is definitely leading to the trivial result $D_{e,\mathrm{sup}} = D_m$ and $E_{e,\mathrm{sup}} = E_m$ for vanishing pores, whereas the finite element result may depend on the element size and the irregular mesh that is produced by the finite element preprocessor, cf. ABAQUS User's manual 6.14 (2014).

Appendix: Using the M-integral

The reduction of the stiffness of a large panel with a circular hole or a crack through its thickness is calculated using the path independent M-integral. The integral is based on a conservation law applicable to elastostatics that was obtained by Knowles and Sternberg (1972). The integral is a function of the stress and displacement gradient field. As a consequence of the path independence it vanishes for a closed loop path bounding a regular region. Opposed to that, integration along a closed loop bounding a non-regular region, e.g. a region containing a pore, such as a hole or a crack, does generally not vanish. Budiansky and Rice (1973) showed that in this case the M-integral can be interpreted as the potential energy release rate associated with an expansion of the region. For more details regarding the M-integral cf. Freund (1978). Expand in this context means a scaling of all geometrical characteristics. From the energy release rate follows the change of the stiffness of the structure.

The value of M is defined by the line integral

$$M = \int_{\Omega} \left(W n_i - T_j \frac{\partial u_j}{\partial x_i} \right) x_i \mathrm{d}\Gamma \,, \tag{31}$$

where W is the elastic energy density, n_i is the unit normal to Ω which is directed to the right relative to the direction of the path Γ in the x_1-x_2 plane, T_i are the tractions acting on the material to the left of Ω relative to the direction of Γ and u_i are the displacements. The elastic strain energy density is defined by

$$W = \frac{1}{2} \sigma_{ij} \epsilon_{ij} \,, \tag{32}$$

where the stress components σ_{ij} are related to the strain components ϵ_{ij} via Hooke's law. The path-independence of M in eq. (31) follows directly from a corresponding conservation law (cf. Budiansky and Rice (1973)).

Consider a stretched large plane panel with height h and width w so that $0 \leq x_1 \leq h$ and $0 \leq x_2 \leq w$ in a Cartesian coordinate system as shown in Figure 14. The pore is here either a circular hole with the diameter b or a crack with the length b. The stretching is given as a constant displacement $u_1 = \delta$ of the edge at $x_1 = h$. The displacement $u_1 = 0$ along the edge at $x_1 = 0$. Remaining boundary conditions are absence of tractions along all edges. Without loss of generality plane stress is assumed.

The integration loop is divided into eight segments, Ω_1 to Ω_8, that form a closed loop encompassing a regular region, see Figure 14. The contributions M_1 to M_8 from integration over the corresponding segments add up to

$$M_1 + M_2 + ... + M_8 = 0 \,. \tag{33}$$

The contributions are defined as

$$M_N = \int_{\Omega_N} \left(W n_i - T_j \frac{\partial u_j}{\partial x_i} \right) x_i \mathrm{d}\Gamma \quad \text{for} \quad N = 1, ..., 8 \,. \tag{34}$$

Because of the reversed direction of both the outward normals and the tractions, the contributions from the integration along Ω_2 and Ω_8 annulate each other, i.e. $M_2 + M_8 = 0$.

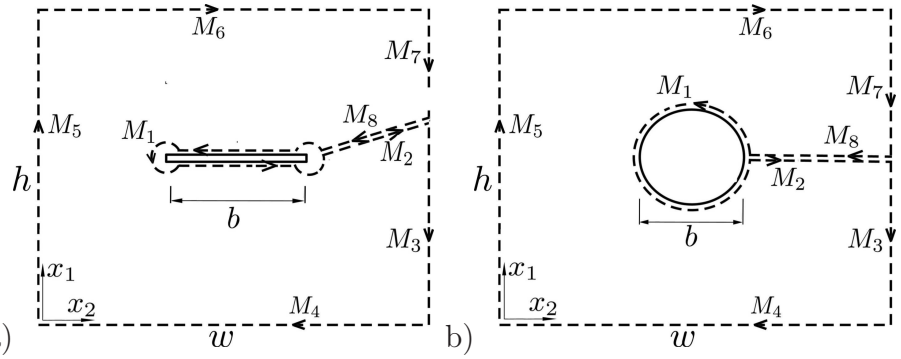

Figure 14: a) Integration path for a panel with a crack. b) Same for a panel with a circular hole.

On segments Ω_3 and Ω_7: $x_2 = w$, $n_1 = 0$, $n_2 = -1$, $T_1 = T_2 = 0$, and $\mathrm{d}\Gamma = -\mathrm{d}x_1$ which gives

$$M_3 + M_7 = -\frac{w}{2E_b}\int_0^h \sigma_{11}^2 \mathrm{d}x_1 \,. \tag{35}$$

On segment Ω_4: $x_1 = 0$, $n_2 = 0$, $T_2 = 0$, and $u_1 = 0 \;\Rightarrow\; \partial u_1/\partial x_2 = 0$, which gives

$$M_4 = 0 \,. \tag{36}$$

On segment Ω_5: $x_2 = 0$, $n_1 = 0$, and $T_1 = T_2 = 0$, which gives

$$M_5 = 0 \,. \tag{37}$$

Finally on segment Ω_6: $x_1 = h$, $n_1 = -1$, $n_2 = 0$, $T_1 = -\sigma_{11}$, $T_2 = 0$, $\partial u_1/\partial x_1 = \epsilon_{11} = (\sigma_{11} - \nu\sigma_{22})/E_b$, $\partial u_1/\partial x_2 = 0$, and $\mathrm{d}\Gamma = \mathrm{d}x_2$ which gives

$$M_6 = \frac{h}{2E_b}\int_0^w (\sigma_{11}^2 - \sigma_{22}^2)\mathrm{d}x_2 \,. \tag{38}$$

Now eq. (33) reduces to

$$M_1 = -M_3 - M_7 - M_6 \,, \tag{39}$$

which reads

$$M_1 = \frac{w}{2E_b}\int_0^h \left\{\sigma_{11}^2\right\}_{x_2=w} \mathrm{d}x_1 - \frac{h}{2E_b}\int_0^w \left\{\sigma_{11}^2 - \sigma_{22}^2\right\}_{x_1=h} \mathrm{d}x_2 \,. \tag{40}$$

By splitting the stresses into

$$\sigma_{11} = \sigma_o + \Delta\sigma_{11} \,\text{and}\, \sigma_{22} = \Delta\sigma_{22} \,, \tag{41}$$

where σ_o is the stress in a homogeneous panel and $\Delta\sigma_{11}$ and $\Delta\sigma_{22}$ are stresses that arise because of the pore, in this case the circular hole or the crack. Since the pore is supposed to be small as compared to the extent of the panel the result is that $\Delta\sigma_{11}/\sigma_o$ and $\Delta\sigma_2/\sigma_o \;\rightarrow$ 0. After excluding second order terms of eq. (40) it follows that

$$M_1 = \frac{\sigma_o}{E_b}\left\{w\int_0^h \left\{\Delta\sigma_{11}\right\}_{x_2=w} \mathrm{d}x_1 - h\int_0^w \left\{\Delta\sigma_{11}\right\}_{x_1=h} \mathrm{d}x_2\right\} . \tag{42}$$

Per definition eq. (24) and eq. (23) give

$$E_e = \frac{h}{\delta w} \int_0^w \{\sigma_{11}\}_{x_1=h} \, \mathrm{d}x_2 \, . \tag{43}$$

Using that the nominal stress $\sigma_o = \frac{\delta}{h} E_b$ gives

$$E_e = E_b - \frac{h}{\delta^2 w} M_1 + \frac{1}{\delta} \int_0^h \{\Delta\sigma_{11}\}_{x_2=w} \, \mathrm{d}x_1 \, . \tag{44}$$

For a small pore in a wide panel, i.e., $w \gg h$, the integral term in eq. (44) becomes insignificant, i.e.

$$E_e = E_b - \frac{h}{\delta^2 w} M_1 \, . \tag{45}$$

A panel with a crack

Consider the path M_1 along a crack in an anti-clockwise direction for a crack that is placed perpendicular to the loading direction as shown in Figure 14a. The crack path follows along the surfaces and encircling the crack tips to avoid the stress singularities present at the crack tips. According to Budiansky and Rice (1973), the value of the M-integral is related to the crack tip driving force G as

$$M_1 = bG \, . \tag{46}$$

For a small crack G is given by the relation

$$G = \frac{K_\mathrm{I}^2}{E_b} = \frac{\pi}{2} \frac{\sigma_o^2 b}{E_b} \, , \tag{47}$$

where $K_\mathrm{I} = \sigma_o \sqrt{\pi b/2}$ is the stress intensity factor.

With this inserted in eq. (45)

$$E_e = E_b \left(1 - \frac{\pi}{2} \frac{b^2}{hw} \right) \, . \tag{48}$$

By comparing with eq. (25), the shape factor $\tilde{\theta}_E$ for a crack is identified as

$$\tilde{\theta}_E = \frac{\pi}{2} \, . \tag{49}$$

A panel with a hole

A closed loop encircling a circular hole in a panel also in an anti-clockwise direction is displayed in Figure 14b. Calculation of M_1 requires the stresses and strains on the perimeter of the hole. Absent tractions, i.e., $T_r = T_\phi = 0$ reduces the strain energy density to $W = \sigma_\phi^2 / 2E_b$, whereas the only non-zero stress component is σ_ϕ. With $n_1 = \cos\phi$, $n_2 = \sin\phi$, $x_1 = \frac{b}{2}\cos\phi$, $x_2 = \frac{b}{2}\sin\phi$, and $\mathrm{d}\Gamma = \frac{b}{2}\mathrm{d}\theta$, M_1 becomes

$$M_1 = \int_0^{2\pi} \frac{\sigma_\phi^2}{4E_b} b \mathrm{d}\phi \, . \tag{50}$$

The stress σ_ϕ may be found in text books on elastostatics, see e.g. Fung (1965). The stress distribution is provided as

$$\sigma_\phi = \sigma_o(1 - 2\cos 2\phi)\,. \tag{51}$$

Inserting this into eq. (6) one obtains

$$M_1 = \frac{\sigma_o^2 b^2}{8E_b}\int_0^{2\pi}(1 - 2\cos 2\phi)^2 \mathrm{d}\phi = \frac{3\pi}{4}\frac{\sigma_o^2 b^2}{E_b}\,, \tag{52}$$

after using the relations $r^2 = x_1^2 + x_2^2 = b^2/4$ and $\mathrm{d}\Gamma = r\mathrm{d}\phi$. Inserted in eq. (45) the result now reads

$$E_e = E_b\left(1 - \frac{3\pi}{4}\frac{b^2}{hw}\right)\,. \tag{53}$$

The $\tilde{\theta}_E$ for a circular hole is identified using eq. (25) as

$$\tilde{\theta}_E = \frac{3\pi}{4}\,. \tag{54}$$

Acknowledgements

Financial support from Erasmus Mundus Action 2 and from The Swedish Research Council under grant no 2011-5561 are gratefully acknowledged.

References

Biot, M.A. (1941) 'General theory of three-dimensional consolidation', *Journal of applied physics*, 12(2):155-64

Budiansky, B., Rice, J.R. (1973) 'Conservation Laws and Energy Release-rates', *Journal of applied mechanics*, 40(1):201-3

Cowin S.C. (2003) 'A recasting of anisotropic poroelasticity in matrices of tensor components', *Transport in porous media*, 50(1-2):35-56

Cussler, E.L. (1997) 'Diffusion: Mass Transfer in Fluid Systems (2nd ed.)', Cambridge University Press, New York, USA

Dassault Systemes (2014) 'Abaqus User's Manual', Simulia Coporation

Freund, L.B. (1978) 'Stress intensity factor calculations based on a conservation integral', *International journal of solids and structures*, 14(3):241-50

Fung, Y.C. (1965) 'Foundations of Solid Mechanics', Prentice-Hall, Inc., New Jersey, USA

Grimal, Q., Rus, G., Parnell, W.J., Laugier, P. (2011) 'A two-parameter model of the effective elastic tensor for cortical bone', *Journal of biomechanics*, 44(8):1621-5

Helsing, J., Jonsson, A. (2002) 'On the computation of stress fields on polygonal domains with V-notches', *International Journal for Numerical Methods in Engineering*, 53(2):433-53

Helsing, J. (2011) 'A fast and stable solver for singular integral equations on piecewise smooth curves', *SIAM J. Sci. Comput*, 33(1):153-74

Knowles, J. K., Sternberg, E. (1972) 'On a class of conservation laws in linearized and finite elastostatics', *Archive for Rational Mechanics and Analysis*, 44(3):187–211

Li, W., You, L., Schaffler, M.B., Wang, L. (2009) 'The dependency of solute diffusion on molecular weight and shape in intact bone', *Bone*, 45(5):1017-23

Lindberg, G., Shokry, A., Reheman, W., Svensson, I. (2014) 'Determination of diffusion coefficients in bovine bone by means of conductivity measurement', *International Journal of Experimental and Computational Biomechanics*, 2(4):324-42

Marinozzi, F. and Bini, F., Marinozzi, A. (2013) 'Hygroscopic swelling in single trabecula from human femur head', Special Issue of the *European Cells & Materials* 26(6):109

Marinozzi, F., Bini, F., Quintino, A., Corcione, M., Marinozzi, A. (2014a) 'Experimental Study of Diffusion Coefficients of Water through the Collagen: Apatite Porosity in Human Trabecular Bone Tissue', *BioMed research international*, Vol. 2014

Marinozzi, F. and Bini, F., Marinozzi, A. (2014b) 'Water uptake and swelling in single trabeculae from human femur head', *Biomatter*, Vol. 4

Muskhelishvili, N.I. (1953) 'Some Basic Problems of the Mathematical Theory of Elasticity', P. Noordhoff Ltd. Groningen, Holland

Nozad, I., Carbonell, R.G. and Whitaker, S. (1985) 'Heat conduction in multiphase systems I. Theory and experiment for two-phase systems', *Chemical Engineering Science*, 40(5):843-55

Ochoa-Tapia, J.A., Stroeve, P. and Whitaker, S. (1994) 'Diffusive transport en two-phase media : spatially periodic models and Maxwell's theory', *Chemical Engineering Science*, 49(5):709-26

Patel, R.B., O'Leary, J.M., Bhatt, S.J., Vasnja, A., Knothe Tate, M.L. (2004) 'Determining the permeability of cortical bone at multiple length scales using fluorescence recovery after photobleaching techniques', Proceedings of the 51st Annual ORS Meeting, Vol. 141

Perrins W.T., McKenzie D.R. and McPhedran R.C. (1979) 'Transport properties of regular arrays of cylinders' *Proceedings of the Royal Society of London*, 369(1737):207-25

Redwood, W.R., Rall, E. and Perl W. (1974) 'Red cell membrane permeability deduced from bulk diffusion coefficients', *The Journal of General Physiology*, 64(6):706-29

Rice, J.R., Cleary, M.P. (1976) 'Some basic stress diffusion solutions for fluid-saturated elastic porous media with compressible constituents', *Reviews of Geophysics*, 14(2):227-41

Safford, R.E., Bassingthwaighte, E.A. and Bassinghtwaighte, J.B. (1978) 'Diffusion of water in cat ventricular myocardium', *The Journal of General Physiology*, 72(4):513-38

Schaffler, M.B., Burr, D.B. (1988) 'Stiffness of compact bone: effects of porosity and density', *Journal of biomechanics*, 21(1):13-6

Showalter, R.E. (2000) 'Diffusion in poro-elastic media', *Journal of mathematical analysis and applications*, 251(1):310-40

Ståhle, P., Persson, C., Isaksson, P. (2013) CT-images, Data set: Researchgate, URL http://dx.doi.org/10.13140/RG.2.1.3961.8082

Wang, L., Wang, Y., Han, Y., Henderson, S.C., Majeska, R.J., Weinbaum, S., Schaffler, M.B. (2005) 'In situ measurement of solute transport in the bone lacunar-canalicular system', Proceedings of the National Academy of Sciences of the United States of America, National Acad. Sciences, 102(33):11911-6

Winkelstein, B.A. (2012) 'Ortopaedic Biomechanics', CRC Press, Fl, USA